2019

OLEDs: Light extraction and deep blue emission

Chamika Manoj Dulanja Hippola
Iowa State University

OLEDs: Light extraction and deep blue emission

by

Chamika Hippola

A dissertation submitted to the graduate faculty

in partial fulfillment of the requirements for the degree of

DOCTOR OF PHILOSOPHY

Major: Condensed Matter Physics

Program of Study Committee:
Joseph Shinar, Co-major Professor
Ruth Shinar, Co-major Professor
Rana Biswas
Kerry Whisnant
James Evans

The student author, whose presentation of the scholarship herein was approved by the program of study committee, is solely responsible for the content of this dissertation. The Graduate College will ensure this dissertation is globally accessible and will not permit alterations after a degree is conferred.

Iowa State University

Ames, Iowa

2019

DEDICATION

I like to dedicate this dissertation to my parents Dayananda and Sujatha Hippola, my wife Iresha Wijayapala, my two daughters, Chathuli and Dineli Hippola and my brother Dinupa Hippola for their continuous support throughout my graduate studies.

TABLE OF CONTENTS

Page

LIST OF FIGURES

Page

LIST OF TABLES

Page

ACKNOWLEDGMENTS

I would like to express my gratitude to Dr. Joseph Shinar and Dr. Ruth Shinar, for serving as my major professors throughout my graduate studies. Without your continuous guidance and help, this dissertation would not be a reality. Thank you very much for your support and courageous words during the hard times that I faced both professionally and personally.

I would like to thank, Dr. Rana Biswas for all the valuable discussions we had, that helped me understand the theoretical background. I am extremely grateful for Dr. Karry Whisnant and Dr. James Evans for agreeing to be members of my program of study committee (POSC). I am very lucky to collaborate with Dr. Dennis Slafer, Diane Martin, and Tom Trovato for more than two years, and thank you for your wise words and support to make my work successful. Also, I am extremely thankful to Dr. J.W Petrich, Dr. Ujjal Bhattacharjee, Dr. Matthew Lynn, Dr. Toby Nelson, and Dr. Niradha Sachinthani for helping me in certain research aspects.

I express my gratitude to my parents, Dayananda Hippola, and Sujatha Hippola for their unconditional love and support throughout my life. Thank you very much for believing in me and pushing me to achieve greatness. I thank my wife, Iresha Wijayapala, for the enormous support and encouragement you are giving me and taking care of our two daughters. It would not be possible to achieve this without your support. I express my gratitude to my beautiful daughters, Chathuli Hippola and Dineli Hippola, for being a part of my life. I also like to thank my parents-in-law, Sumana Wijayapala, and late Ajantha Wijayapala for their encouragement.

I want to express my gratitude to my past and present group members, Dr. Dusan Danilovic, Dr. Wai Leung, Dr. Joong-mok Park Dr. Eeshita Manna, Dr. Ying Chen, Dr. Min Cai, Dr. Teng Xiao, Dr. Emily Hellerich, Dr. Weipan Cui, Dr. Fadzai Fungura, Rajiv Kaudal, Erik Dykstra, Joshua Wolanyk. Raghunandan B-Iyer, and Michael Fralaide for their wonderful support in the lab. I am grateful to Eeshita, Emily, and Ying for teaching me the first steps towards OLEDs and optically/ electrically detected magnetic resonance (ODMR/ EDMR). My special thanks go to Dusan, for his great encouragement and his wonderful guidance during my Ph.D.

In addition, I would also like to thank the Physics Department and Ames Laboratory supporting staff, Lori Hockett, Gloria Oberender, Debra Schmidt, Nancy Filkins, and Larry Stoltenberg for all the help you provided over the last seven years.

I am grateful to the Department of Physics and Astronomy, Ames Laboratory, U.S. Department of Energy (USDOE) for continuously supporting my research for the last seven years. This work was partially supported by USDOE, Office of Energy Efficiency and Renewable Energy under Grant Nos. DE-SC0011337 and DE-EE0007621 and by the Basic Energy Sciences, Division of Materials Science and Engineering, USDOE at Ames Laboratory under the contract number DE-AC 02–07CH11358. The Ames Laboratory is operated for the USDOE by Iowa State University.

ABSTRACT

OLEDs have emerged in the market over the last decade mainly in display applications due to their unique and attractive properties, such as lightweight, high brightness with strong color contrast, thin and flexible designs as well as potentially of low cost. OLEDs for lighting applications are under extensive research and development. Though promising for solid-state lighting, there are critical aspects that need to be addressed to increase their efficiency, which will lead to commercialization.

One major issue is the ~20% OLEDs' limited forward outcoupling efficiency. This is due to several loss processes. More specifically, light generated in the emissive layer is internally trapped/ waveguided in the substrate or lost to surface plasmon excitation at the metal cathode. Another issue is the less efficient and unstable blue, especially deep blue (400-450 nm), OLEDs.

This dissertation addresses both of these key OLED issues.

The outcoupling efficiency that is limited by the internal/ external waveguiding along with surface plasmon excitation loss was enhanced by using novel corrugated plastic substrates. The unique substrate structure enables enhanced outcoupling in the forward hemisphere by minimizing total internal reflection and surface plasmon excitation. The dissertation demonstrates OLEDs with an external quantum efficiency of 50%, meaning an outcoupling efficiency ≥ 50% for a green phosphorescent OLEDs which yields a > 2-fold enhancement over the conventional flat devices. Enhancements were observed for blue and white phosphorescent devices depending on the pitch of the corrugation and the features' height.

Bright (14000 cd/m^2) deep blue TADF exciplex-based OLEDs were fabricated using low cost abundant commercial organic small molecules, including triphenylphosphine oxide (PPh_3O). The deep blue emission peaked at ~435 nm with the peak emission credited mainly to triplet exciplex emission at NPB/TPBi:PPh_3O 5:1 interface. The triplet emission was confirmed by the strong quenching of the phosphorescence of the emitting layer in the presence of O_2.

CHAPTER 1. INTRODUCTION TO ORGANIC LIGHT EMITTING DIODES

1.1. History of OLEDs

Electroluminescence (EL) from an organic molecule was first reported in 1955 by A. Bernanose et al. [1] It was obtained by applying high alternating voltages to a cellulose film doped with acridine orange. In 1963 EL was observed in single crystal anthracene and tetracene-doped anthracene crystals at 400 V by M. Pope et al. [2]. Due to the high driving voltage of these discoveries, organic molecules were seen as potential display or lighting sources at that time. The perspective of EL of organic molecules was recognized in 1987 with the fabrication of world's first thin film organic light emitting diode (OLED) by C.W Tang et al. A 60 nm thick layer of an organic small molecule, 8-hydroxyquinoline aluminum (Alq_3) was sandwiched between indium tin oxide (ITO) and magnesium:silver with a 10:1 ratio electrodes to achieve a brightness >1000 cd/m^2 at an applied voltage < 10 V. The external quantum efficiency (EQE) reported for the aforementioned device was about 1% [3]. Friend and coworkers fabricated the first polymer light emitting diode (PLED) in 1990 using poly(p-phenylene vinylene) (PPV), where the polymer film was formed by a solution process [4]. The first flexible OLED was fabricated in 1992 on a polyethylene terephthalate (PET) substrate [5]. In 1994 the first white OLED (WOLED) was demonstrated by J. Kido et al. [6].

1998 marked as a significant year in the field due to the invention of phosphorescent OLEDs (PhOLEDs). The groundbreaking work was carried out by Forrest and coworkers using Platinum octaethylporphyrin (PtOEP) [7]. The discovery was significant due to the fact that in fluorescent OLEDs only 25% of the generated excitons, which are singlets, are allowed to decay radiatively to the ground state while the remaining 75% triplet excitons are lost in non-radiative processes. Thus, the theoretical internal quantum efficiency (IQE) of the fluorescent

OLED is limited to 25%, which results in ~5% EQE due to the limited ~20% forward outcoupling. The use of organic molecules with a heavy metal such as platinum (Pt), which induces strong spin-orbit coupling, allows radiative decay of both singlet and the triplet excitons, consequently leading to a theoretically achievable IQE of 100%, and hence, EQE ~20%.

Another remarkable discovery is the fabrication of thermally activated delayed fluorescence (TADF) OLEDs in 2009 by Adachi and coworkers [8]. By synthesizing organic molecules with a small energy difference between the singlet and triplet states (ΔE_{ST}), triplet excitons can cross over to the singlet state via reverse intersystem crossing (rISC), allowing their radiative decay to the ground state, thus significantly improving the OLEDs' efficiency.

The first commercial OLED product came into the market in 1997, a display in a car audio system produced by Tohoku Pioneer [9]. Commercial OLED products have improved since this initial step to fascinating and interesting inventions such as paper-like televisions, rollable displays, foldable mobile phones, and mirror-like displays (**Figure 1.1**). Some of these devices are still in the prototype stage, while others are already commercially available. OLEDs have grown to a stage where they can compete successfully with other display technologies, such as light emitting diodes (LEDs), with lighting applications following.

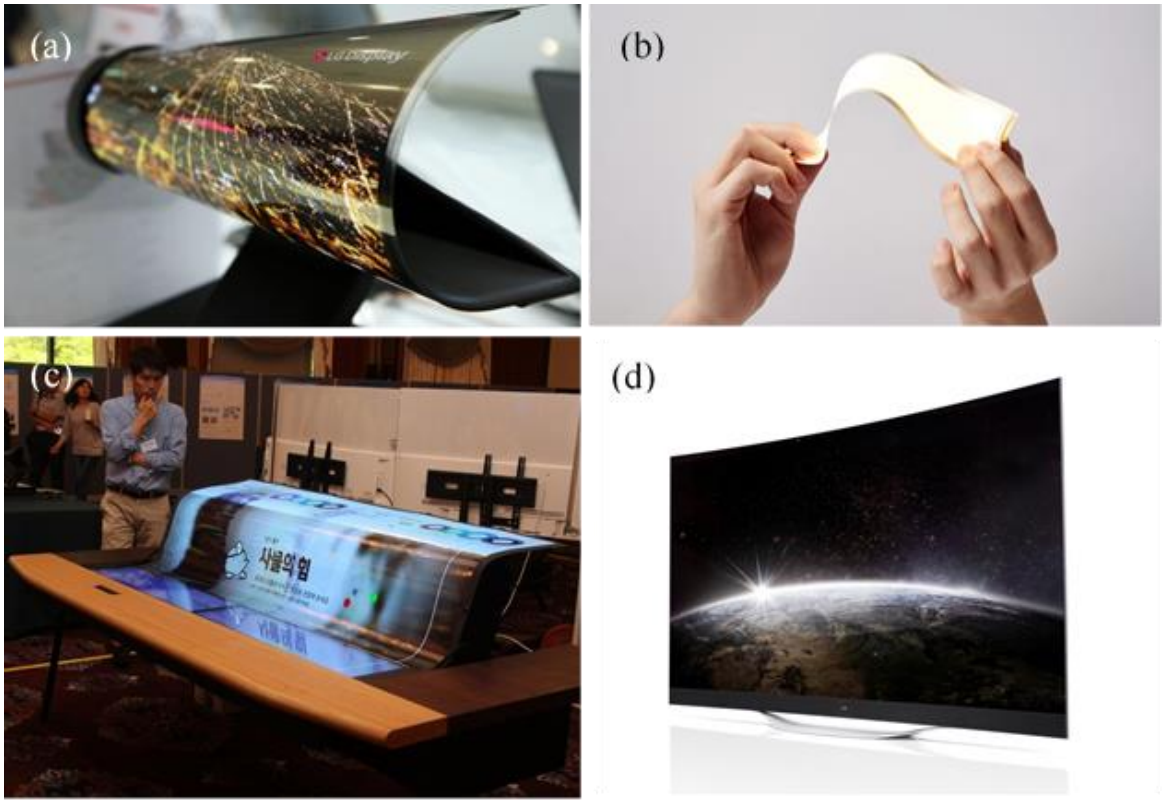

Figure 1.1: Latest OLED products, a) rollable OLED display made on PET by LG Displays, b) flexible white OLED lighting panel by LG Chem [10]*, c) 77" OLED smart desk by LG Displays* [11]*, d) 77" Ultra high definition curved OLED TV by LG.*

OLEDs possess many advantages over conventional display and lighting technologies. OLED displays can be extremely lightweight, and devices are not limited to a rigid substrate, which enables applications in foldable and wearable technologies. With the advantages ability to simply fabricate OLEDs on flexible substrates, roll-to-roll mass production is possible, which is expected to reduce manufacturing cost significantly. With the ability to work without a continuously driven backlight, OLED displays provide incredible picture quality and lower power consumption. Relative inefficiency and short lifetime of blue OLEDs still remains a challenge.

1.2. OLED Structure

OLEDs consist of multiple organic thin films stacked between two electrodes, as shown in **Figure 1.2**. Generally, a transparent anode is formed on a substrate, which can be either glass or plastic. In state-of-the-art OLEDs, the anode is followed by a hole injection layer (HIL), a hole transport layer (HTL), an emissive layer (EML), an electron transport layer (ETL), electron injection layer (EIL), and a cathode. A hole blocking layer (HBL) and an electron blocking layer (EBL) are sometimes added, but often the ETL and HTL also act as hole and electron blocking layers, respectively.

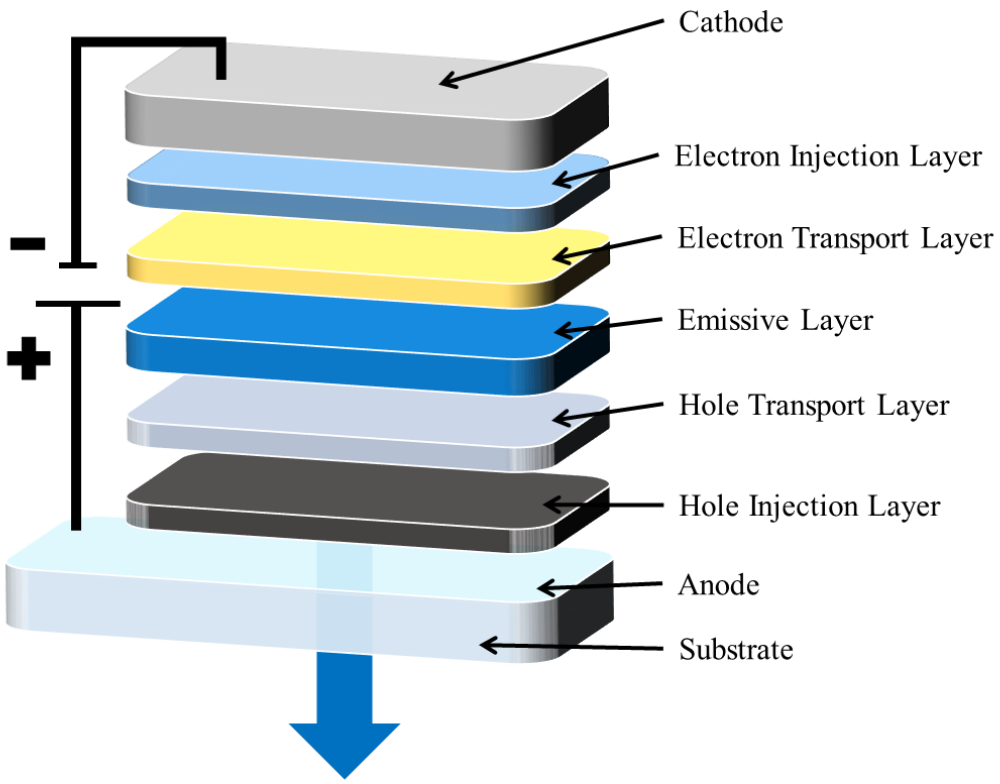

Figure 1.2: Schematic presentation of the layer stacking of a bottom-emitting OLED (not to scale).

A substrate suitable for OLED fabrication needs to have certain properties to obtain optimal device performance. More than 90% optical transmission over the visible spectrum is

required for bottom emitting OLEDs. The transmission needs to be fairly uniform across the visible spectrum to obtain natural color. To avoid any defects, such as pinholes or shorts, the substrate should be preferable flat. A low thermal expansion coefficient can also be a crucial factor if the OLEDs undergo annealing steps. Moreover, OLEDs are very sensitive to water and oxygen; therefore, the substrate is required to have a low permeability to water and oxygen [12].

The transparent anode plays a critical role in device performance. It should be of very low resistivity along with >85% transmission. Maintaining a very low surface roughness is also important since sharp points create localized high electric fields that eventually lead to catastrophic shorts. ITO is a commonly used anode. Its work function (φ_f) is -4.7 eV, which can be increased via surface treatments, such as UV ozone or oxygen plasma etch cleaning [13]. The quality of the ITO highly depends on the deposition technique and conditions. Most commonly ITO is fabricated by radiofrequency (RF) sputtering, with its surface conductivity governed by the annealing temperature and the surface roughness is determined by the argon (Ar) partial pressure inside the chamber [14,15].

The efficiency of an OLED highly depends on efficient carrier injection into the device from both ends. Energy barriers at organic-organic interfaces can be eliminated by careful engineering and material choice. The electrode-organic barrier can be controlled by using HIL and EIL [12]. Commonly used HIL materials include metal oxides such as molybdenum oxide (MoO_3), Tungsten trioxide (WO_3) and vanadium pentoxide (V_2O_5) [16,17].

The charge carriers injected at the electrodes, have to reach the emissive layer for radiative recombination. High carrier mobility and suitable frontier molecular orbital

alignment are two critical factors for an efficient device [12]. Various HTL and ETL materials have been using over the years, and choosing a good HTL or ETL material depends on the entire device architecture. Some of the most commonly used HTL and ETL materials are shown in **Figure 1.3** and **Figure 1.4,** respectively.

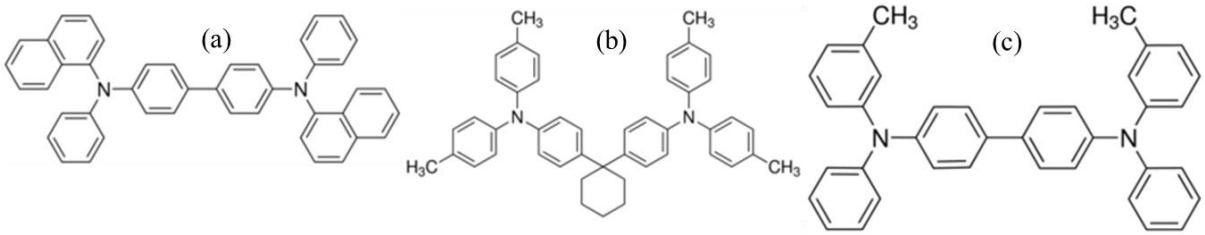

Figure 1.3: Chemical structures of HTL materials. a) N,N′-Di(1-naphthyl)-N,N′-diphenyl-(1,1′-biphenyl)-4,4′-diamine (NPD), b) N,N′-Bis(3-methylphenyl)-N,N′-diphenylbenzidine (TPD), and c) 4,4′-Cyclohexylidenebis[N,N-bis(4-methylphenyl)benzenamine] (TAPC)

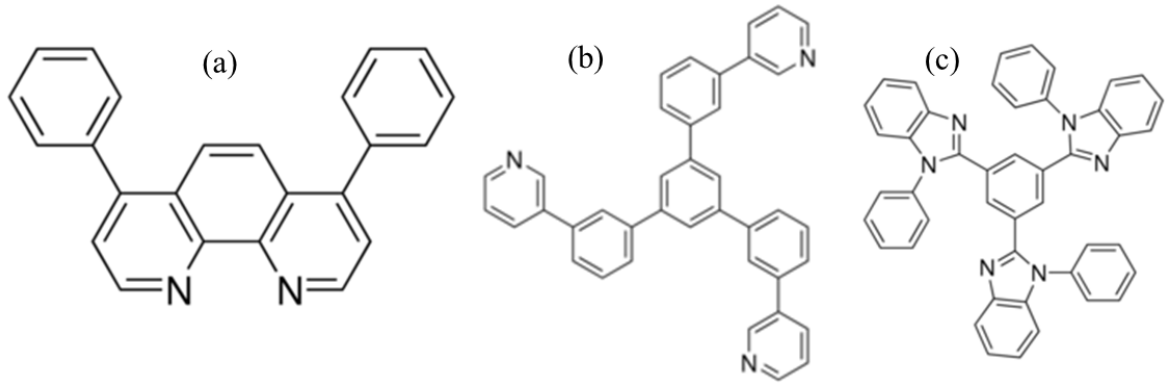

Figure 1.4: Chemical structures of ETL materials. a) Bathophenanthroline (BPhen), b) 1,3,5-Tri(m-pyridin-3-ylphenyl)benzene (TmPyPb), and c) 2,2′,2″-(1,3,5-Benzinetriyl)-tris(1-phenyl-1-H-benzimidazole) (TPBi).

1.3. Operating Principle

1.3.1. Electronic Configuration of Carbon

A Carbon atom has 6 electrons in $1s^2 2s^2 2p^2$ electronic structure. In forming chemical bonds, atomic orbitals are mixed to form hybridized orbitals. As shown in **Figure 1.5**, hybridization results in *sp*, sp^2, or sp^3 orbitals.

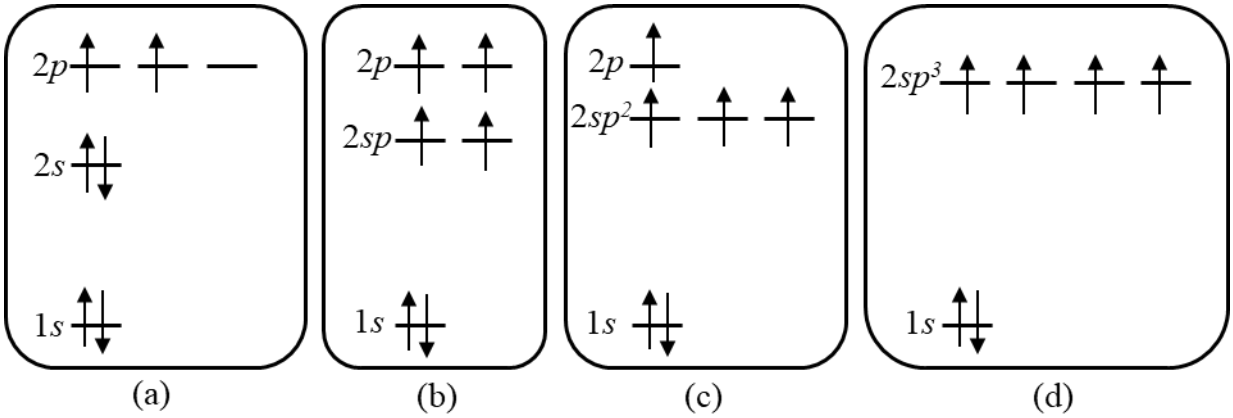

Figure 1.5: The electronic configuration of the carbon atom at a) ground state, b) sp, c) sp^2 and d) sp^3 hybridized states.

As an example, in sp^2 hybridization a 2*s* orbital mixes with two 2*p* orbitals, forming three hybrid sp^2 orbitals (that generate 3 σ bonds) with one remaining (non-hybridized) *p*-orbitals that together with sp^2 orbital forms a double bond. Such *p* orbitals form π bonds. The molecular structure of simple alkenes that have sp^2 hybridization is trigonal, planar with ideal bond angles of 120°.

1.3.2. π-Conjugated Organic Compounds

Organic semiconductors are generally π-conjugated compounds with alternating single and double C bonds. As shown in **Figure 1.6a**, π bonds are formed through an overlap of non-hybridized *p* orbitals of two adjacent carbon atoms. The π bonds are weaker in comparison to σ bonds; they have delocalized electrons, which can hop across molecular segments (e.g., polymers) and from one molecule to another. The semiconducting properties arise from these delocalized electrons of the π bond. Alternating double and single bonds in an organic small molecule or in a polymer backbone is the origin of π conjugation.

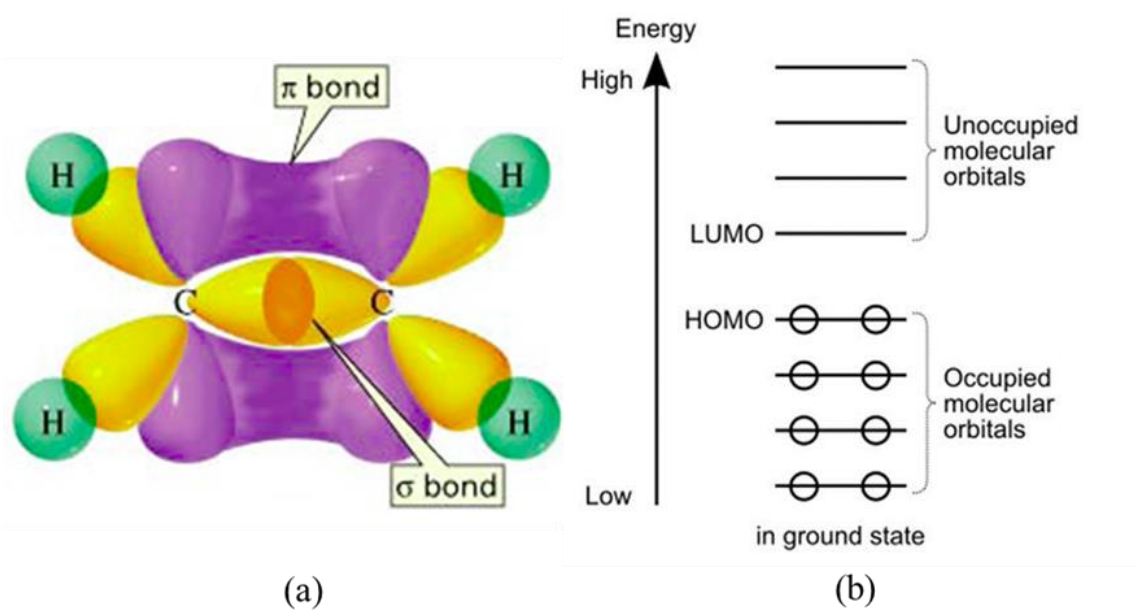

Figure 1.6: a) Schematic representation of σ and π bond formation in carbon double bond b) HOMO and LUMO energy levels

According to Molecular Orbital (MO) theory, molecular wavefunction can be expressed as a linear combination of the atomic orbitals involved. The coefficient associated with each wavefunction can be determined by minimizing the total energy of the system. When atoms are interacting, in proximity, the energy levels split to form lower energy bonding orbitals and higher energy antibonding orbitals. As stated by the Pauli Exclusion Principle, each state can accommodate two electrons, leaving electrons to occupy the bonding state and keeping the anti-bonding state empty. As the number of carbon atoms in a molecule increases, the number of bonding and anti-bonding orbitals also increases forming quasi-continuous energy bands separated by a gap. As indicated in **Figure 1.6b,** all the electrons will occupy the low energy bonding states while the anti-bonding states remain empty. The HOMO is the topmost occupied energy level, and LUMO is the lowest unoccupied level.

A key feature of polymer and in organic small molecule films is their disordered structure. In the case of a polymer, the energetic disorder caused by the structural disorder leads to an inhomogeneous broadening of absorption spectrum bands and to a broad density of states distribution for excitons. Small π conjugated molecules can similarly exhibit a broad density of states distribution due to the structural disorder. The charge transport properties of the organic materials are highly dependent on the width of the density of states in the charge transport manifold. Tail states of the distribution can act as shallow trapping sites for charge carriers at low temperatures [18]. On the other hand, atomic and molecular disorders present in organic semiconductors, give rise to electronic energy states lying in the middle of the energy gap that act as deep traps which can immobilize the charge carriers. In addition to that, deep trap states can also act as effective recombination centers for electron and holes that quench the luminescence and lifetime in OLEDs [19].

1.3.3. Charge Carrier Injection

A typical organic material has a very high resistivity of 10^{15}- 10^{20} Ωcm at low electric fields, indicating that there are no free charge carriers. As a result, the total organic layer thickness of an OLED has limited to ~ 100 nm, unless the electron/ hole transport layers are doped appropriately. Obviously, improving charge injection will improve OLED efficiency and lifetime. Ideally, an ohmic contact is preferred at the metal/organic interface to minimize the driving voltage.

To understand the charge carrier injection at the metal/organic interface, three crucial factors need to be considered. 1) The existence of the image charge at the electrode, 2) The hopping-type charge transport and 3) The presence of the disorder in a non-crystalline system [20]. As the metal and the organic layer establish contact, charge carriers (electrons and holes)

hop into trap states creating an image potential in the electrode that reduces the barrier to an effective potential barrier given by **Equation 1.1** and illustrated in **Figure 1.7**.

$$e\varphi_B(r) = e\varphi_m - eEr - \frac{e}{16\pi\varepsilon r} \tag{1.1}$$

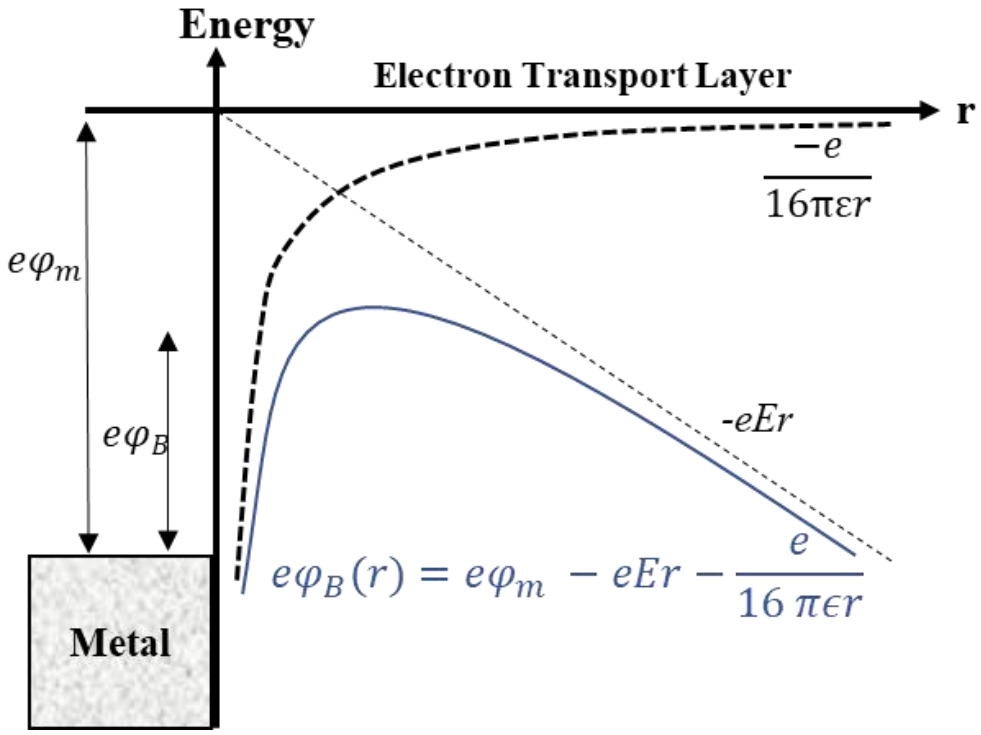

Figure 1.7: Effective potential barrier experienced by an electron at the metal/organic interface.

Two main mechanisms are used to describe charge injection at metal-organic interfaces, namely the Richardson-Schottky model and the Fowler-Nordheim tunneling [21].

1. The Richardson-Schottky (RS) model describes a field-assisted thermionic emission in which the carriers are thermally excited to overcome the potential barrier ($q\varphi_B$) formed by the image charge potential and the external electric field

(**Figure 1.7**). The thermionic injection current has an Arrhenius-type temperature dependence (**Equation 1.2**) and a Poole-Frankel type field dependence (**Equation 1.3**). The model predicts that the injection of charge carriers can occur from the metal into the semiconductor if the thermal energy is sufficient to overcome the Schottky barrier [22–24].

$$\ln j_{RS} \propto T \tag{1.2}$$

$$\ln J_{RS} \propto \sqrt{E} \tag{1.3}$$

2. The Fowler-Nordheim (FN) tunneling injection model assumes an electron present in the Fermi level of the metal can tunnel through the triangular potential barrier formed as a result of the interfacial barrier and the current density generated by FN tunneling can be written as,

$$J_{FN} = \frac{q^3}{8\pi h \varphi_B} E^2 e^{\frac{-8\pi\sqrt{2m^*}\varphi_B^{1.5}}{3hqE}} \tag{1.4}$$

Where m^* is the effective charge carrier mass, q is the electron charge and φ_B is the barrier height [25].

1.3.4. Charge Carrier Transport

As mentioned, alternating single-double bonds in organic molecules results in charge delocalization. Organic molecules, however, interact via relatively weak van der Waals interaction, and as a result, the electronic wavefunctions are localized on a finite number of

molecules or even on individual molecules. Additionally, organic films are often amorphous, though crystalline structures can be obtained in some cases. These fundamental properties lead to various transport mechanisms, i.e., hopping, band-like, and multiple trapping and release [26].

Hopping transport model: moving charges induces lattice polarization due to a stronger intramolecular coupling between electrons and phonons. Because of the polarization, the lattice relaxes to a new equilibrium state, creating a potential well for the polaron, thus confining its movement. When the electronic wave functions of two neighboring sites overlap, the polaron hops from one site to the next via tunneling. **(Figure 1.8)** [12,26]. The Marcus theory is widely used for evaluating the charge transfer rate by hopping. In the absence of an electric field, the hopping rate is estimated by,

$$K_{hop} = \frac{2\pi}{\hbar} t^2 \frac{1}{\sqrt{4\pi\lambda k_B T}} e^{\left[-\frac{\lambda}{4k_B T}\right]} \qquad (1.6)$$

Where T is the absolute temperature, k_B is the Boltzmann's constant, t is the transfer integral that reflects the strength of the electronic interaction between adjacent molecules and λ is the total reorganization energy. The reorganization energy consist of two components, one accounts for the changes in the geometry of the two molecules involved in the charge transfer and the other accounts for the changes in the polarization of the surrounding medium [27].

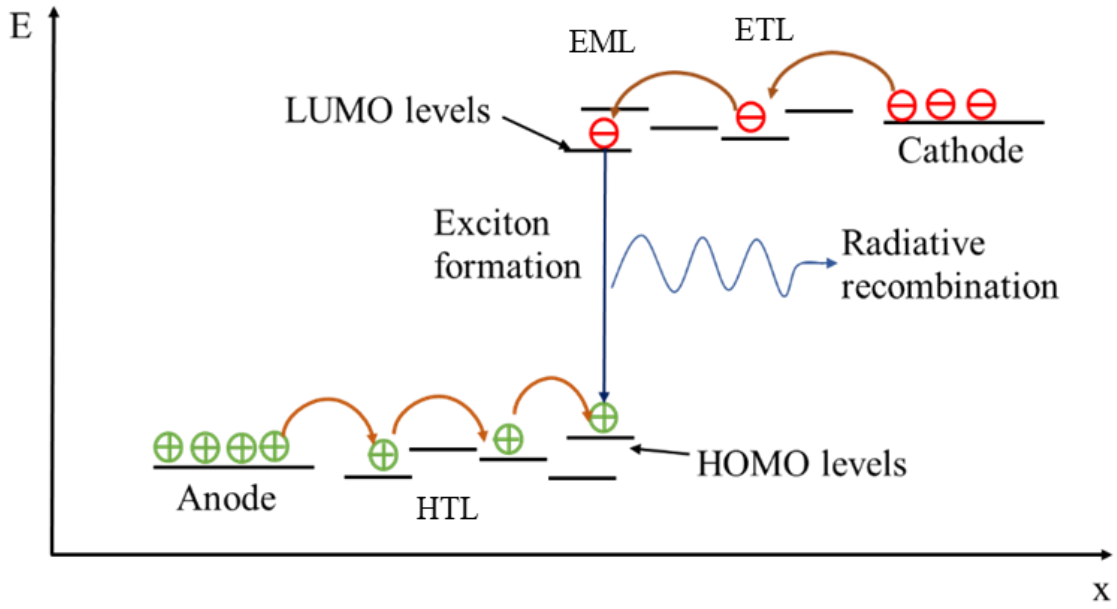

Figure 1.8: Schematic representation of charge carrier transport by the hopping mechanism.

Band-like model: for some organic molecules, the carriers move as a highly delocalized plane wave in a broad carrier band with a mean free path much larger than the nearest neighbor distance. These charge carriers exhibit metal-like transport properties, which are known as band-like transport. Crystals featuring delocalized charge carriers display band-like transport. However, lattice vibrations can disrupt the symmetry of the crystal, and hence decrease the mobility. Temperature is a crucial factor that governs the band-like transport, where lowering the temperature, reduces the lattice vibrations, thereby increase the carrier mobility.

Multiple trapping and release model: some organic thin films exhibit a polycrystalline structure rather than an amorphous or a crystalline structure [28]. In such materials, the charge carrier transport cannot be explained using the hopping or the band-like transport mechanisms. To understand the transport mechanism in such systems, multiple trapping, and release (MTR) theory are used. A key assumption in MTR is that the charge carrier transport occurs in

extended states, where most of the charge carriers are trapped in localized states. When the energy of the localized state is slightly lower than that of the mobility edge, this localized state behaves as a shallow trap, where the charge carriers can be released by thermal excitations. In MTR the number of charge carriers available for transport depends on the energy difference between the trap states and the extended state band as well as the temperature [26].

Various methods such as time of flight (TOF), dc current-voltage characteristics, Hall-effect, and delayed EL techniques have been used to study the mobility in organic semiconductors. In general, the charge carrier mobility depends on the external field according to **Equation 1.7**.

$$\mu(E,T) = \mu_0 e^{-\frac{\epsilon_0}{k_B T}} e^{\frac{\beta\sqrt{E}}{k_B T}} \tag{1.7}$$

E is the applied electric field, $\mu_0$is the low-field mobility, ε_0 is the activation energy at zero electric field and β is an empirically determined constant [18,29]. Mobility varies vary with temperature and at low temperatures, it is dominated by the effect of shallow traps. The mobility increases with increasing temperature due to thermally assisted hopping. At higher temperatures, the mobility behaves as T^{-n} and decreases with increasing temperature because of the phonon scattering [30].

The metal/organic interface is typically quasi-ohmic, and the charge injection rate from the metal is higher than the charge transport rate in the organic layer. Then the current depends solely on the transport properties, i.e., the mobility of the bulk organic layer rather than the injection process. This is known as space charge limited current (SCLC) regime and depends

on the injection barrier and the mobility. The current-voltage behaves, as demonstrated in **Equation 1.5** [21].

$$j \propto V^{\alpha} \tag{1.5}$$

The Value of α is determined by the operating regime, and it is typically linear or quadratic for SCLC regime. The device transits to the trapped charge limited current (TCLC) regime with high electric field due to rapid filling up of deep traps in the highly disordered organic layers. In this regime, the current behaves in a similar relationship described in **Equation 1.5** with a much higher α value ranging from 7 to 9 [31].

1.3.5. Exciton Formation and Recombination

The injected electrons and holes from the respective electrodes that drift through the organic layers under the influence of an electric field can experience two types of interactions, Coulomb interaction, and exchange interaction. Since the dielectric constant of organic materials are typically much lower ($\varepsilon_r \sim 3-5$) than that of inorganic semiconductors ($\varepsilon_r > 10$) [32,33], the Coulombic attraction ($F_{Coulomb} \sim \varepsilon_r^{-1}$) dominates over the exchange interaction and binds the electron and the hole together when they come closer. In general, this capture occurs before the electron and the hole reside on a single molecule; it is known as charge transfer (CT) state [34]. Getting further closer to each other, the bounded electron and hole inhabits the same molecule to form an exciton from CT states. OLED excitons are known as Frenkel excitons with an approximate radius of 10 Å and has a binding energy of 0.1- 1 eV [35]. This is different from TADF emission and is discussed later in this section.

The injected electron and hole have statistically independent spin states, and the electron-hole pair can form either an exciton with total spin *S=0* or *S=1*. A singlet exciton (SE) with *S=0* is an antisymmetric state under particle exchange. A triplet exciton (TE) of *S=1* has three possible symmetric states under particle exchange. Thus, the probability of forming a SE is 0.25, and that of a TE is 0.75. The spin state of the exciton governs the electroluminescence of the OLED, and when a photon is emitted, it needs to preserve the spin (*ΔS=0*). Since the ground state of most molecules is a singlet state [33], only SEs can decay radiatively to the ground state. Radiation from SEs is known as fluorescence, which is illustrated in **Figure 1.9a**; it is a very fast process occurring in 0.1 ns- 100 ns. Since the formation of SEs is limited to 25% of the total excitons, the efficiency of fluorescent OLEDs is also limited.

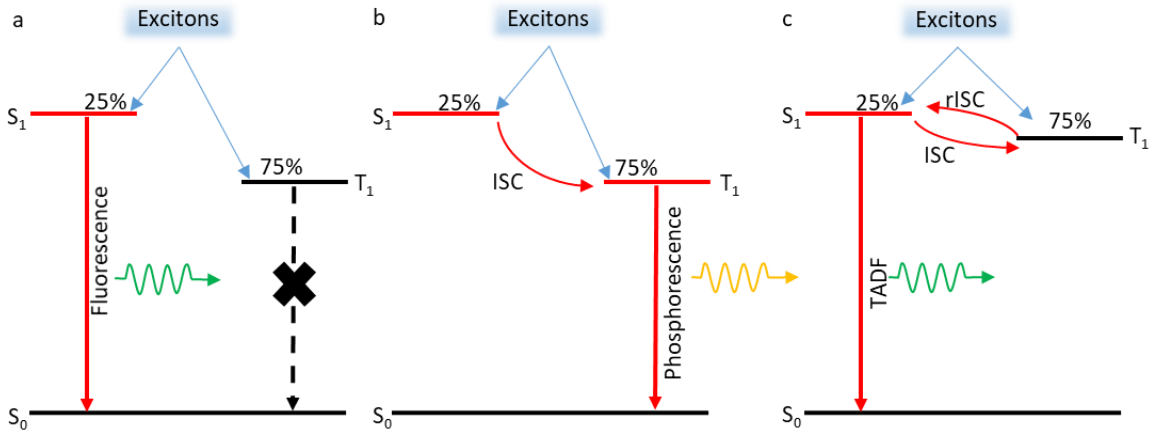

Figure 1.9: Representation of radiative decay processes in OLEDs, a) fluorescence, b) Phosphorescence, c) TADF.

Because of this limitation, harvesting triplets is the key to achieving high OLED efficiencies. Radiative decay of *S=1* TEs to the *S=0* ground state is quantum mechanically forbidden since it violates the spin selection rule (*ΔS=0*). However, radiative emission can be achieved from TEs via spin mixing, which can be accomplished either at the CT state or at the

exciton state. Spin mixing at CT state leads to a phenomenon called enhanced fluorescence and spin mixing at the exciton state results in phosphorescent [7] or TADF [8].

When a heavy atom such as platinum or iridium is present in the organic molecules, it enhances spin-orbit interaction [7,36]. Strong spin-orbit coupling results in an excited state with a mixed T/S character that allows radiative decay (phosphorescence) to ground state. Phosphorescence is significantly slower (1-100 μs) than fluorescence (1-100 ns) [37], but if the excitonic state mixing results in a radiative decay faster than the non-radiative rate, the luminescence can be efficient. OLED phosphorescence is demonstrated in **Figure 1.9b**. Since the phosphorescent OLEDs generate light from both SEs and TEs, it can reach an internal quantum efficiency of 100%.

TADF is a mechanism, first reported by Endo et al. in 2009 [8], that results in enhanced fluorescence. This is achieved with specially designed emitting molecules that have a small energy difference (ΔE_{ST} < 0.1 eV), comparable to k_BT between S1 and T1 so that S1 can thermally be populated via rISC (**Figure 1.9c**) [33]. The efficiency of the TADF process largely depends on rISC efficiency, which increases by minimizing $\Delta E_{ST,}$ which is governed by the electron exchange energy. The formation of intramolecular CT (ICT) state, where the electron and hole are decoupled to minimize the exchange energy enables E-type delayed fluorescence (i.e., TADF) in the emitter molecule [38]. The above condition is achievable by engineering the molecule, so the HOMO and LUMO are spatially separated. The special separation can be obtained within the TADF molecule[39] or by intermolecular excited states of donor-acceptor complexes known as exciplexes. During this bimolecular process, a partial charge transfer occurs from a donor-based orbital (D*/D) to an acceptor-based orbital (A*/A). The exciplex complex forms only in the excited state since the interaction between the donor, and the

acceptor is repulsive in the ground state and attractive in the excited state. This exciplex then decays radiatively or dissociate into its constituents [40]. But to have the charge transfer via rISC, a minimal interaction between the two orbitals should still exist rather than complete isolation of the two orbitals. The energy difference can also be minimized by careful selection of electron donor and acceptor with adapted energy levels [41].

Enhance fluorescence is another approach to achieve highly efficient OLEDs, where the mixing of singlets and triplets occurs at CT state rather than exciton state. In many fluorescent OLEDs, it is assumed the CT mixing rate is fast and governed by the strength of the coupling (10^{-4}-10^{-5} eV) between the singlet and triplet CT states [33,42].

For high efficiencies, guest-host systems are used in phosphorescent and TADF OLEDs, and the energy transfer in these guest-host systems can occur as cascade, Förster resonance (FRET) or Dexter resonance (DET) energy transfer. Cascade energy transfer is when the fluorescence emission of the host molecule is reabsorbed by the guest that then emits light. Obviously, this requires the emission spectrum of the host molecule to overlap with the absorption spectrum of the guest molecule for effective energy transfer. The transfer probability decreases with increasing separation between the guest and the host molecules. FRET and DET are two nonradiative processes of energy transfer from the host molecule to the guest molecule. In FRET, exciton on the host molecule induces a dipole in the guest molecule, and the induced donor field interacts with the induced acceptor dipole. This is a very fast process for an actual photon to be emitted by the host and absorbed by the guest, i.e., it is a virtual photon transfer process. The rate of FRET is proportional to $1/R^6$ (**Equation 1.8**) [43].

$$K_{FRET}(R) = \frac{1}{\tau_H}\left({}^{R_0}/_{R}\right)^6 \quad 1.8$$

Where R is the distance between the guest and the host molecules, R_0 is the Förster radius and τ_H is the average host exciton lifetime.

DET is another process, which occurs by exchanging an excited electron between the donor and acceptor molecules. Since it requires a direct electron exchange, the donor and the acceptor molecules need to have overlapped wavefunctions and be in proximity, typically with a separation less than 1 nm. Rate of energy transfer via DET is given by,

$$K_{DET}(R) \propto \exp\left(-\frac{2R}{L}\right) \quad 1.9$$

Where L represents the sum of the Van der Waals radii of the donor-acceptor molecules.

1.4. Measuring OLED Efficiency

OLEDs' efficiency plays an important role in energy consumption. Several parameters, such as luminous and power efficiencies, are measured for assessing OLEDs' performance. Luminous efficiency (η_L) measured in candelas per ampere (cd/A), is calculated from the ratio of the luminance measured in candelas per square meter (cd/m^2) and the current density that passes through the device (**Equation 1.10**). The Power efficiency measured in lm/W is the ratio of the luminous power emitted in the forward direction to the total electrical power required to drive the OLED at a given voltage (**Equation 1.11**).

$$Luminous\ Efficiency\ (\eta_L) = \frac{Luminance}{Current\ Density} \quad (1.10)$$

$$Power\ Efficiency\ (\eta_P) = \frac{Luminous\ Power}{Current\ \times Voltage} \tag{1.11}$$

Both efficiencies highly depend on the light perception of the human eye, which is described by the luminosity curve, also known as the photopic response curve shown in **Figure 1.10**. As seen, the human eye is most sensitive to light with wavelength 555 nm vanishing at 380 nm and 780 nm. This implies that it requires more energy to produce the same sensation in the blue and red regions of the visible spectrum than in the green.

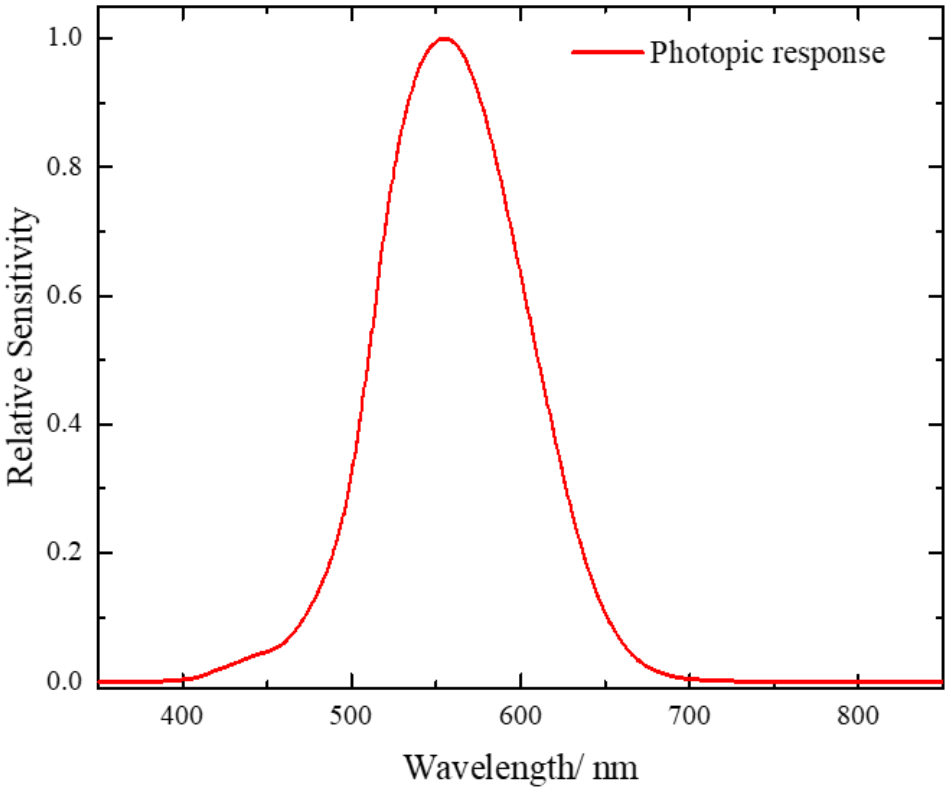

Figure 1.10: Photopic response of the human eye

EQE (η_{EQE}) is defined as the ratio between the number of photons emitted in the forward hemisphere and the number of electrons injected into the device. EQE is a

measurement that treats all the photons equally regardless of the photopic response (**Equation 1.12**).

$$\eta_{EQE} = \eta_{OUT} \times \eta_{IQE} \tag{1.12}$$

$$\eta_{IQE} = \gamma \times r_{ex} \times \eta_{PL} \tag{1.13}$$

Where η_{OUT} is the out-coupling efficiency, discussed in detail later, η_{IQE} is the IQE (**Equation 1.13**). The term γ is a charge balance factor, r_{ex} is the fraction of singlet or triplet exciton generation and η_{PL} is the photoluminescence (PL) quantum yield. For phosphorescent OLED η_{IQE} can be optimized to be 1.

η_{OUT} represents how much of the internally generated photons are extracted out of the device in the forward direction. In simplified ray tracing calculations,, the outcoupling efficiency is estimated by **Equation 1.14**, where *n* is the refractive index of the organic stack [44]. Total internal reflection (TIR) of the emitted light at various interfaces within the device and the substrate/air interface as well as surface plasmon excitation at the metal cathode are the prime light outcoupling losses. Having a refractive index ~1.7 for organic materials, **Equation 1.14** predicts that only 17% of the emitted photons can be forward extracted. Nearly 30% of the photons are externally waveguided in the substrate due to TIR at the glass/air interface (substrate mode), and 50% are lost to internal waveguiding in the high *n* organics and ITO anode + surface plasmon excitation at the metal cathode [44–46]. The plasmon loss decreases as the OLED's ETL thickness increases. Recent models computing the outcoupling factor treat the light emitting molecules as classically oscillating dipoles [47].

$$\eta_{OUT} \sim \frac{1}{2\,n^2} \tag{1.14}$$

Recovering these lost photons significantly improves the OLED's efficiency, and extensive research addressing the outcoupling is ongoing. Light trapped in the substrate can be extracted by using an external microlens array (μLA) attached to the back of the substrate without altering the device's electrical characteristics [48–50]. One approach to minimize the internally waveguided and plasmon loss is to fabricate the organic stack on a randomly structured or uniformly corrugated substrate [51,52]. Enhanced light outcoupling using nonplanar emissive layer is discussed in detail in chapter 2.

1.5. OLED Fabrication

Vacuum thermal evaporation (VTE) has been the most commonly used deposition technique for small-molecule OLED fabrication. VTE is a simple process where pure materials are evaporated from a crucible using thermal energy. The rate of evaporation is controlled by adjusting the temperature of the crucible; most OLED materials evaporate below 300 ^{0}C. [12] Thin films are fabricated by resistively heating materials in a vacuum chamber with a base pressure of ~ 10^{-6} – 10^{-7} Torr. The generated vapors condense on the substrate. The deposition rate and films' thickness are monitored using a quartz crystal microbalance (QCM) located inside the vacuum chamber and parameters such as tooling factor, material density, and the acoustic impedance must be adjusted prior to deposition.

VTE is advantageous over solution-based deposition techniques because highly efficient modern OLEDs are multilayer devices and VTE enables material (co)deposition without disturbing preceding layers. Another advantage of VTE is the cleanliness of the

process. OLEDs are highly sensitive to oxygen and water. Since VTE is carried out in high vacuum incorporation of water and oxygen is minimized. Moreover, particle contamination that leads to catastrophic electrical shorts is also minimized.

The main disadvantage of VTE is the scalability associated with vacuum systems and their cost. VTE line of sight path deposition is also problematic when considering large-area devices. In such devices, the deposition rate and thickness of each individual layer reduce away from the center. This leads to devices with non-uniform current and emission across the device. This issue can be eliminated either by moving the substrate or the evaporation source back and forth along a line. A critical drawback of thermal evaporation is the sensitivity of the organic layers to temperature and degradation occurring upon crystallization of overheated layers. This issue is clearly visible in materials such as BPhen.

PLEDs are fabricated using π conjugated organic polymers that decompose and degrade fast when subjected to high temperature; hence, polymer films cannot be fabricated using VTE. Spin-coating and other solution processing techniques are therefore used to generate such films. The polymers are dissolved in appropriate solvents, and following application, the substrate with the thin film is dried and baked at a necessary temperature to evaporate the excess solvent. One of the drawbacks of solution processing is the difficulty to precisely control the thickness of the film, which results in performance variations of nominally identical devices. Pressure, solution concentration, spin speed when spin coating, and wetting of the substrate are some of the parameters the film thickness depends on. An additional drawback is the limited number of proper solvents for π conjugated polymers and the difficulty of fabricating multilayer stacks without affecting preceding layers.

1.6. Dissertation Organization

This dissertation compiles five chapters. Chapter 1 provides a general introduction to OLEDs. Described are device structure, operating principle, efficiency measurement, and other details that are relevant to the work presented in later chapters.

Chapter 2 is modified from the author's published paper titled "Enhanced Light Extraction from OLEDs Fabricated on Patterned Plastic Substrates." This chapter discussed a novel approach to enhance light extraction from OLEDs using a corrugated substrate to minimize mostly internal waveguiding and surface plasmon losses. Green, blue, and white PhOLEDs fabrication and characterization are discussed, including cross-sectional studies using Focused Ion Beam (FIB) (performed by Dr. Matthew Lynn and the author), and the Atomic Force Microscopy (AFM) images provided by Rajiv Kaudal. Simulations performed in collaboration with Drs. Rana Biswas and Akshit Peer are presented. This work was published on Advanced Optical Material in 2018. Part of the work was published as an invited talk in Proceeding of the SPIE in 2017.

Chapter 3 is a continuation of chapter 2, where the discussion focuses on minimizing surface plasmon loss in OLEDs. Two approaches to achieve the latter are discussed: 1. increasing the distance between the metal cathode and the emissive layer and 2. using a shallow substrate corrugation that largely mitigates plasmon loss.

Chapter 4 is a manuscript in preparation. This chapter discusses the importance of deep blue OLEDs in display and lighting applications. The current approaches to achieve highly efficient blue OLEDs and the stability issue associated with blue OLEDs are also discussed. A new approach to achieving deep blue OLEDs is presented where the electroluminescence is

enhanced using exciplex emission. Part of this work was published as an invited talk in Proceedings of the SPIE in 2016. Chapter 5 summarizes the overall results.

1.7. References

(1) Bernanose, A. Electroluminescence of Organic Compounds. *Br. J. Appl. Phys.* **1955**, *6* (S4).

(2) Pope, M.; Kallmann, H. P.; Magnante, P. Electroluminescence in Organic Crystals. *J. Chem. Phys.* **1963**, *38* (8), 2042–2043.

(3) Tang, C. W.; Vanslyke, S. A. Organic Electroluminescent Diodes. *Appl. Phys. Lett.* **1987**, *51* (12), 913–915.

(4) Burroughes, J. H.; Bradley, D. D. C.; Brown, A. R.; Marks, R. N.; Mackay, K.; Friend, R. H.; Burns, P. L.; Holmes, A. B. Light-Emitting Diodes Based on Conjugated Polymers. *Nature* **1990**, *347* (6293), 539–541.

(5) Gustafsson, G.; Cao, Y.; Treacy, G. M.; Klavetter, F.; Colaneri, N.; Heeger, a J. Flexible Light-Emitting-Diodes Made from Soluble Conducting Polymers. *Nature* **1992**, *357* (6378), 477–479.

(6) Kido, J.; Hongawa, K.; OKuyama, K.; Nagai, K. White Light-Emitting Organic Electroluminescent Devices Using the Poly(N- Vinylcarbazole) Emitter Layer Doped with Three Fluorescent Dyes. *Appl. Phys. Lett.* **1994**, *64* (7), 815–817.

(7) Baldo, M. A.; O'Brien, D. .; You, Y.; Shoustikov, A.; Sibley, S.; Thompson, M. E.; Forrest, S. R. Highly Efficient Phosphorescent Emission from Organic Electroluminescent Devices. *Nature* **1998**, *395* (6698), 151–154.

(8) Endo, A.; Ogasawara, M.; Takahashi, A.; Yokoyama, D.; Kato, Y.; Adachi, C. Thermally Activated Delayed Fluorescence from Sn4+-Porphyrin Complexes and Their Application to Organic Light Emitting Diodes - A Novel Mechanism for Electroluminescence. *Adv. Mater.* **2009**, *21* (47), 4802–4806.

(9) Tohoku Pioneer Corporation http://global.pioneer/en/info/globalnetwork/japan/tohokupioneer/mainbusinesses/oled/ (accessed Aug 7, 2018).

(10) Innovative Flexible OLED screen displays | Street Communication http://streetcommunication.com/innovative-flexible-oled-screen-displays/ (accessed Aug 9, 2018).

(11) LG bends the limits of display technology - NotebookCheck.net News https://www.notebookcheck.net/LG-bends-the-limits-of-display-technology.230038.0.html (accessed Aug 9, 2018).

(12) Gaspar, D. J.; Polikarpov, E. *OLED Fundamentals*; CRC Press, 2015.

(13) Ishii, H.; Sugiyama, K.; Ito, E.; Seki, K. Energy Level Alignment and Interfacial Electronic Structures at Organic Metal and Organic/ Organicinterfaces. *Adv. Mater.* **1999**, *11* (8), 605–625.

(14) Tang, W.; Chao, Y.; Weng, X.; Deng, L.; Xu, K. Optical Property and the Relationship between Resistivity and Surface Roughness of Indium Tin Oxide Thin Films. *Phys. Procedia* **2012**, *32*, 680–686.

(15) Kavei, G.; Zare, Y.; Mohammadi Gheidari, A. Evaluation of Surface Roughness and Nanostructure of Indium Tin Oxide (ITO) Films by Atomic Force Microscopy. *Scanning* **2008**, *30* (3), 232–239.

(16) Tokito, S.; Noda, K.; Taga, Y. *Metal Oxides as a Hole-Injecting Layer for an Organic Electroluminescent Device*; 1996; Vol. 29.

(17) Meyer, J.; Winkler, T.; Hamwi, S.; Schmale, S.; Johannes, H. H.; Weimann, T.; Hinze, P.; Kowlasky, W.; Riedl, T. Transparent Inverted Organic Light-Emitting Diodes with a Tungsten Oxide Buffer Layer. *Adv. Mater.* **2008**, *20* (20), 3839–3843.

(18) Shinar, J.; Savvateev, V. Organic Light Emitting Devices - A Survey. In *Organic light emitting devices - A survey*; Shinar, J., Ed.; Springer, New York, 2004; pp 1–41.

(19) Sharma, A.; Kumar, P.; Singh, B.; Chaudhuri, S. R.; Ghosh, S. Capacitance-Voltage Characteristics of Organic Schottky Diode with and without Deep Traps. *Appl. Phys. Lett.* **2011**, *99*, 023301.

(20) Gartstein, Y. N.; Conwell, E. M. *High-Field Hopping Mobility in Molecular Systems with Spatially Correlated Energetic Disorder*; 1995; Vol. 245.

(21) Bassler, H.; Kohler, A. Charge Transport in Organic Semiconductors. In *Unimolecular and Supramolecular Electronics I. Topics in Current Chemistry*; Springer: Berlin, Heidelberg, 2011; Vol. 312, pp 1–66.

(22) Scott, J. C. Controlling Charge Injection in Organic Electronic Devices Using Self-Assembled Monolayers. *J. Chem. Phys.* **2003**, *21*, 3528.

(23) Barth, S.; Wolf, U.; Bä, H.; Mü, P.; Riel, H.; Vestweber, H.; Seidler, P. F.; Rieß, W. *Current Injection from a Metal to a Disordered Hopping System. III. Comparison between Experiment and Monte Carlo Simulation*.

(24) Cai, M. Organic Light-Emitting Diodes (OLEDs) and Optically-Detected Magnetic Resonance (ODMR) Studies on Organic Materials, 2011.

(25) Lenzlinger, M.; Snow, E. H. Fowler-Nordheim Tunneling into Thermally Grown SiO2. *J. Appl. Phys.* **1969**, *40* (1), 278–283.

(26) Lu, N.; Li, L.; Geng, D.; Liu, M. A Review for Polaron Dependent Charge Transport in Organic Semiconductor. *Org. Electron. physics, Mater. Appl.* **2018**, *61* (June), 223–234.

(27) Olivier, Y.; Lemaur, V.; Brédas, J. L.; Cornil, J. Charge Hopping in Organic Semiconductors: Influence of Molecular Parameters on Macroscopic Mobilities in Model One-Dimensional Stacks. *J. Phys. Chem. A* **2006**, *110*, 6356–6364.

(28) Horowitz, G. Organic Thin Film Transistors: From Theory to Real Devices. *J. Mater. Res.* **2004**, *19* (7), 1946–1962.

(29) Chen, B.; Liu, S. Measurement of Electron/Hole Mobility in Organic/Polymeric Thin Films Using Modified Time-of-Flight Apparatus. *Synth. Met.* **1997**, *91*, 169–171.

(30) Anderson, B. L.; Anderson, R. L. *Fundamentals of Semiconductor Devices*; McGraw-Hipp: Boston, 2005.

(31) Pope, M.; Swenberg, C. E. *Electronic Processes in Organic Crystals and Polymers*, 2nd ed.; Oxford University Press, 1999.

(32) Cho, N.; Schlenker, C. W.; Knesting, K. M.; Koelsch, P.; Yip, H. L.; Ginger, D. S.; Jen, A. K. Y. High-Dielectric Constant Side-Chain Polymers Show Reduced Non-Geminate Recombination in Heterojunction Solar Cells. *Adv. Energy Mater.* **2014**, *4* (10).

(33) Reineke, S.; Baldo, M. A. Recent Progress in the Understanding of Exciton Dynamics within Phosphorescent OLEDs. *Phys. Status Solidi A* **2012**, *209* (12), 2341–2353.

(34) Miura, N. Magneto-Spectroscopy of Semiconductors. In *Physics and Fundamental Theory*; 2011; pp 256–342.

(35) Forrest, S. R. Excitons and the Lifetime of Organic Semiconductor Devices. *Philos. Transitions A* **2015**, *373*, 1–7.

(36) Baldo, M. A.; Lamansky, S.; Burrows, P. E.; Thompson, M. E.; Forrest, S. R. Very High-Efficiency Green Organic Light-Emitting Devices Based on Electrophosphorescence. *Appl. Phys. Lett.* **1999**, *75* (1), 4–6.

(37) Minaev, B.; Baryshnikov, G.; Agren, H. Principles of Phosphorescent Organic Light Emitting Devices. *Phys. Chem. Chem. Phys* **2014**, *16*, 1719.

(38) Dias, F. B.; Bourdakos, K. N.; Jankus, V.; Moss, K. C.; Kamtekar, K. T.; Bhalla, V.; Santos, J.; Bryce, M. R.; Monkman, A. P. Triplet Harvesting with 100% Efficiency by Way of Thermally Activated Delayed Fluorescence in Charge Transfer OLED Emitters. *Adv. Mater.* **2013**, *25* (27), 3707.

(39) Zhang, Q.; Li, J.; Shizu, K.; Huang, S.; Hirata, S.; Miyazaki, H.; Adachi, C. Design of Efficient Thermally Activated Delayed Fluorescence Materials for Pure Blue Organic Light Emitting Diodes. *J. Am. Chem. Soc* **2012**, *134*, 8.

(40) Sarma, M.; Wong, K.-T. Exciplex: An Intermolecular Charge-Transfer Approach for TADF. *Appl. Mater. Interfaces* **2018**, *10*, 19279.

(41) Bui, T.-T.; Goubard, F.; Ibrahim-Ouali, M.; Gigmes, D.; Dumur, F. Thermally Activated Delayed Fluorescence Emitters for Deep Blue Organic Light Emitting Diodes: A Review of Recent Advances. *Appl. Sci.* **2018**, *8* (4), 494.

(42) Barford, W.; Bursill, R. J.; Makhov, D. V. Spin-Orbit Interactions between Interchain Excitations in Conjugated Polymers.

(43) Bulovic, V.; Shoustikov, A.; Baldo, M. A.; Bose, E.; Kozlov, V. G.; Thompson, M. E.; Forrest, S. R. *Bright, Saturated, Red-to-Yellow Organic Light-Emitting Devices Based on Polarization-Induced Spectral Shifts*; 1998; Vol. 287.

(44) Kim, J.-S.; Ho, P. K. H.; Greenham, N. C.; Friend, R. H. Electroluminescence Emission Pattern of Organic Light-Emitting Diodes: Implications for Device Efficiency Calculations. *J. Appl. Phys.* **2000**, *88* (2), 1073.

(45) Singh Mehta, D.; Saxena, K. Light Out-Coupling Strategies in Organic Light Emitting Devices. *Proc. ASID'06* **2006**, 198–201.

(46) Lu, M.-H.; Sturm, J. C. External Coupling Efficiency in Planar Organic Light-Emitting Devices. *Appl. Phys. Lett.* **2001**, *78* (13), 1927–1929.

(47) Gather, M. C.; Reineke, S. Recent Advances in Light Outcoupling from White Organic Light-Emitting Diodes. *J. Photonics Energy* **2015**, *5* (1), 057607.

(48) Park, J.-M.; Gan, Z.; Leung, W.; Lui, R.; Ye, Z.; Constant, K.; Shinar, J.; Shinar, R.; Ho, K.-M. Soft Holographic Interference Lithography Microlens for Enhanced Organic Light Emitting Diode Light Extraction. *Opt. Express* **2011**, *19* (S4), 786–792.

(49) Möller, S.; Forrest, S. R. Improved Light Out-Coupling in Organic Light Emitting Diodes Employing Ordered Microlens Arrays. *J. Appl. Phys.* **2002**, *91*, 3324.

(50) Wei, M.-K.; Su, I.-L.; Matterson, B. J.; Lupton, J. M.; Safonov, A. F.; Salt, M. G.; Barnes, W. L.; W Samuel, I. D. Method to Evaluate the Enhancement of Luminance Efficiency in Planar OLED Light Emitting Devices for Microlens Array. *Opt. Express* **2004**, *12* (23), 5777–5782.

(51) Zhou, J.; Ai, N.; Wang, L.; Zheng, H.; Luo, C.; Jiang, Z.; Yu, S.; Cao, Y.; Wang, J. Roughening the White OLED Substrate's Surface through Sandblasting to Improve the External Quantum Efficiency. *Org. Electron.* **2011**, *12*, 648–653.

(52) Hippola, C.; Kaudal, R.; Manna, E.; Xiao, T.; Peer, A.; Biswas, R.; Slafer, W. D.; Trovato, T.; Shinar, J.; Shinar, R. Enhanced Light Extraction from OLEDs Fabricated on Patterned Plastic Substrates. *Adv. Opt. Mater.* **2018**, *6* (4), 1–11.

CHAPTER 2. ENHANCED LIGHT EXTRACTION FROM OLEDS FABRICATED ON PATTERNED PLASTIC SUBSTRATES

Modified from a manuscript published in *Advanced Optical Materials*

Chamika Hippola *[§], Rajiv Kaudal *[§], Eeshita Manna [§¥], Teng Xiao [§], Akshit Peer [§¥£], Rana Biswas *[§¥£], W. Dennis Slafer [ǂ], Tom Trovato [†], Joseph Shinar*[§], and Ruth Shinar[¥£]

* Physics and Astronomy Department, Iowa State University, Ames, IA 50011, USA

[§] Ames Laboratory, US Department of Energy, Iowa State University, Ames, IA 50011, USA

[¥] Electrical and Computer Engineering Department, Iowa State University Ames, IA 50011, USA

[£] Microelectronics Research Center, Iowa State University Ames, IA 50011, USA

[ǂ] MicroContinuum, Inc., Cambridge, MA 02138, USA

[†] Trovato Manufacturing, Inc., Victor, NY 14564, USA

2.1. Abstract

A key scientific and technological challenge in organic light-emitting diodes (OLEDs) is enhancing the light outcoupling factor η_{out}, which is typically < 20%. This paper reports experimental and modeling results of a promising approach to strongly increase η_{out} by fabricating OLEDs on novel flexible nanopatterned substrates that result in a > 2× enhancement in green phosphorescent OLEDs (PhOLEDs) fabricated on corrugated polycarbonate (PC). The external quantum efficiency (EQE) reaches 50% (meaning η_{out} ≥50%); it increases 2.6x relative to a glass/ITO device and 2× relative to devices on glass/poly(3,4-ethylenedioxythiophene): polystyrene sulfonate (PEDOT:PSS) or flat PC/PEDOT:PSS. A significant enhancement is also observed for blue PhOLEDs with EQE

1.7× relative to flat PC. The corrugated PC substrates are fabricated efficiently and cost-effectively by direct room-temperature molding. These substrates successfully reduce photon losses due to trapping/waveguiding in the higher index organic + anode layers and possibly substrate, and loss to surface plasmon excitation at the metal cathode. Focused ion beam (FIB) gauged the conformality of the OLEDs. Dome-shaped convex nanopatterns with a height of ~280–400 nm and pitch ~750–800 nm, were found to be optimal. Substrate design and layer thickness simulations, reported first for patterned devices, agree with the experimental results that present a promising method to mitigate photon loss paths in OLEDs.

2.2. Introduction

OLEDs are widely used in displays, from smartphones to large TVs, as they provide thinner, brighter displays with vibrant colors and infinite contrast. They are also being developed for solid-state lighting (SSL) applications. Unlike the bright point source emission of inorganic LEDs, OLEDs provide a cool or warm diffuse white source of light that is by default suitable for large area illumination. One of the primary criteria for OLEDs in SSL, together with cost reduction and increased stability, is improved light outcoupling (and hence efficiency), which remains a key scientific and technological challenge. The US Department of Energy (DOE) goal is an outcoupling factor (the ratio of the number of photons emitted into the "forward" hemisphere to the number of photons generated in the OLED) η_{out} = 70% by 2020, matching or exceeding that of current alternatives. The EQE (the ratio of the number of photons emitted into the "forward" hemisphere to the number of electrons injected into the OLED) is given by [1,2]

$$EQE = \eta_{out}\gamma r_{ex}\Phi_{PL} \tag{2.1}$$

Where

$$\eta_{out} = EQE/IQE \tag{2.2}$$

where γ and Φ_{PL} are the charge balance factor and intrinsic PL quantum yield, respectively. r_{ex} is the radiative exciton recombination factor, which is ≈ 0.25 for fluorescent materials, where only singlet excitons decay radiatively, but can approach 1 for phosphorescent materials, where both singlet and triplet excitons decay radiatively. IQE is the internal quantum efficiency, i.e., the ratio of the number of photons generated in the OLED to the number of electrons injected into it. It should be emphasized that while EQE can be measured directly, that is not the case for η_{out} or IQE, i.e., their determination is invariably model-dependent [3–6]. As IQE ≤ 1, η_{out} ≥ EQE. In some very specific cases (e.g., the green phosphorescent OLEDs, PhOLEDs, described below) the parameters γ and Φ_{PL} can be adjusted to approach 1 by carefully choosing the materials and device architecture. Hence, almost 100% IQE is apparently achievable [7–9].

The power efficiency of white PhOLEDs is already ≈ 100 lm W^{-1}, comparable to that of LEDs and fluorescent tubes. This efficiency, however, is still far from the PhOLEDs' full potential with the main challenge being η_{out} [2,10–12]. The outcoupling is compromised by trapped or waveguided light loss inside the device and in the substrate due to refractive index mismatch, as well as losses to surface plasmons at the metal electrode [2,10–12]. Depending on the ETL thickness, up to 60% of the generated photons are lost mostly to (i) total internal reflection (TIR) at the glass/ITO interface (refractive indices n_{glass} ≈ 1.5, n_{ITO} ≈ 2.0) and subsequent waveguiding and loss in the organic + ITO layers ("internal waveguiding"), and (ii) surface plasmons at the metal cathode [11,12]. Another ≈10–25% of the photons are trapped inside the

glass substrate due to TIR at the glass/air interface and subsequent external waveguiding to the glass edges [11–13]. Thus, $\eta_{out} \leq 20\%$ with the conventional structure of through-the-glass-bottom-emitting-OLEDs [11,12].

Extensive research has been performed in an attempt to improve η_{out} via different approaches. To extract the light lost in glass substrate modes, various sizes of microlens arrays (μLAs) were attached at the back of the glass, [13,14] TiO_2 nanoparticles [15] were embedded in the substrate, or high index substrates [16] replaced the glass. A maximal 2× enhancement in the EL was achieved with a structured μLA when the μLA area exceeded that of the OLED pixel [13].

Recovering the 40–60% light internally trapped in the organic + anode layers and/or lost to surface plasmons at the metal cathode remains particularly challenging. Use of high n ≈1.7 polyimide (PI) with embedded air voids as scattering centers resulted in an η_{out} enhancement of 65% for green OLEDs; for white OLEDs (WOLEDs) EQE increased 1.6× from 11.9% to 19%, and the power efficiency increased from 18 to 32 lm W^{-1} at 100 cd m^{-2} [17]. The use of colorless PI in a more complex procedure resulted in an increase of 1.9× in EQE, from 13.8% with glass/ITO to 26% [18]. Subanode designs with a nondiffractive dielectric scattering grid layer (e.g., SiO_2 with n ≈ 1.5 or air grid in TiO_2, n ≈ 2.2) between the transparent anode and the substrate were shown to enhance outcoupling of the internally waveguided light into the substrate [19]. An increase in EQE from ≈ 15% to ≈ 18% in a green PhOLED was reported. It increased to 40% with the addition of a μLA. The respective power efficiency increased from 36 to 43 to 95 lm W^{-1} with the μLA [20]. In a more complex design, a silver nanowire mesh in nanoimprinted PET substrate with a poly(3,4-ethylenedioxythiophene):

polystyrene sulfonate (PEDOT:PSS) anode and an aperiodic nanostructure in the WOLED stack + μLA resulted in EQE = 46.3% (2.6×) at 1000 cd m^{-2} [21].

Another recent study focused on 1D grating, 2D grating, and quasi-random biomimetic nanostructures of PEDOT:PSS on flat PET/ITO where the highest EQE achieved was 12.5% (*vs.* 8.3% for a flat device) for a green OLED [22]. Xiang et al. [23] employed a built-in Ag network electrode in patterned PET substrate, with the pattern apparently being on the "blank side." Hence, the enhancement due to this pattern is akin to a μLA used for extraction of substrate modes only [13]. Xu et al. [24] explored flexible transparent OLEDs with a biomimetic nanostructured metal/ dielectric composite electrode on a flat plastic. The pattern height was restricted to a single low value of h ≈ 50 nm and a pseudo-period 250 nm; conformality was not addressed. Chen et al. [25] described OLEDs fabricated on multilayer high conductivity/ low conductivity PEDOT:PSS spin-coated on an ITO micromesh. However, the height of the ITO micromesh could only be roughly estimated at ≈ 40 nm. The application of PEDOT:PSS reduced the corrugation height from 40 to 20 nm, and the EQE was ≈ 22%.

None of the foregoing studies explored the dependence of η_{out} on the substrate pattern height or pitch and only Chen et al. [25] evaluated the conformality of the OLED layers deposited on a micromesh ITO, though his structure required an external hemispherical lens for enhancing the EQE above ≈ 22%. Importantly, none evaluated the dependence of the OLED performance on the HTL or ETL thickness. In addition, none of these studies explored the separate roles of the nanopatterns in disrupting internal waveguiding versus disrupting surface plasmons.

Surface plasmon losses remain a major issue. A design of broad periodicity and random orientation in a buckling structure was shown to outcouple the surface plasmon mode in a green OLED [26]. A thicker *n*-doped ETL (with the doping needed to reduce the higher resistance associated with thicker layers) that increases the distance between the emitting layer and the metal cathode also weakens this loss channel [11,12].

In this work enhanced light extraction exceeding 2× was achieved via fabrication of PhOLEDs with a PEDOT:PSS anode on flexible patterned polycarbonate (PC) substrates, with an effort to grow the OLED stack conformally on the patterned, scattering structure. Such structures disrupt the internal waveguiding in the organics + anode and reduce loss to surface plasmons at the metal cathode. The latter was also achieved with a thicker ETL that increases the distance between the EML and the metal cathode. The PhOLEDs were broadly characterized via optoelectronic, structural, and chemical analyses. Flexible substrates of PET/CAB (cellulose acetate butyrate) were also studied.

Flexible substrates have many advantages over standard glass substrates. They are lightweight, amenable to roll-to-roll (R2R) fabrication, cost-effective, and have a relatively high refractive index $n_{PC} \approx 1.6$. Consequently, they can play a crucial role in advancing OLED-based SSL and wearable devices of interest in medical and sensing applications.

Conductive ITO is extensively used as the anode in OLEDs because of its high transparency in the visible and preferred work function for hole injection into the organics [27]. However, its refractive index $n_{ITO} \approx 2$ is high and exacerbates the internal waveguiding losses. Unlike ITO, PEDOT:PSS ($n_{PEDOT:PSS} \approx 1.5$) does not present a refractive index mismatch with

the substrate [28,29], resulting in more light extraction due to reduced internal waveguided losses in the organic + anode layers [28].

Initially PEDOT:PSS was used only as a buffer layer between ITO and the organic layers due to its lower conductivity but efficient hole injecting properties [30,31]. However, it has become increasingly attractive as an anode with the commercial availability of high conductivity PEDOT:PSS and with conductivity enhancing approaches obtained via mixing or treating with additives such as ethylene glycol (EG) [32–37]. Cai et al. [28,34] showed that a spin-coated double layer PEDOT:PSS anode treated with EG yields superior anodes for green PhOLEDs in comparison to ITO. In future commercial devices, however, an integrated substrate/ anode with a metal mesh conductor and a thin ITO is envisioned.

2.3. Results and Discussion

2.3.1. Substrate Pattern and Anode

2.3.1.1. Characterization of nanopattern substrates

All PC substrates had convex, dome-shaped nanopatterns (**Figure 2.1**) with the height h of the features ranging from 80 to 650 nm and a constant pitch a ≈ 750–800 nm. Substrates based on PET/CAB with concave features had h ≈ 220–600 nm and a ≈ 0.75–3 μm; the concave PET/CAB substrates were found to be inferior to the convex PCs. As mentioned, the nanopatterns on the substrates are expected to produce corrugation throughout the OLED stack, which should increase forward light extraction. This increased extraction is due to random changes in the incident angle at the organic + anode/substrate and possibly also substrate/air interfaces. Importantly, the corrugation reduces also surface plasmon-related losses at the metal cathode.

The different plastic substrates were imaged via atomic force microscopy (AFM) for determining h and a. **Figure 2.1** shows 3D AFM images of a nanopatterned PC substrate with h ≈ 320 nm and a ≈ 750 nm, and a PET/CAB/ITO with h ≈ 250 nm and a ≈ 1.75 μm.

2.3.1.2 Anode fabrication

Figure 2.2 also shows a focused ion beam (FIB) image of an ITO section on a corrugated PET/CAB. As seen, there are some damaged areas, which may be due to stress induced in the thick (>100 nm) ITO deposited on the patterned substrates and/or damage to the corrugated surface occurring before or during ITO deposition.

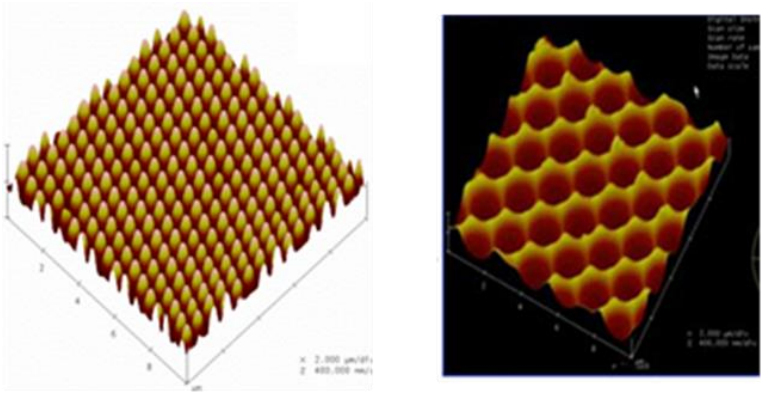

Figure 2.1: Left: AFM image of a 10x10 μm^2 convex PC with h ~320 nm and a ~750 nm; Right: AFM image of a 10x10 μm^2 concave PET/CAB with h ~250 nm and a ~1.75 μm coated with ITO.

To reduce the surface tension of PEDOT:PSS at the interface with the hydrophobic plastic substrate, the polymer solution has to be treated with an additive. The wetting improves when the aqueous PEDOT:PSS solution is mixed with alcohols and/ or fluorosurfactants [38]. Indeed, the addition of 25 vol.% or 50 vol.% ethanol increases the wettability of PEDOT:PSS on PC but reduces the conductivity significantly. The turn-on voltage of a standard NPB (N,N′-di(1-naphthyl)-N,N′-diphenyl-(1,1′-biphenyl)-4,4′- diamine)/ Alq_3 (tris(8-

hydroxyquinolinato)/ CsF/Al OLED increased to 7.4 – 10.2 V versus 2.9 V for a similar OLED on glass/ITO. By contrast, the addition of a fluorosurfactant, e.g., Zonyl FS30 or Capstone FS35, reduces the surface tension considerably without affecting the conductivity of the PEDOT:PSS film [39]. Some studies demonstrated an enhanced conductivity of PEDOT:PSS even upon adding a fluorosurfactant at a very low concentration [40]. Here PEDOT:PSS was mixed with EG and 0.5–1 vol.% of Zonyl FS30 or Capstone FS35 fluorosurfactant. For a double layer PEDOT:PSS anode with each layer spin-coated at 3000 rpm for 30 s, a sheet resistance of ≈170 Ohm sq−1 was achieved, which is slightly higher than the sheet resistance reported by Cai et al. [28] A double layered PEDOT:PSS film fabricated as described above [28], and in particular a single layer spin-coated at 6000 rpm proved to be optimal anodes for green and blue PhOLEDs, depending on the device structure.

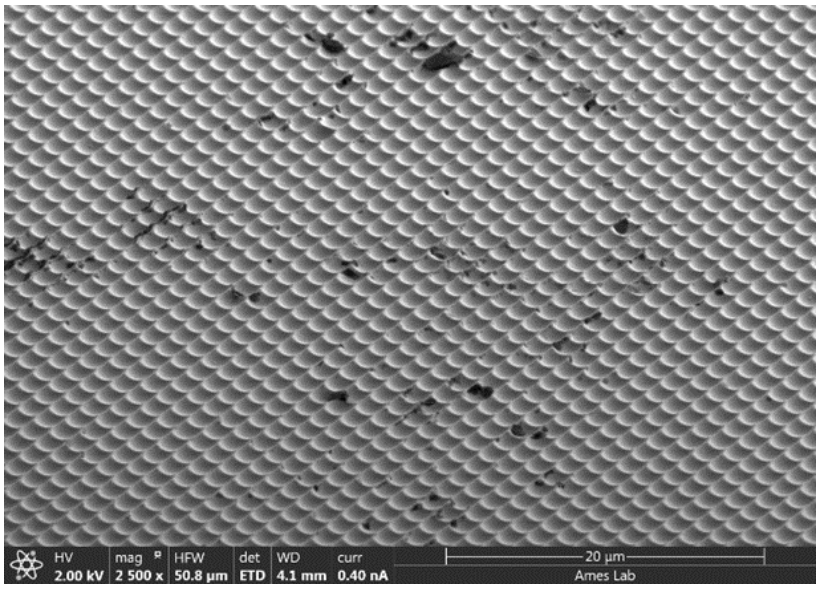

Figure 2.2: FIB image (with 20 µm scale bar) of ITO on corrugated PET/CAB showing damaged areas.

Mapping the current distribution on the patterned double-layer PEDOT:PSS anode via conductive AFM (c-AFM) (**Figure 2.3**) demonstrated a nonuniform current distribution with, as expected, a higher current through the troughs and a lower current at the nanopattern peaks. Thinner PEDOT:PSS showed a more uniform current distribution.

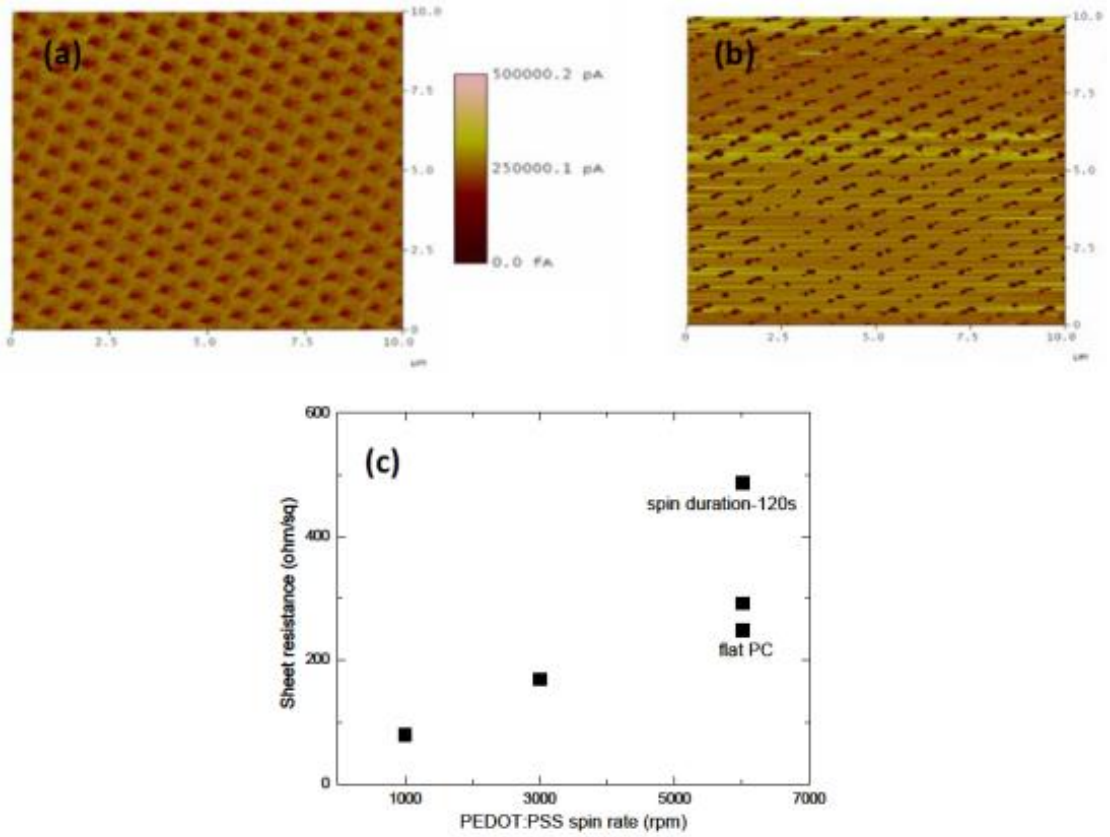

Figure 2.3: Conductivity AFM images of 2–layered PEDOT:PSS spin-coated on patterned PC with h ~320 nm and a ~750 nm for 30 s. (a) 3,000 rpm (~65 nm) and (b) 6,000 rpm (~40 nm). (c) The sheet resistance of two PEDOT:PSS layers coated on flat and patterned PC substrates at different spin coating rates and durations. The spin duration was 30 s unless otherwise noted.

Figure 2.3 also shows the sheet resistance of PEDOT:PSS layers prepared at different spin rates and durations. While the resistance of a thin PEDOT:PSS anode is higher than that of the typical ≈130 nm ITO, it proved important in demonstrating the promise of PhOLEDs on

corrugated flexible substrates, as thicker solution-processed coatings were not uniform. They reduced the corrugation, i.e., filling more of the troughs, as indicated in **Table 2.1** (measurement by AFM).

Table 2.1: Pattern heights before and after PEDOT:PSS spin coating at various rates.

Substrate	**PEDOT:PSS[a)] solution + additive**	**PEDOT:PSS spin coating speed and duration for each of the two layers**	**Height measured after coating (nm)**
(1) PC-320	6 vol.% EG+ 1 vol.% Capstone FS35 fluorosurfactant	1000 rpm for 30 s	60
		3000 rpm for 30 s	141-149
		6000 rpm for 30 s	194-203
		6000 rpm for 60 s	208-218
		6000 rpm for 120 s	219-237
		6000 rpm for 30 s Single layer	**~300**
(2) PC-280		6000 rpm for 120 s	166-173
		6000 rpm for 120 s 3 layers	102-112

*The anode consisted of two PEDOT:PSS layers unless otherwise mentioned

Table 2.2 shows that the corrugation further decreased following device fabrication on PC-320 (i.e., PC with corrugation height h ≈ 320 nm). Importantly, the thin single layer PEDOT:PSS (≈20–30 nm) spin-coated at 6000 rpm for 30 s did not result in a change in the corrugation height within the ≈ 8% experimental error, i.e., the PEDOT:PSS was deposited conformally.

Table 2.2: Corrugation height of the pattern before and after two-layer PEDOT:PSS coating and PhOLED fabrication and the associated enhancement factor.

Sample		**Corrugation height**		**Spin conditions and luminous efficiency enhancement factor**
	Before device fabrication (nm)	Following PEDOT:PSS coating (average)	After device fabrication (nm)	
PC-320	320	~200		6000 rpm/30 s
PC-320	320	~215		6000 rpm/60 s
PC-320	320	~230		6000 rpm/120 s
PC-320 green	320		135-170	~1.6x
PC-135 blue	135 (inverted)		118	~1.5x
PC-320 blue	320		190	~3.0

2.3.2. Evaluation of the Conformal Structure

To assess the conformality of the OLED stack, we used FIB. A thick ITO layer (≈130 nm) or a 2-layer PEDOT:PSS anode (≈65 nm) resulted in a reduced corrugation of the OLED stack and Al cathode for green PhOLEDs on PC-320 (**Table 2.2**). By contrast, devices with the thin single PEDOT:PSS layer on PC-320 or ITO on the PET/CAB did not show such a reduction as seen in **Figure 2.4**, though some thickness variations across the features were

observed. The more conformal structure may be related to the solution-processed thinner anode on PC-320 and larger a/h ratio of the PET/CAB substrate.

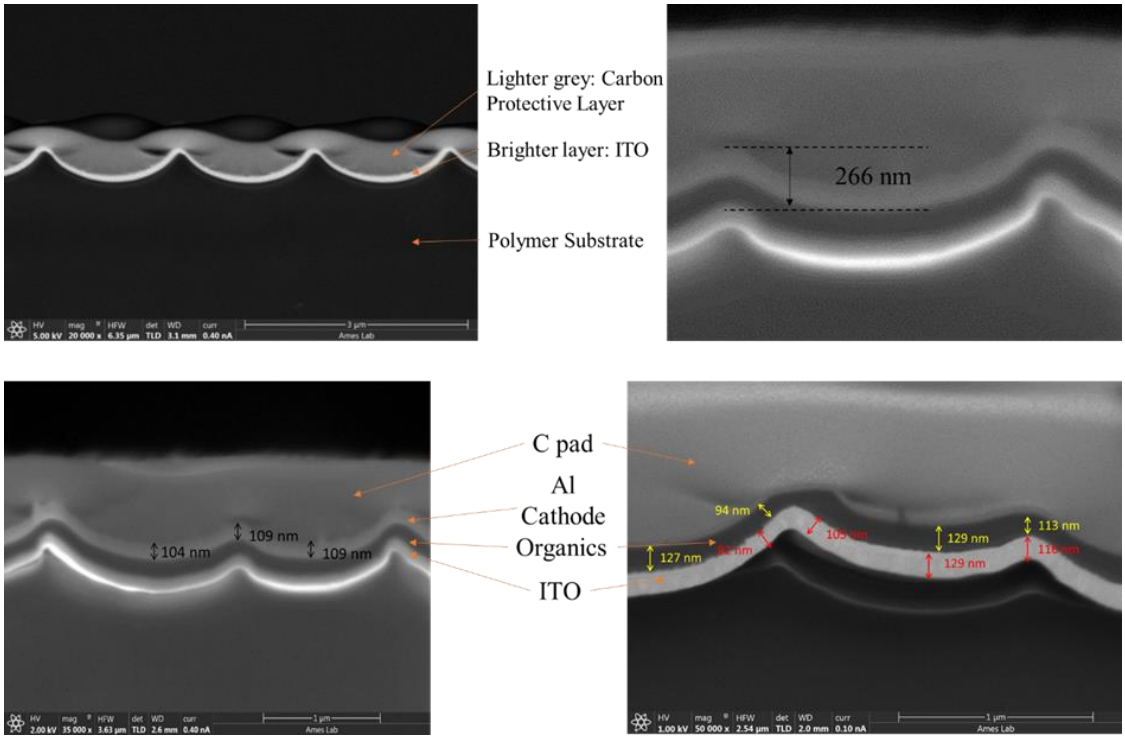

Figure 2.4: FIB images of patterned ITO and a PhOLED fabricated on PET/CAB with a ~1.75 μm and h ~250 nm. The images show that the OLED structure is largely conformal with the substrate's corrugation (see text).

The expected organic stack thickness of this specific device, based on the quartz crystal monitor in the evaporation chamber within the glovebox, is ≈125 nm. The observed thickness was ≈130 nm in the troughs and ≈120 nm on the top of the corrugation, a difference of only ≈8%. On the slopes, we measured an average of ≈100 nm, a reduction of ≈23% in the thickness. The similarity of the thickness of the corrugated and flat layers is surprising due to the significantly larger surface area of the former but appears to be related to the a/h ratio that is high in this case. We note that for further development of this approach for future applications tilting and rotation of the substrate may be of benefit. Importantly, the corrugation height

measured at the top Al layer was ≈ 265 nm, similar to h ≈ 250 nm measured for the bare substrate by AFM. The Al thickness was ≈ 109 nm. We next show results of enhanced outcoupling in patterned PhOLEDs using a PEDOT:PSS anode.

2.3.3. Green and Blue PhOLEDs

2.3.3.1. Green PhOLEDs design 1: Double layer PEDOT:PSS anode

To determine the optimal h for maximum light extraction, green tris (2-phenylpyridine) iridium(III) ($Ir(ppy)_3$)-based PhOLEDs with two different structures were evaluated. In one, the structure was PEDOT:PSS (two layers) anode / MoO_3 (1 nm)/10 wt.% MoO_3:NPB (22.5 nm)/NPB (22.5 nm)/6 wt.% $Ir(ppy)_3$:CBP (11 nm)/BPhen (40 nm)/LiF (1 nm)/Al (100 nm).

Such structures were fabricated on different patterned PCs. The OLED layers were thermally evaporated on the spin-coated double layer PEDOT:PSS anode. Light extraction increased with the corrugation height of the convex patterned PCs for heights $\approx 250 \leq h \leq 400$ nm as compared to a flat PC; a maximum luminous efficiency of ≈127 cd A^{-1} was achieved for such optimized devices (**Figure 2.5d**). This efficiency is ≈1.6x higher than that of the device on a flat PC. EQE similarly increased ≈1.6× from ≈22% to 36%. The OLED efficiency was actually reduced for patterns with h ≈215 and ≈500 nm. Importantly, the angular dependence of the EL spectra for these green PhOLEDs deviates only slightly from Lambertian (**Figure 2.5b**), and no significant change in the normal emission spectrum was observed (**Figure 2.5a**).

As described later, the devices further improved significantly with a thick HTL, which likely masked fine structural or other defects in the corrugated plastic substrates.

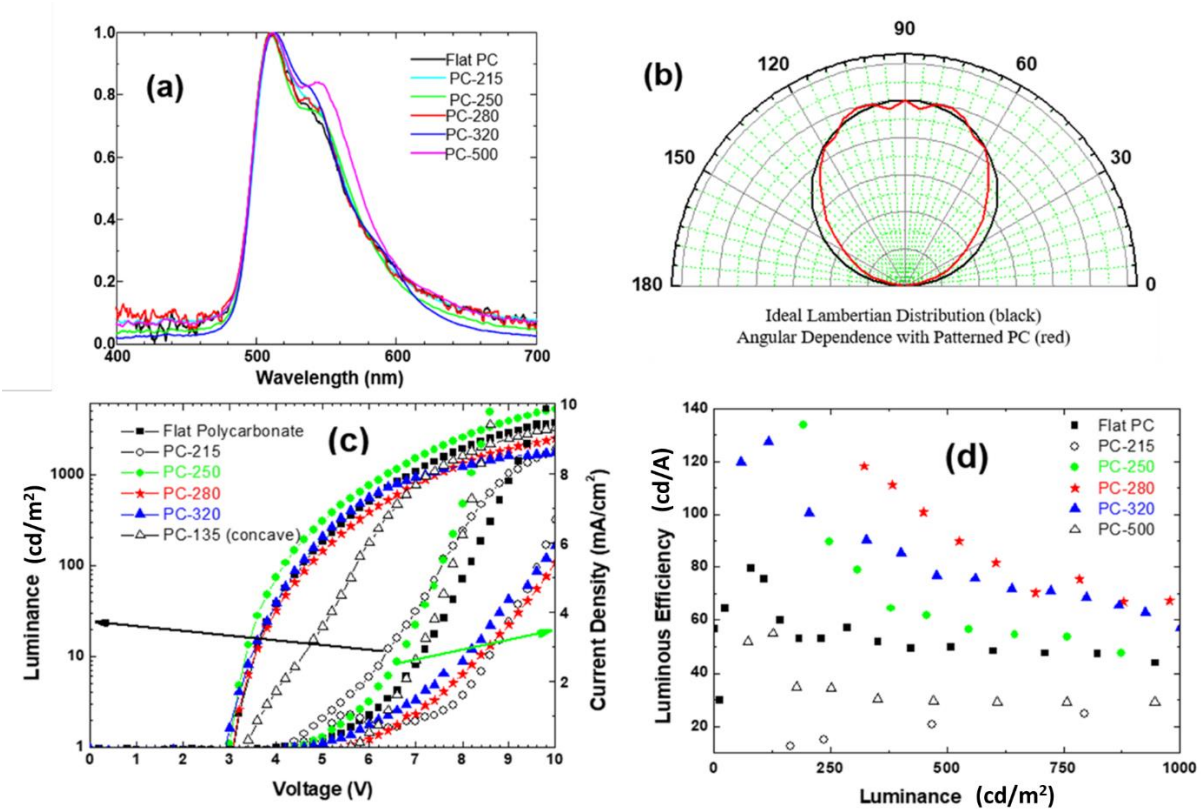

Figure 2.5: (a) Normalized EL spectra for flat and patterned PC substrates (b) Comparison of the angular distribution of the EL spectrum of an OLED fabricated on patterned PC with ideal Lambertian profile (c) J-L-V curves and (d) Luminous efficiency vs. brightness of $Ir(ppy)_3$-based PhOLEDs; corrugation heights range from 215 nm (PC-215) to 500 nm (PC-500).

As seen in **Figure 2.5**, the peak luminous efficiency was the highest for the devices on PC-280 and PC-320 (i.e., h ≈ 280 and 320 nm, respectively). **Table 2.3** summarizes the results. We note that the roll-off of the efficiency and the devices' degradation were fast as they were not encapsulated, and the PC is relatively porous to water vapor and oxygen. Permeated oxygen, whose level increases for the corrugated substrates due to their larger surface area, quenches the phosphorescence [41]. Hence, encapsulated devices would not only be much more stable but would also exhibit higher efficiencies, as the phosphorescent quenching by O_2 will lessen. Additionally, as shown by FIB analysis, the OLED stack, including the Al cathode exhibited a corrugated structure, though the height of the corrugation decreased, as shown in

Table 2.2. This situation is likely due to the nonuniform ≈65 nm PEDOT:PSS layer (**Table 2.1**) and was also observed for thick (>100 nm) ITO on PC. For better enhancement, the fidelity of the conformal structure needs to be highly controlled, as described next.

Table 2.3: Comparison of attributes of green and blue PhOLEDs fabricated on different substrates with two layers of PEDOT:PSS (total thickness ~ 65 nm) as the anode.

	Sample	Turn on voltage (V)	Max. luminous efficiency (cdA^{-1})	Corresponding EL (cdm^{-2})	Luminous Efficiency @ 1000 cdm^{-2}
Green $Ir(ppy)_3$-based PhOLEDs	Flat PC	3.0	80	79	44
	PC-215	4.0	28	1321	27
	PC-250	3.0	89	247	47
	PC-280	3.0	118	323	64
	PC-320	3.0	127	118	57
	PC-500	3.4	54	127	29
Blue FIrpic-based PhOLEDs	Flat PC	3.3	29.2	110	9.6
	PC-320		87	140	17.9
	PC-135		45.2	408	30.9

2.3.3.2. Green PhOLEDs design 2: Single layer PEDOT:PSS anode and thicker HTL and ETL

A single layer PEDOT:PSS anode resulted in a more uniform current distribution and the most conformal OLED stack; however, the sheet resistance increased up to 1.3 kΩ sq^{-1}. The increased resistance indicates that other means for enhanced conductivity are necessary. We fabricated devices on such a thin anode with the addition of a thin HAT-CN (dipyrazino[2,3- f:2′,3′-h]quinoxaline-2,3,6,7,10,11-hexacarbonitrile) layer and a thicker HTL to minimize the effect of substrate structural or other defects. We also employed a thicker ETL

that enhances the device performance by reducing surface plasmon excitation loss due to increased EML/metal electrode distance.

The PhOLEDs structure was Substrate/Anode/HAT-CN (5 nm)/ 10 wt.% MoO_3: TAPC (120 nm)/ HAT-CN (5 nm)/ TAPC (20 nm)/ 6 wt.% $Ir(ppy)_3$: mCP (20 nm)/TmPyPb (20 nm)/ 20 wt.% CsF: TmPyPb (40 nm)/ LiF (1 nm)/ Al (100 nm).

This structure is a result of device optimization via change of layer thickness and HTL doping level, including employment of HAT-CN layers, which improved hole injection. 20 wt.% CsF doping of the ETL improved the device, which is in accordance with earlier reports [42] a lower concentration of 2 wt.% resulted in inferior results.

Experiments with various levels of the CsF dopant indicated that 20 wt.% is suitable for *n*-doping TmPyPb (3,3′-[5′-[3-(3-pyridinyl) phenyl][1,1′:3′,1″-terphenyl]-3,3″-diyl]bispyridine), but not BPhen (4,7-diphenyl-1,10-phenanthroline) or TPBi (2,2′,2″-(1,3,5-benzinetriyl)-tris(1-phenyl-1-H-benzimidazole)) ETLs. The substrate/anode was either glass/ITO, glass/PEDOT:PSS, flat PC/PEDOT:PSS, or PC-320/PEDOT:PSS (PC-320 is of h ≈ 320 nm, a ≈ 800 nm). We note that the reported values of the HOMO and LUMO levels of HAT-CN (−7.5 and −4.4 eV, respectively) are very deep [43], indicating deep electron trap and high hole barrier. As the HAT-CN layers are thin, however, a possible scenario for the experimentally observed very good hole transport properties of HAT-CN may be a change in the energetics due to electron trapping by some HAT-CN molecules, which should raise the HOMO and LUMO levels of the charged and adjacent molecules.

Figure 2.6 (Bottom) shows optical images of some devices. As seen in **Figure 2.6** (Top), the light emitted from the corrugated device shows some diffraction due to the pattern.

In all cases, the EL peaked at 512 nm with a slightly increased shoulder at longer wavelengths for the device on glass/ITO.

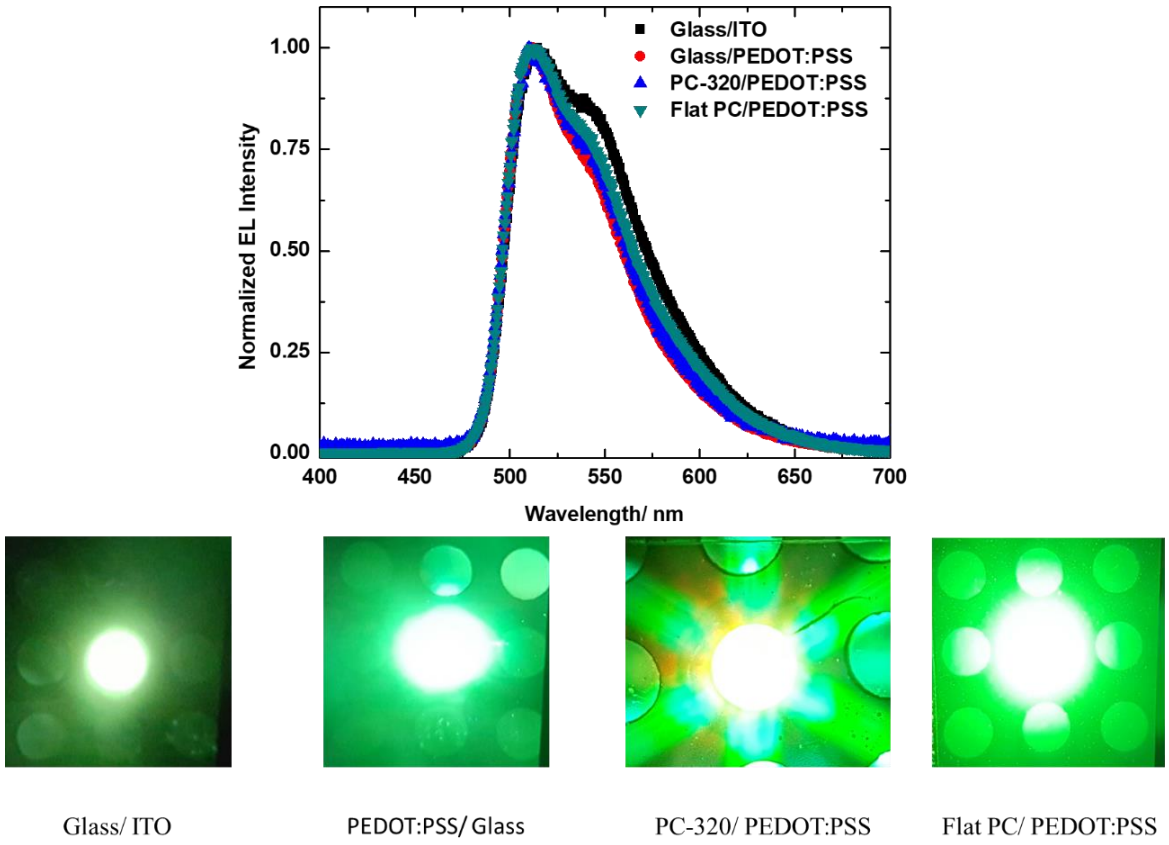

Figure 2.6: Top: Electroluminescence spectrum, Bottom: images of the working devices of green PhOLEDs on various substrates/ anode.

The luminous and power efficiencies (**Figure 2.7**) were the largest for the device fabricated on PC-320/ PEDOT:PSS. The maximal luminous efficiency for the latter was 164 cd A^{-1} at ≈200–300 cd m^{-2}, 1.9× the ≈ 87 cd A^{-1} of the PhOLED on glass/PEDOT:PSS, 2.4× the 67 cd A^{-1} of the device on glass/ ITO, and 2× the 82 cd A^{-1} of a device on flat PC. The respective maximal power efficiencies for the four substrate/anode combinations were 150, 80, 70, and 70 lm W^{-1}, i.e., the enhancements were 1.9× and 2.1×.

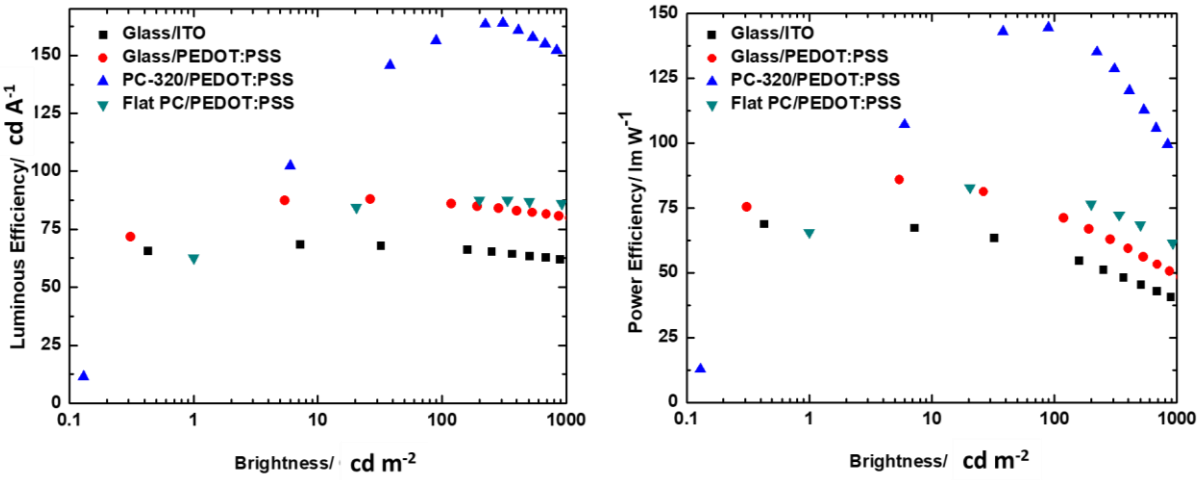

Figure 2.7: Left: Luminous efficiency, Right: Power efficiency of green PhOLEDs.

The maximal EQE was 50% with enhancements of 2× relative to the device on glass/PEDOT:PSS and 2.6× relative to that on glass/ITO (**Figure 2.8**). These enhancements are beyond those observed for the PhOLEDs with the thinner HTL and ETL. This is likely due to improved hole injection, masking of substrate nonuniformity and defect issues, and further enhanced outcoupling of photons otherwise lost to surface plasmon excitation.

All the optoelectronic properties are summarized in **Table 2.4**. As seen in **Table 2.4**, the highest EQE of 50% was obtained for a green PhOLED on PC-320, a 2× enhancement in comparison to such devices on glass and flat PC. This EQE entails $\eta_{out} \geq 50\%$ (Equation 3.1). Significant enhancements were also obtained for the blue PhOLEDs. This situation indicates that in addition to disrupting surface plasmon excitation, the enhancement is due to the extraction of photons trapped in the high index layers, as only small perturbations in the flat layer near the metal cathode are believed to be sufficient for reducing surface plasmon excitation.

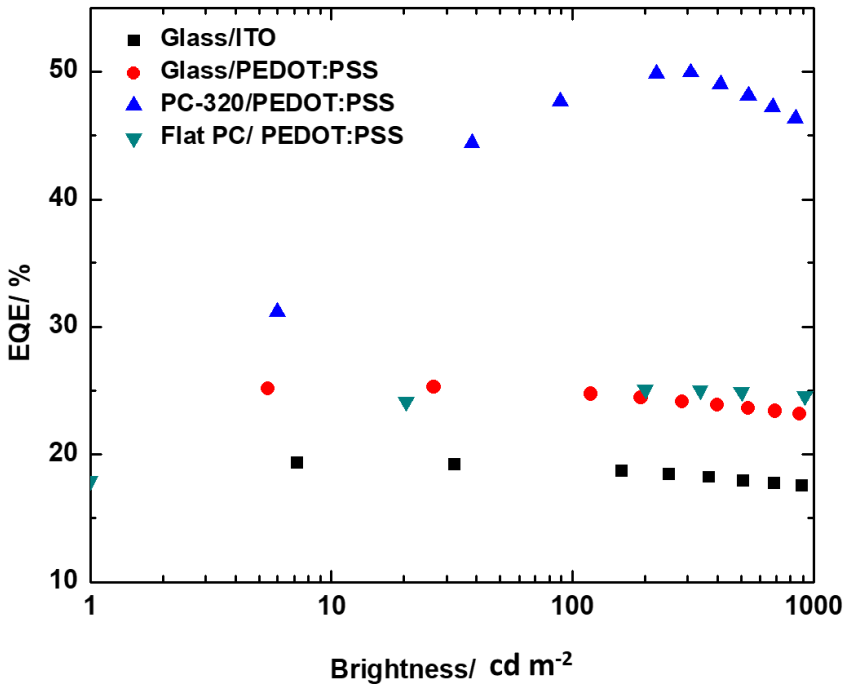

Figure 2.8: EQE of green PhOLEDs on various substrate/ anode.

Table 2.4: Green PhOLEDs' peak & 700 cdm^{-2} efficiencies and the enhancement factor of the PhOLEDs on the patterned substrate

Substrate/anode	**Luminous Efficiency (cdA^{-1})***	**Power efficiency (lmW^{-1})***	***EQE* (%)***	**Enhancement factors (relative to glass/ITO; glass/PEDOT:PSS; flat PC/PEDOT:PSS)**
Glass/ITO	68 (62)	67 (41)	19 (18)	
Glass/PEDOT:PSS	88 (82)	86 (53)	25 (23)	
Flat PC/ PEDOT:PSS	88 (86)	82 (64)	25 (25)	
Corrugated PC/ PEDOT:PSS	164 @ 300 cdm^{-2}; (154)	144 @ 100 cdm^{-2}; (104)	50 @ 300 cdm^{-2}; (47)	Luminous efficiency: 2.4x; 1.9x; 1.9x Power efficiency: 2.1x; 1.7x; 1.8x *EQE*: 2.6x; 2.0x; 2.0x

* The efficiencies at 700 cd m^{-2} are in parenthesis.

2.3.3.3. Blue PhOLEDs design 2: Single layer PEDOT:PSS anode and thicker HTL and ETL

We note that the conformal fabrication of blue PhOLEDs with Design 1, i.e., a relatively thick two-layer PEDOT:PSS anode was challenging, though high enhancement was achieved as summarized in **Table 2.5**. Hence, we present here only devices with Design 2. The device structure was that of the green PhOLED, except that the emitting layer was 20 nm of 8 wt.% FIrpic:mCP. We note that it is likely that the optimal thickness of the various device layers (that will enhance the efficiencies) in green and blue PhOLEDs differ; [12] a determination of such thicknesses requires a future detailed evaluation of various combinatorial arrays. The device spectrum and the current density- brightness-voltage (JLV) curve are shown in **Figure 2.9**.

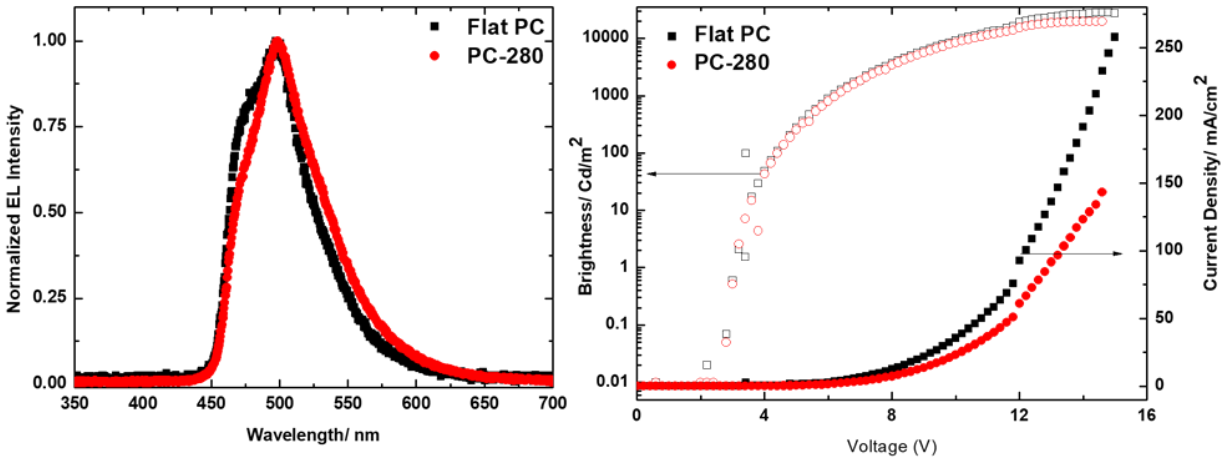

Figure 2.9: EL spectrum and the JLV curve of blue PhOLED.

Table 2.5: Comparison of attributes of green and blue PhOLEDs fabricated on different substrates with two layers of PEDOT:PSS (total thickness ~ 65 nm) as the anode.

	Sample	Turn on voltage (V)	Max. luminous efficiency (cdA^{-1})	Corresponding EL (cdm^{-2})	Luminous Efficiency @ 1000 cdm^{-2}
Green $Ir(ppy)_3$-based PhOLEDs	Flat PC	3.0	80	79	44
	PC-215	4.0	28	1321	27
	PC-250	3.0	89	247	47
	PC-280	3.0	118	323	64
	PC-320	3.0	127	118	57
	PC-500	3.4	54	127	29
Blue FIrpic-based PhOLEDs	Flat PC	3.3	29.2	110	9.6
	PC-320		87	140	17.9
	PC-135		45.2	408	30.9

The device attributes are shown in **Figure 2.10**. The maximal luminous efficiency (**Figure 2.10 (a)**) increased 2× from ≈ 31 to ≈ 62 cd A^{-1} at the patterned substrate. At ≈ 1000 cd m^{-2} the enhancement was ≈1.8×, increasing from 30 cd A^{-1} on the flat PC to ≈ 55 cd A^{-1} on the pattern. The maximal power efficiency (**Figure 2.10 (b)**) increased from 16.9 to ≈ 50 lm W^{-1}; a threefold enhancement; at ≈ 700 cd m^{-2} the enhancement was 1.7×; this reduction is due to a rapid roll-off for the unencapsulated corrugated device. Note that the roll off in the power efficiency is significantly steeper than in the luminous efficiency or EQE. This is direct proof that the resistance, probably that of the anode, is a major contributor to the power efficiency roll-off. The maximal EQE (**Figure 2.10 (c)**) increased to 25% from 15% for the flat device, a 1.7× enhancement. At ≈1000 cd m^{-2} the enhancement was 1.5-fold.

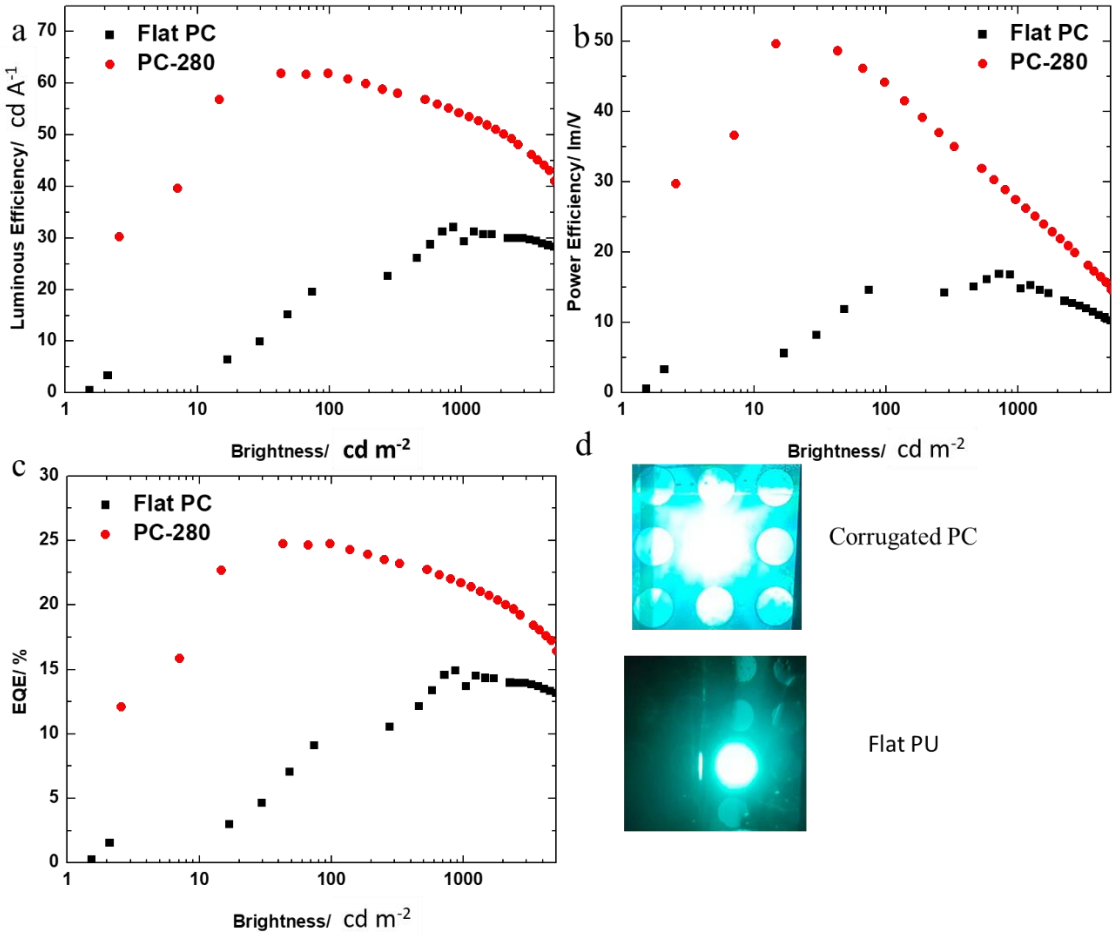

Figure 2.10: Device attributes of blue PhOLED. a) Luminous efficiency, b) Power efficiency, c) EQE and d) Images of the pixels.

2.3.3.4. Blue PhOLEDs design 2: Single layer PEDOT:PSS anode, thinner HTL, and thick ETL

As mentioned above, the thickness of the HTL and the ETL has a large influence on device performance. The optimal thickness of the HTL and the ETL not only depend on the respective materials but also on the emitting material as well. The blue PhOLED emission from the 20 nm 8 wt.% FIrpic doped in mCP, is more efficient when using a thinner 80 nm HTL and a thicker ETL (60 nm) rather than a thicker 140 nm HTL with the same 60nm ETL. The

improvement is apparent in both patterned and flat OLEDs. **Figure 2.11** shows the spectra and JLV curves of identical devices fabricated on PC-308 and on flat PC.

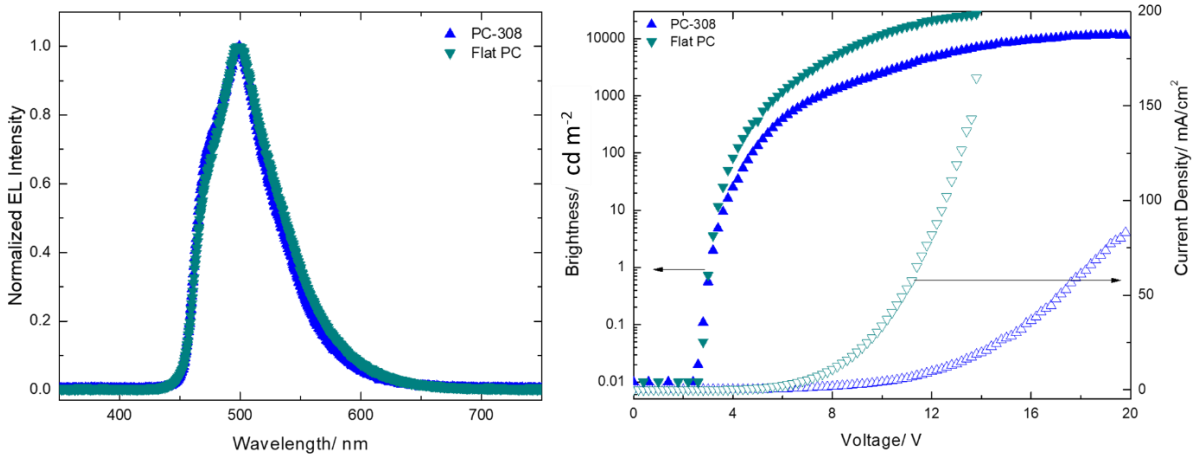

Figure 2.11: EL spectra and JLV behavior of blue PhOLED fabricated on flat and corrugated PC.

As the HTL thickness decreased from 140 nm to 80 nm, the luminous efficiency (**Figure 2.12a**) of the device on flat PC increased 1.8 fold from 31 to 57 cd A^{-1}. The luminous efficiency of the corresponding corrugated device increased 1.3 fold from 62 to 79 cd A^{-1}. The efficiency increase in the flat device is likely due to better charge balance for FIrpic-based blue OLEDs, that is weaker in the patterned device.

The Power efficiency (**Figure 2.12b**) of the flat device improved 2.4 fold from 17 to 41 lmW^{-1}. There was no enhancement in the power efficiency of the corrugated devices. **Figure 2.12c** shows the EQE of the blue PhOLEDs with 80 nm HTL on corrugated (32.4%) and flat (22.5%) PCs. The 1.3 fold enhancement is smaller than the 1.7 fold enhancement observed for the devices with 140 nm HTL.

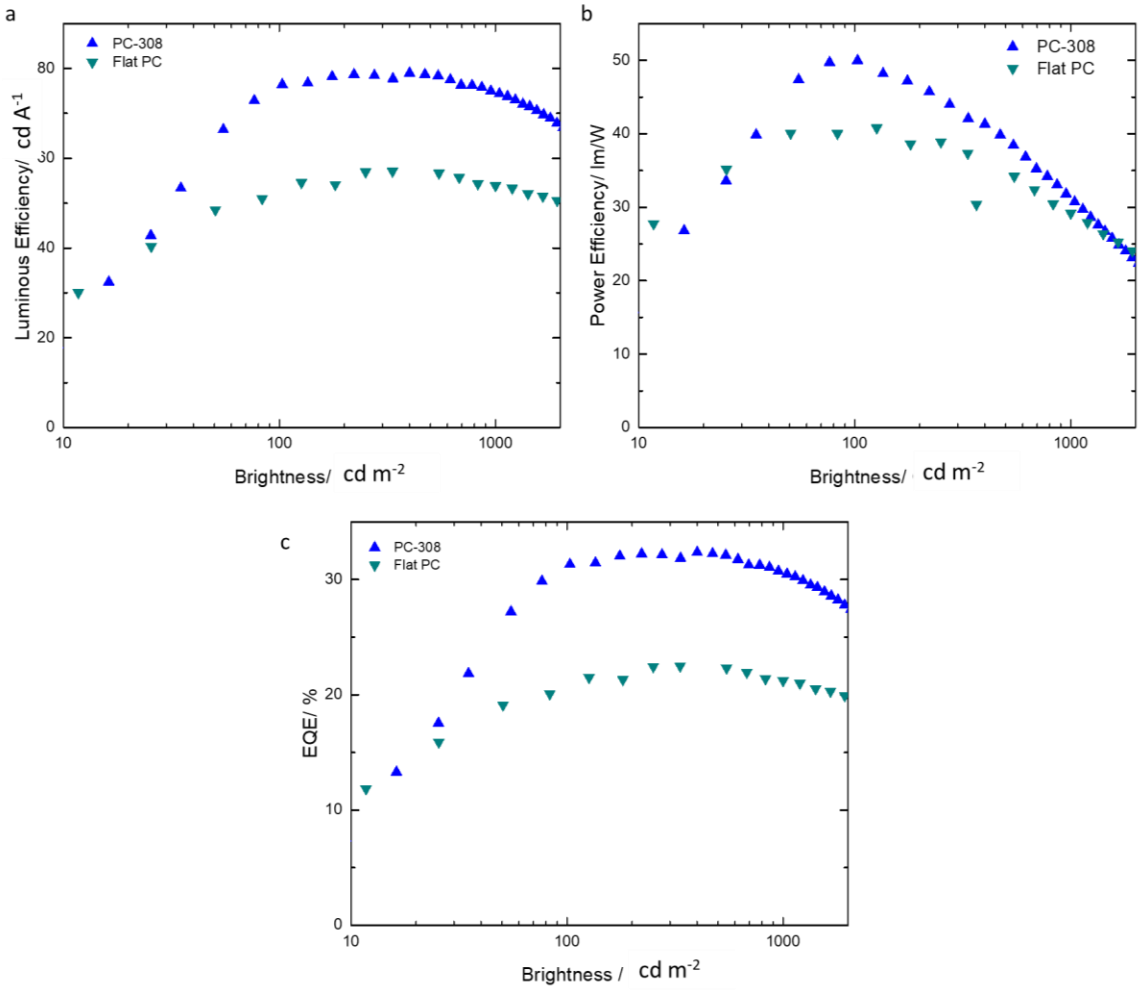

Figure 2.12: Performance of the blue PhOLED with 80 nm HTL and 60 nm ETL ,a) Luminous Efficiency, b) Power Efficiency, and EQE vs. Brightness.

2.3.3.5. White PhOLEDs design 2: Single layer PEDOT:PSS anode and 120 nm HTL and 60 nm ETL

The white PhOLED consist of only two emitters, blue and orange iridium(III) bis(4-phenylthieno[3,2-c]pyridinato-N,C20) acetylacetonate (PO-01). The device stack was similar to that of the green PhOLED that yielded an EQE of 50 %, with the emissive layer being 19 nm 8 wt.% FIrpic:mCP and 1 nm of 6 wt.% PO-01:mCP. Unlike the blue PhOLED that showed improved performance with a thinner HTL, the white PhOLED performed better with the

thicker HTL and ETL. The addition of 1 nm of 6 wt.% PO-01:mCP into the blue PhOLED, not only change the overall emission of the device but also change the energy levels within the device architecture, demanding a better charge balance at the emissive layer than the previously discussed blue device. As seen in **Figure 2.13** (left) the relative intensity of the blue emission is smaller than that of the orange emission in both the flat and the patterned devices, but the difference is less pronounced in the corrugated device. This observation requires further evaluation.

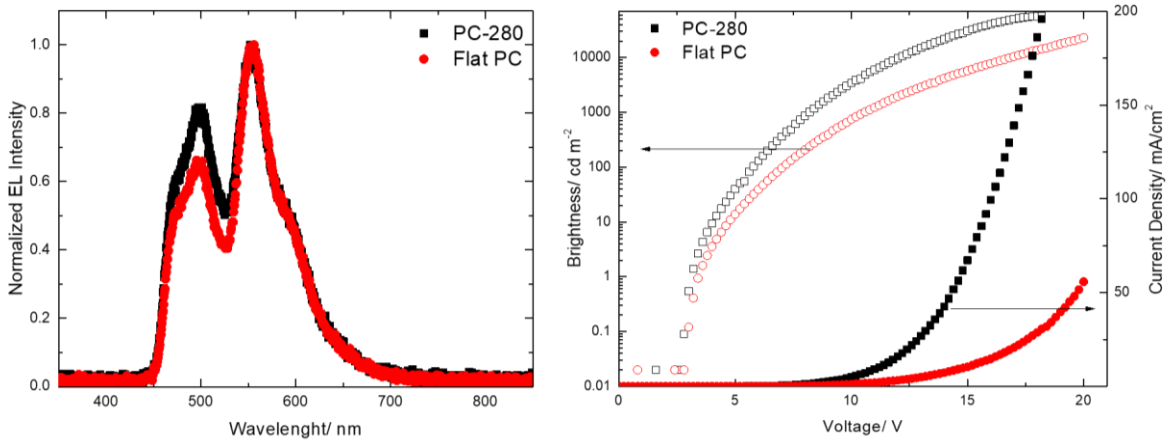

Figure 2.13: EL spectrum and the JLV curve for the white PhOLED fabricated on corrugated and flat PC.

The luminous efficiency and the EQE (**Figure 2.14**) of the white patterned PhOLED increased 1.3x relative to the flat device from 67.8 to 88.9 cd/A and from 23.6% to 31.8% respectively.

In summary, patterned green, blue and white PhOLEDs on PC/PEDOT:PSS show improved performance relative to devices on flat PC/PEDOT:PSS and more so in comparison to devices on glass/ITO.

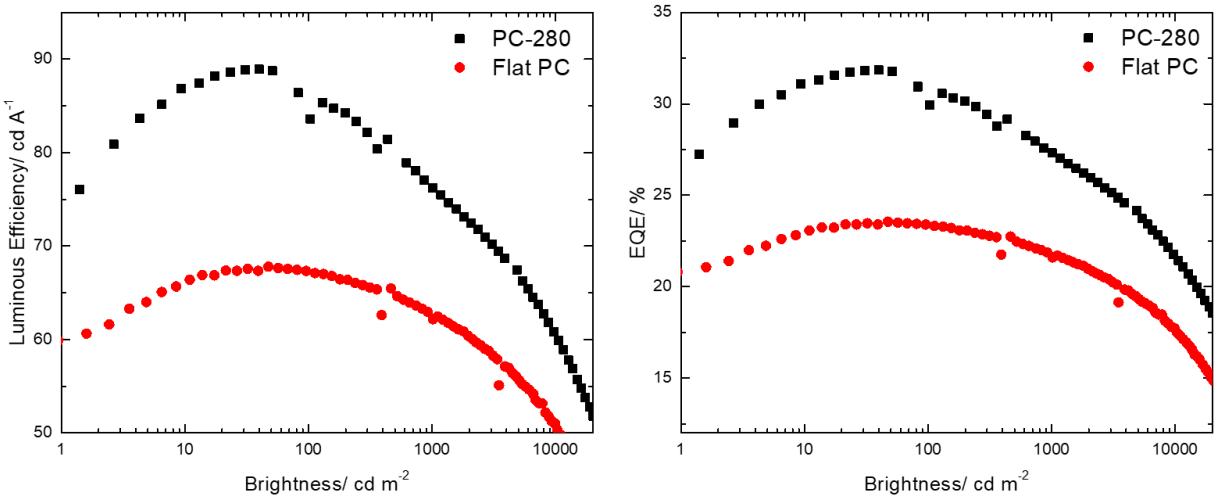

Figure 2.14: Luminous efficiency and the EQE of the white PhOLEDs.

2.3.4. Computational Modeling of the OLEDs

It is of great interest to predict the limits to outcoupling achievable in OLEDs using rigorous electromagnetic simulations to predict the optimum range of structures. Accordingly, we have employed two complementary computational approaches consisting of (i) Fourier space scattering matrix and (ii) real space finite difference time domain (FDTD) methods.

An alternative simulation approach to the scattering matrix that provides additional physical insights is the FDTD simulation employed the Lumerical package that has the ability to handle complex OLED corrugations, in a real space approach where the OLED is discretized in a real space grid (**Figure 2.15**). The emissive layer conforms to the contour of the corrugated substrate. The random orientation of the dipoles is modeled by a superposition of classical dipoles that are oriented in the three Cartesian directions (x, y, and z, with the z-direction perpendicular to the substrate). The dipoles can reside at varying distances from the PC/air interface. That is, the two extremum positions of the dipole correspond to (i) the 'highest' position farthest from the PC/air interface, where the dipoles form a ring-like distribution

above the corrugation peak, in contrast to (ii) the 'lowest' position, where the dipoles are located above the troughs of the anode corrugation, closest to the substrate/air interface. The distribution of emitted power was monitored (i) inside the OLED emissive layer (P_{in}) and (ii) in the air region outside the substrate (P_{out}), with the ratio P_{out}/P_{in} providing the outcoupling factor. Based on the FDTD simulations performed with corrugated OLEDs of the varying pitch a, we infer that 750 nm is optimal for blue OLEDs and benefits green OLEDs, whereas 500 nm is slightly better for red OLEDs. Thus, a single pitch around 750 nm may be a near-optimal choice for white OLEDs. The FDTD simulations indicated best enhancements were obtained for a range of pitch values ca 500-750 nm.

Accordingly, we simulated the enhancement of light for the two extremum positions of the dipoles as a function of the wavelength of the emission and averaging over the three dipole orientations. As an example, for a green OLED, an enhancement factor of ~1.6x was obtained for h = 200 nm and a = 500 nm for an OLED with 180 nm anode + HTL (90 nm each, glass/ITO OLED) and 70 nm ETL. The dipoles farther from the PC/air interface offer larger enhancement (~1.6x), than those residing closer to the substrate. Further exploration of dipole positions, pitch values, and corrugation heights are necessary to optimize the enhancements further. The effect on the maximal η_{out}, of changing h from 200 to 300 nm is small as indicated by the scattering matrix simulations.

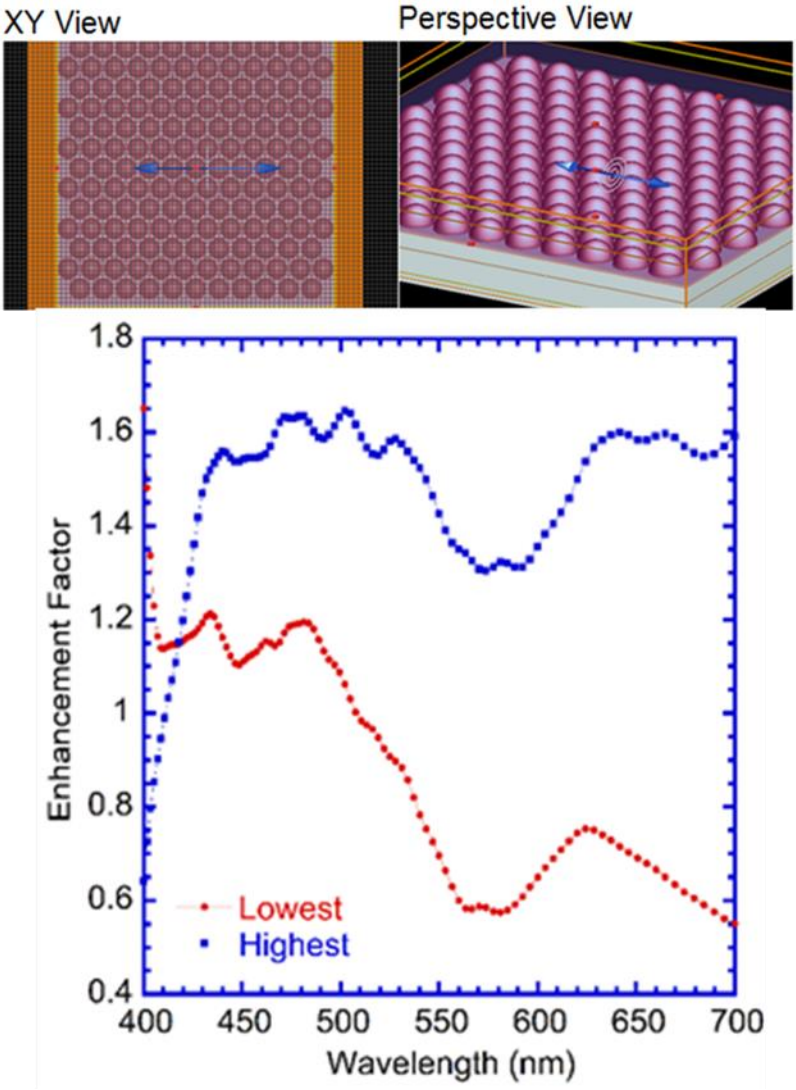

Figure 2.15: Corrugated OLED structures and emission enhancement factor vs. emission wavelength for two dipole locations, i.e., above the anode trough and above the corrugation peak.

2.3.4.3. Scattering matrix simulations in Fourier space

The rigorous scattering matrix approach in Fourier space provides a quantitative estimate of η_{out} and power losses within the OLED. Several studies [11,12,44,45] have developed this approach for flat OLEDs to quantify the waveguided modes within the substrate and high-index layers, in addition to the plasmonic losses.

The corrugated OLEDs we fabricated pose a problem of considerable complexity, and the theory of light emission from such systems has not previously been developed. Accordingly, we have developed a rigorous scattering matrix-based theory of light emission in corrugated systems (to be published), based on the formalism developed for flat OLEDs [11,12]. Our theory includes:

i. A corrugated OLED where each layer is described by periodic dielectric functions ε(r) and its Fourier components ε(G), where G is a vector of the reciprocal 2D periodic lattice.

ii. Dipoles in a conformally corrugated emissive layer forming annular rings at different heights z in the OLED. At each height, the dipoles are described by a Fourier transform H(G).

iii. Light emission from the dipoles in a conformally corrugated emissive layer that are reflected from the cathode and the air/substrate interface to generate a reflected electric field E (u, G) in the emissive layer. Here u is the parallel component of the wavevector in the emissive layer.

iv. The ability of the corrugated layers to scatter waveguided modes within the substrate and high index layer to the air through diffraction.

v. The Purcell factor of the emission rate, which is a lateral function of the planar coordinates x and y in each layer. This is converted into a Fourier transform of the convolution of the internal fields E (u, G), and the dipole positions H(G) and summed over all Fourier components G in the structure.

vi. Independently summing the emission from three polarizations of the dipoles (transverse magnetic vertical (TM_v), transverse magnetic horizontal (TM_h), and transverse electric horizontal (TE_h); i.e., z, x, y) to obtain the emission rates of dipoles in the corrugated layer $K(TM_v)$, $K(TM_h)$, and $K(TE_h)$.

vii. The emission of waves into the air region is simulated and modulated by the emission rates of dipoles in the corrugated layer for each of the three polarizations.

viii. A summation of emission from each independent parallel component u of the wave vector for the power emitted inside P_{in} and outside the structure P_{out}.

ix. The outcoupling factor η_{out}, which is the ratio of the power emitted into the air to the total emission P_{out}/P_{in} at each wavelength.

Maxwell's equations are solved in Fourier space for the substrate/ anode/HTL/ETL/Al cathode OLED with the emissive dipoles residing between the HTL and the ETL. By computing the reflected modes from the air/substrate interface and the ETL/metal cathode interface, we obtain the fields at the location of the dipole emitter and the Purcell factor, which represents inhibition or enhancement of the emission rates due to the OLED optical cavity geometry [11,12,44,45].

For a flat OLED with a PC or glass substrate, we simulated the outcoupling of light as a function of the ETL thickness, shown for a green OLED in **Figure 2.16**. There are two maxima in the outcoupled power, corresponding to ETL thicknesses of λ/4 (total optical thickness of 3λ/4), and a second peak at an ETL thickness of 3λ/4 (total optical thickness of 5λ/4), in agreement with previous reports [11,12]. Only <15% of the light is emitted to air within the first maximum.

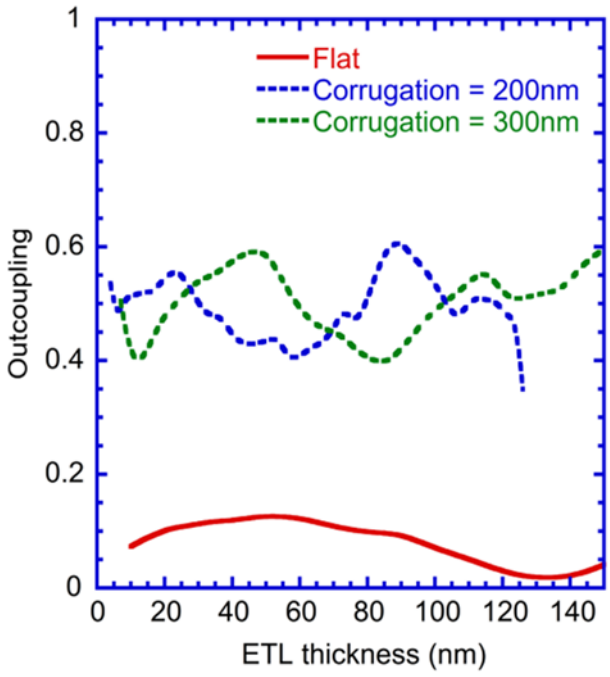

Figure 2.16: Simulated outcoupling from a green OLED (λ= 510 nm) on a patterned PC/PEDOT:PSS substrate/anode in comparison to a planar glass/ITO OLED using scattering matrix theory. The corrugation heights are 200 and 300 nm.

The outcoupling was computed as a function of the thickness of the ETL (d_{ETL}) layer. Initial results suggest a weak dependence on the ETL layer thickness. Numerically ill-converged regions around u ≈ 1.0 were truncated. We obtain η_{out} reaching 60% for both 200 and 300 nm corrugation heights, for a range of ETL thicknesses including an ETL layer thickness of ≈ 85 nm at 200 nm corrugation height. We utilized a PC substrate with n = 1.56 in the green OLED (λ = 510 nm) similar to the experiment. We utilized the annular ring with the largest density of dipole emitters located closest to the air–polycarbonate interface. The outcoupling dramatically exceeds that of a flat glass/ITO OLED where the outcoupling was <15%. Further studies will optimize the structure to maximize the outcoupling.

2.4. Summary and Concluding Remarks

We demonstrated outcoupling enhancements of 1.5- to ≈ 3-fold using various nano-corrugated PC substrates for green, blue, and white PhOLEDs with a PEDOT:PSS anode. The enhancements depend on the structure and height of the corrugation, and the PEDOT:PSS thickness has an effect on the device conformality and hence, performance. The largest enhancement was achieved for devices fabricated on convex patterns with a corrugation height h ≈280–400 nm and pitch of ≈750–800 nm. The observed enhancements are due to the effect of the corrugation on the extraction of the internally waveguided light in addition to reducing loss to surface plasmon excitation at the Al metal cathode.

The anode thickness was optimized to achieve a more conformal OLED stack and thus a more uniform current distribution. While an integrated substrate/anode with a metal mesh conductor, to reduce the resistance, and a thin ITO layer will further improve the devices; currently the best devices were achieved with a thin PEDOT:PSS (≈ 20–30 nm) anode. A thermally evaporated ITO can replace the PEDOT:PSS anode and conformal structures were observed using FIB, but ITO's high n ≈ 2 is problematic and fabricating a high-quality ITO film typically requires elevated temperatures, which is an issue with most plastic substrates. Surprisingly, despite the larger surface area, the layers' thicknesses on the corrugated substrates were similar to those on flat substrates.

Importantly, devices with doped thick HTL and ETL demonstrated improved performance. The thick HTL provided a cover to some of the substrates' defects that can otherwise lead to shorts. The thick ETL increased the distance between the cathode and the emissive layer, hence reducing plasmon excitation loss. Doping of the thicker layers was necessary for reducing the resistance of the devices. Device encapsulation, in particular, a

barrier layer integrated with the substrate/ anode to prevent moisture and O_2 from penetrating the relatively porous plastic, will lead to high efficiencies at high brightness and minimize quenching of the phosphorescence by O_2.

The simulations, reported for the first time for patterned devices, and experiment generally agree that large corrugation heights of ≈200–400 nm are necessary to achieve enhanced light outcoupling from OLEDs. The simulations also suggest that corrugations can reduce plasmonic losses that are particularly severe in thin flat OLEDs. The simulated outcoupling of $\eta_{out} \approx 60\%$ is consistent with the measured maximal EQE of 50% for green corrugated PhOLEDs on PC/PEDOT:PSS. Improving the conformality of the devices is ongoing, including utilizing predictive simulations to achieve a guiding maximal enhancement.

2.5. Experimental Section

2.5.1. Materials

The flat and patterned PC and PET/CAB substrates with various pattern heights and pitches were fabricated by MicroContinuum, Inc. The conductive polymer PEDOT:PSS, used as the anode, was purchased from H. C. Starck. LiF, BPhen, FIrpic, and the yellow emitter rubrene were purchased from Sigma-Aldrich. MoO_3 was purchased from Sterm Chemicals and NPB and Alq_3 from HW Sands Corporation. HAT-CN, TAPC, CBP, 3TPYMB, TmPyPB, and $Ir(ppy)_3$ were purchased from Luminescence Technology Corporation.

2.5.2. Corrugated PC and PET/ CAB fabrication

The patterned substrates were fabricated by proprietary processes developed by MicroContinuum Inc. (www.microcontinuum.com). The corrugated PC is fabricated by an efficient, direct near room-temperature molding process so that there is no patterned

layer/substrate interface, which eliminates peel off and index mismatch losses. The process eliminates thermal distortion and/ or degradation and reduces production time by avoiding slow heating/ cooling cycles required by conventional thermal molding processes. A single template with constant pitch was used to produce a wide range of amplitudes of the features' height without the cost/time required for fabricating new templates for each amplitude to be studied.

The corrugated PET/CAB substrates are generated by using the above process on a 12 μm thick layer of CAB previously slot coated onto a 75 μm thick PET carrier substrate. This approach enables independent optimization of the physical and optical characteristics of the patterned layer and the carrier substrate, including adjustment of the refractive index by modifying the patterned layer and the tear resistance of the carrier layer [46–48].

2.5.3. PEDOT:PSS Film Fabrication and Characterization

The PEDOT:PSS solution was mixed with 6 vol.% EG and 1 vol.% Capstone FS35 fluorosurfactant. The mixed solution was filtered using a 0.45 μm syringe filter. The solution was spun at various spin rates and spin durations. For example, a single layer of PEDOT:PSS was deposited by spin-coating the mixed solution at 6000 rpm for 30 s followed by annealing the film on a hot plate at 120 °C for 5 min. The second PEDOT:PSS layer was formed following the same procedure. The resulting film was annealed at 120 °C for 1 h in air and for 1 h in the glovebox. Sheet resistances were measured using a four-point probe setup with a source measurement unit (Keithley 200 and Fluke 8842A). The morphology of the films was obtained by AFM (TESPA) employing tapping mode; current distribution maps were imaged by conductive AFM employing contact mode.

2.5.4. FIB Imaging

For analysis of the OLED structure and stack conformality, an FEI Helios DualBeam FIB/SEM system was used that combines sputtering, imaging, and analytical capabilities. The system enables very precise ion milling in selected areas as well as high-resolution 3D microscopy. A beam of gallium ions is used for nm precision milling and imaging, depending on the ion energy and intensity; the Ga+ ion source can image and machine down to 5 nm resolution levels. The system also enables chemical analysis using X-ray energy dispersive spectroscopy (EDS).

2.5.5. OLED Fabrication and Characterization

OLEDs were fabricated on the PEDOT:PSS-coated corrugated and flat plastic substrates as well as on glass/ITO and glass/PEDOT:PSS substrates for reference. The Al cathode and all organic materials were deposited by thermal evaporation inside a chamber with a base pressure of $\approx 10^{-6}$ mbar within a glovebox. The Al cathode was deposited through a shadow mask containing either 1.5 mm diameter circular holes or 3 mm wide stripes. Characterization of the OLEDs was done using a Keithley 2400 source meter to apply a voltage and measure the current. The brightness was measured by a Minolta LS110 luminance meter, and the EL spectra were obtained using an Ocean Optics PC2000-ISA spectrometer. The raw spectra were obtained in the "SCOPE" mode but were corrected to the radiometrically calibrated mode; the spectra shown are the corrected spectra. LabView software was used to calculate the efficiencies from the experimental data.

2.6. Acknowledgment

The work was supported by the DOE/EERE under Grant Nos. DE-SC0011337 and DE-EE0007621. Ames Laboratory is operated by Iowa State University for the USDOE under

Contract No. DE-AC 02–07CH11358. The research was supported in part by Basic Energy Sciences, Division of Materials Science and Engineering, USDOE.

2.7. Reference

(1) Shinar, J.; Savvateev, V. In *Organic light emitting devices - A survey*; Shinar, J., Ed.; Springer, New York, 2004; pp 1–41.

(2) Kim, J.-S.; Ho, P. K. H.; Greenham, N. C.; Friend, R. H. Electroluminescence Emission Pattern of Organic Light-Emitting Diodes: Implications for Device Efficiency Calculations. *J. Appl. Phys.* **2000**, *88* (2), 1073.

(3) Chen, X.-W.; Choy, W. C. H.; Liang, C. J.; Wai, P. K. A.; He, S. Modifications of the Exciton Lifetime and Internal Quantum Efficiency for Organic Light-Emitting Devices with a Weak/Strong Microcavity. *Appl. Phys. Lett.* **2007**, *91*, 221112.

(4) Flämmich, M.; Danz, N.; Michaelis, D.; Wächter, C. A.; Bräuer, A. H.; Gather, M. C.; Meerholz, K. Measuring the Internal Luminescence Quantum Efficiency of OLED Emitter Materials in Electrical Operation. In *Proceedings of SPIE*; 2010; Vol. 7617, p 761715.

(5) Furno, M.; Rosenow, T. C.; Gather, M. C.; Lüssem, B.; Leo, K. Analysis of the External and Internal Quantum Efficiency of Multi-Emitter, White Organic Light Emitting Diodes. *Appl. Phys. Lett.* **2012**, *101*, 143304.

(6) Miwa, T.; Kubo, S.; Shizu, K.; Komino, T.; Adachi, C.; Kaji, H. Blue Organic Light-Emitting Diodes Realizing External Quantum Efficiency over 25% Using Thermally Activated Delayed Fluorescence Emitters. *Sci. Rep.* **2017**, *7*, 287.

(7) Baldo, M. A.; O'brien, D. F.; You, Y.; Shoustikov, A.; Sibley, S.; Thompson, M. E.; Forrest, S. R. Highly Efficient Phosphorescent Emission from Organic Electroluminescent Devices. *Nature* **1998**, *395*, 151–154.

(8) Baldo, M. A.; Lamansky, S.; Burrows, P. E.; Thompson, M. E.; Forrest, S. R. Very High-Efficiency Green Organic Light-Emitting Devices Based on Electrophosphorescence. *Appl. Phys. Lett.* **1999**, *75*, 4.

(9) Tsutsui, T.; Yang, M.; Yahiro, M.; Nakamura, K.; Watanabe, T.; Tsuji, T.; Fukuda, Y.; Wakimoto, T.; Miyaguchi, S. High Quantum Efficiency in Organic Light-Emitting Devices with Iridium-Complex as a Triplet Emissive Center. *Jpn. J. Appl. Phys.* **1999**, *38*, L1502.

(10) Madigan, C. F.; Lu, M.-H.; Sturm, J. C. Improvement of Output Coupling Efficiency of Organic Light-Emitting Diodes by Backside Substrate Modification. *Appl. Phys. Lett.* **2000**, *76* (13), 1650–1652.

(11) Meerheim, R.; Furno, M.; Hofmann, S.; Lüssem, B.; Leo, K. Quantification of Energy Loss Mechanisms in Organic Light-Emitting Diodes. *Appl. Phys. Lett.* **2010**, *97* (25), 1–4.

(12) Furno, M.; Meerheim, R.; Hofmann, S.; Lüssem, B.; Leo, K. Efficiency and Rate of Spontaneous Emission in Organic Electroluminescent Devices. *Phys. Rev. B - Condens. Matter Mater. Phys.* **2012**, *85* (11), 1–21.

(13) Park, J.-M.; Gan, Z.; Leung, W.; Lui, R.; Ye, Z.; Constant, K.; Shinar, J.; Shinar, R.; Ho, K.-M. Soft Holographic Interference Lithography Microlens for Enhanced Organic Light Emitting Diode Light Extraction. *Opt. Express* **2011**, *19* (S4), 786–792.

(14) Möller, S.; Forrest, S. R. Improved Light Out-Coupling in Organic Light Emitting Diodes Employing Ordered Microlens Arrays. *J. Appl. Phys.* **2002**, *91*, 3324.

(15) Chang, C.-H.; Chang, K.-Y.; Lo, Y.; Chang, T.-F.; Chang, H. More Light from Blue Organic LEDs Using Embedded Nanoparticles. *SPIE Newsroom* **2012**, No. Iii, 9–11.

(16) Gaertner, G.; Greiner, H. Light Extraction from OLEDs with (High) Index Matched Glass Substrates. In *Proceedings of SPIE*; 2008; p 6999.

(17) Koh, T.-W.; Spechler, J. A.; Lee, K. M.; Arnold, C. B.; Rand, B. P. Enhanced Outcoupling in Organic Light-Emitting Diodes via a High-Index Contrast Scattering Layer. *ACS Photonics* **2015**, *2*, 1366–1372.

(18) Spechler, J. A.; Koh, T. W.; Herb, J. T.; Rand, B. P.; Arnold, C. B. A Transparent, Smooth, Thermally Robust, Conductive Polyimide for Flexible Electronics. *Adv. Funct. Mater.* **2015**, *25* (48), 7428–7434.

(19) Sun, Y.; Forrest, S. R. Enhanced Light Out-Coupling of Organic Light-Emitting Devices Using Embedded Low-Index Grids. *Nat. Photonics* **2008**, *2*, 483–487.

(20) Qu, Y.; Slootsky, M.; Forrest, S. R. Enhanced Light Extraction from Organic Light-Emitting Devices Using a Sub-Anode Grid. *Nat. Photonics* **2015**, *9*, 758–763.

(21) Zhou, L.; Xiang, H.-Y.; Shen, S.; Li, Y.-Q.; Chen, J.-D.; Xie, H.-J.; Goldthorpe, I. A.; Chen, L.-S.; Lee, S.-T.; Tang, J.-X. High-Performance Flexible Organic Light-Emitting Diodes Using Embedded Silver Network Transparent Electrodes. *ACS Nano* **2014**, *8* (12), 12796–12805.

(22) Wang, R.; Xu, L. H.; Li, Y. Q.; Zhou, L.; Li, C.; Ou, Q. D.; Chen, J. De; Shen, S.; Tang, J. X. Broadband Light Out-Coupling Enhancement of Flexible Organic Light-Emitting Diodes Using Biomimetic Quasirandom Nanostructures. *Adv. Opt. Mater.* **2015**, *3* (2), 203–210.

(23) Xiang, H.-Y.; Li, Y.-Q.; Zhou, L.; Xie, H.-J.; Li, C.; Ou, Q.-D.; Chen, L.-S.; Lee, C.-S.; Lee, S.-T.; Tang, J.-X. Outcoupling-Enhanced Flexible Organic Light-Emitting Diodes on Ameliorated Plastic Substrate with Built-in IndiumÀTin-Oxide-Free Transparent Electrode. *ACS Nano* **2015**, *9* (7), 7553–7562.

(24) Xu, L.-H.; Ou, Q.-D.; Li, Y.-Q.; Zhang, Y.-B.; Zhao, X.-D.; Xiang, H.-Y.; Chen, J.-D.; Zhou, L.; Lee, S.-T.; Tang, J.-X. Microcavity-Free Broadband Light Outcoupling Enhancement in Flexible Organic Light-Emitting Diodes with Nanostructured Transparent Metal−Dielectric Composite Electrodes. *ACS Nano* **2016**, *10*, 1625–1632.

(25) Chen, C.-Y.; Chen, Y.-J.; Lee, W.-K.; Lu, C.-Y.; Lin, H. Y.; Wu, C.-C. Analyses of Optical Out-Coupling of Organic Light emitting Devices Having Micromesh Indium Tin Oxide and Conducting Polymer as Composite Transparent Electrode. *Opt. Express* **2016**, *24* (10), A810–A822.

(26) Koo, W. H.; Jeong, S. M.; Nishimura, S.; Araoka, F.; Ishikawa, K.; Toyooka, T.; Takezoe, H. Polarization Conversion in Surface-Plasmon-Coupled Emission from Organic Light-Emitting Diodes Using Spontaneously Formed Buckles. *Adv. Mater.* **2011**, *23* (8), 1003–1007.

(27) Nüesch, F.; Forsythe, E. W.; Le, Q. T.; Gao, Y.; Rothberg, L. J. Importance of Indium Tin Oxide Surface Acido Basicity for Charge Injection into Organic Materials Based Light Emitting Diodes. *J. Appl. Phys.* **2000**, *87* (11), 7973–7980.

(28) Cai, M.; Ye, Z.; Xiao, T.; Liu, R.; Chen, Y.; Mayer, R. W.; Biswas, R.; Ho, K. M.; Shinar, R.; Shinar, J. Extremely Efficient Indium-Tin-Oxide-Free Green Phosphorescent Organic Light-Emitting Diodes. *Adv. Mater.* **2012**, *24* (31), 4337–4342.

(29) Gasiorowski, J.; Menon, Reghu; Hingerl, K.; Dachev, M.; Sariciftci, N. S. Surface Morphology, Optical Properties and Conductivity Changes of Poly(3,4-Ethylenedioxythiophene):Poly(Styrenesulfonate) by Using Additives. *Thin Film Solids* **2013**, *536*, 211–215.

(30) Cai, M.; Xiao, T.; Hellerich, E.; Chen, Y.; Shinar, R.; Shinar, J. High-Efficiency Solution-Processed Small Molecule Electrophosphorescent Organic Light-Emitting Diodes. *Adv. Mater.* **2011**, *23* (31), 3590–3596.

(31) Xiao, T.; Cui, W.; Anderegg, J.; Shinar, J.; Shinar, R. Simple Routes for Improving Polythiophene:Fullerene-Based Organic Solar Cells. *Org. Electron.* **2011**, *12* (2), 257–262.

(32) Ouyang, J.; Xu, Q. F.; Chu, C. W.; Yang, Y.; Li, G.; Shinar, J. On the Mechanism of Conductivity Enhancement in Poly(3,4-Ethylenedioxythiophene):Poly(Styrene Sulfonate) Film through Solvent Treatment. *Polymer (Guildf).* **2004**, *45* (25), 8443–8450.

(33) Kim, Y. H.; Sachse, C.; MacHala, M. L.; May, C.; Müller-Meskamp, L.; Leo, K. Highly Conductive PEDOT:PSS Electrode with Optimized Solvent and Thermal Post-Treatment for ITO-Free Organic Solar Cells. *Adv. Funct. Mater.* **2011**, *21* (6), 1076–1081.

(34) Cai, M.; Xiao, T.; Liu, R.; Chen, Y.; Shinar, R.; Shinar, J. On the Mechanism of Conductivity Enhancement in Poly(3,4-Ethylenedioxythiophene):Poly(Styrene Sulfonate) Film through Solvent Treatment. *Appl. Phys. Lett* **2011**, *99*, 153303.

(35) Fehse, K.; Walzer, K.; Leo, K.; Lövenich, W.; Elschner, A. Highly Conductive Polymer Anodes as Replacements for Inorganic Materials in High-Efficiency Organic Light-Emitting Diodes. *Adv. Mater.* **2007**, *19* (3), 441–444.

(36) Na, S.-I.; Kim, S.-S.; Jo, J.; Kim, D.-Y. Efficient and Flexible ITO-Free Organic Solar Cells Using Highly Conductive Polymer Anodes. *Adv. Mater.* **2008**, *20* (21), 4061–4067.

(37) Hecht, D. S.; Hu, L.; Irvin, G. Impact of the Expression of P Glycoprotein, the Multidrug Resistance-Related Protein, Bcl-2, Mutant P53, and Heat Shock Protein 27 on Response to Induction Therapy and Long-Term Survival in Patients with de Novo Acute Myeloid Leukemia. *Adv. Mater.* **2011**, *23* (13), 1482–1513.

(38) Hrehorova, E.; Rebros, M.; Pekarovicova, A.; Fleming, P. D.; Bliznyuk, V. N. Characterization of Conductive Polymer Inks Based on PEDOT:PSS. *TAGA J.* **2008**, *4*, 219–231.

(39) Vosgueritchian, M.; Lipomi, D. J.; Bao, Z. Highly Conductive and Transparent PEDOT:PSS Films with a Fluorosurfactant for Stretchable and Flexible Transparent Electrodes. *Adv. Funct. Mater.* **2012**, *22* (2), 421–428.

(40) Palumbiny, C. M.; Schlipf, J.; Hexemer, A.; Wang, C.; Müller-Buschbaum, P. The Morphological Power of Soap: How Surfactants Lower the Sheet Resistance of PEDOT:PSS by Strong Impact on Inner Film Structure and Molecular Interface Orientation. *Adv. Electron. Mater.* **2016**, *2* (4), 1500377.

(41) Shinar, J.; Shinar, R. Organic Light-Emitting Devices (OLEDs) and OLED-Based Chemical and Biological Sensors: An Overview. *J. Phys. D. Appl. Phys.* **2008**, *41* (13), 133001.

(42) Han, J.; Kwon, Y.; Sohn, J.; Lee, C. Highly Enhanced Phosphorescent Organic Light-Emitting Diodes with Cesium Fluoride Doped Electron Injection Layer. *Proc. SPIE* **2015**, *9566*, 95662E.

(43) Dai, Y.; Zhang, H.; Zhang, Z.; Liu, Y.; Chen, J.; Ma, D. Highly Efficient and Stable Tandem Organic Light-Emitting Devices Based on HAT-CN/HAT-CN: TAPC/TAPC as a Charge Generation Layer. *J. Mater. Chem. C* **2015**, *3*, 6809–6814.

(44) Sullivan, K. G.; Hall, D. G. Enhancement and Inhibition of Electromagnetic Radiation in Plane-Layered Media. I. Plane-Wave Spectrum Approach to Modeling Classical Effects. *J. Opt. Soc. Am. B* **1997**, *14* (5), 1149–1159.

(45) Neyts, K. A. Simulation of Light Emission from Thin-Film Microcavities. *J. Opt. Soc. Am. A* **1998**, *15* (4), 962–971.

(46) Slafer, W. D.; Kime, M. B.; Monen, M. J.; Horton, W. G.; Robinson, W. C.; Wan, L. C. Continuous Manufacturing of Thin Cover Sheet Optical Media. *Proc. SPIE* **1992**, *1663*, 324–335.

(47) Cowan, J. J.; Slafer, W. D. Recording And Replication Of Holographic Micropatterns For The Ordering Of Photographic Emulsion Grain In Film Systems . *J. Imaging Sci.* **1987**, *31* (3), 100–107.

(48) Cowan, J. J.; Slafer, W. D. Holographic Embossing at Polaroid: The Polaform Process. *Proc. SPIE* **1986**, *600* (June 1986), 49–56.

CHAPTER 3. ENHANCED EFFICIENCY THROUGH REDUCED SURFACE PLASMONS LOSS

3.1. Abstract

The efficiency of OLEDs is limited by various loss mechanisms. Photon loss due to surface plasmons is a major loss channel, and along with waveguiding, it is responsible for the loss of 50-53% of the photons generated in the emission zone. In this work, we tried to minimize the surface plasmon loss by two methods: first, by increasing the distance between the emissive layer and the metal cathode and second by using a corrugated device structure. By increasing the organic layer thickness between the emissive layer and the metal cathode, the external quantum efficiency was increased from 10% to 21% The change in the optical cavity length also had a significant effect on the emission spectra. Substrates with shallow corrugation were used to disrupt the surface plasmons and yielded an EQE enhancement factor of 1.9, realizing an EQE of 40% for the corrugated device.

3.2. Introduction

Thin film OLEDs are in high demand in commercial displays and emerging in lighting products due to their ability to produce soothing colors, high contrast images, and the applicability in wearable technology. Their stability, lifetime, and efficiency have improved dramatically over the last three decades after the first thi~~n~~ film OLEDs were reported by Tang and Van Slyke [1] in 1987. Though the first commercial applications of OLEDs were in display technology, their development has led to their emergence in general lighting fixtures as well as in various biological sensors such as oxygen, immunoassays, glucose, and hydrocarbon sensors [2]. Over the years, the primary focus has been to improve the yield of charge-to-photon conversion known as IQE of OLEDs. Development of devices such as phosphorescent OLEDs

and TADF OLEDs enabled harvesting triplets and consequently improving the IQE to nearly 100% [3,4].

Lately, the focus has shifted toward improving the outcoupling efficiency η_{out} since most of the generated photons get trapped or are lost inside the OLED stack due to the mechanisms mentioned above. The generated excitons decay either radiatively or non-radiatively. When the in-plane wavevector of the emitting dipole $k_{\parallel}$ is less than the free space wavevector $k_0 = 2\pi/\lambda_0$, with λ_0 the free space emission wavelength, then the energy may leak from the mode and produce useful far-field emission, known as leaky mode radiative decay. But when $k_{\parallel} > k_0$, it contains too much momentum to be coupled to a free space mode and consequently it gets trapped as a waveguiding mode [5].

Light loss due to waveguiding through the organic+ITO stack or through the substrate also contributes significantly to the total light loss in OLEDs. To outcouple the light that undergoes total internal reflection at the substrate/air interface, external extraction techniques have been developed. An external microlens array (μLA) fabricated on the blank, i.e., external, side of the glass/ITO/OLED stack using soft lithography imprinting yielded up to a 100% increase in the EL for both green and blue fluorescent OLEDs [6]. The periodic surface variation at the μLA interface provides variation in incident angle for the light, and the light that gets reflected into the device will reflect again from the reflective cathode and eventually exit into the forward hemisphere. Another promising approach to enhance light extraction is the use of a corrugated surface to fabricate the OLEDs on. The corrugation of the surface is carried out throughout the organic stack and into the reflective cathode. Such device architecture provides the light generated from the emissive layer to scatter randomly at various interfaces to minimize the waveguiding and the substrate loss. The latter technique was used to demonstrate

a 2-fold EQE enhancement for green PhOLEDs fabricated on patterned PC substrates with a pitch of ~750 nm and a feature height of 300-400 nm [7].

Excitons can also decay nonradiatively, which results in heating the surrounding material if the decay is by phonon emission.

The surface charge density oscillations at the metal/dielectric interface are known as surface plasmons. They consist of damped, transverse-magnetic (TM), nonradiative, electromagnetic surface waves that propagate along and confined to the interface [8]. When the metal cathode is in the proximity ($\leq \lambda_0/30$) [5] of the emitter molecule, the photon energy is dissipated as a surface plasmon. Photon loss due to surface plasmons is often neglected, but along with waveguiding modes, the loss can be as high as 50-53% [9]. Diminishing these loss paths is the key to achieve highly efficient OLEDs and reaching the US Department of Energy (USDOE) outcoupling milestone of 70% by the year 2020.

The OLED community has put considerable effort to quantify and minimize the surface plasmon loss. Since interaction between the oscillating dipole and the metal cathode is short-range, a thicker organic layer between the cathode and the EML is a viable option. The ETL, which is in between the cathode and EML, can be used to increase the separation between the two. But increasing the ETL thickness is at the expense of other device performance metrics (e.g., the power efficiency) since a thicker layer increases the ohmic resistance. Appropriate *n*-doping of the ETL reduces the resistance. In such cases, the *n*-dopant must be carefully selected to minimize any electrical losses, and the efficiency of the doping highly depends on the dopant as well as the host material. Formation of an ion pair or a charge carrier complex upon doping is essential for it to be effective. This has been proven experimentally in systems such as BPhen

and Alq_3 [10]. Here we demonstrate the effect of the host material with cesium fluoride (CsF) as the dopant.

Another technique used to minimize the surface plasmon loss is called surface plasmon cross coupling (SPCC). Surface plasmons carry a larger momentum (wavevector) than a photon propagating in free space, and therefore it requires assistance to radiate into free space. Having an opaque metal layer with periodic structure act as a Bragg diffraction grating that can couple surface plasmons back to free space allows light to radiate from surface plasmon modes [11]. SPCC is a three-step process where the emitting dipole near the metal cathode excites a surface plasmon in the dielectric medium at the metal/ dielectric interface, and then periodic metal cathode allows the excited surface plasmon to cross couple to the metal medium at the interface. Finally, the grating allows the excited surface plasmon to emit into free space [8,12,13].

In this work, we concentrate our focus to minimize the photon loss due to surface plasmons via two approaches. First is by increasing the separation between the metal cathode and the emitting dipole using a thick ETL, where we observed a 2X enhancement in EQE relative to the optimized white PhOLED with a thinner ETL. Second is by using various shallow corrugation patterns that further improve the device performance by coupling the surface plasmons into far-field emission. The results were expressed using a green PhOLED and compared to an identical device fabricated on a flat substrate to validate the difference.

3.3. Results and Discussion

3.3.1. White PhOLED With Varying ETL Thickness

A white PhOLED based on blue and orange emitters was investigated *vs.* ETL thickness to optimize the plasmon loss mitigation. The device structure was modified from the

structure described in Zhou *et al*. where FIrpic is the (sky) blue emitter, and PO-01 is the orange emitter, producing near-white emission. The reference device on glass/ITO yields an EQE of 9.1% [14] and is the reference device for the following comparison.

The reference white PhOLEDs were fabricated on glass/ITO substrates with 5 nm of MoO_3 as the hole injecting material. Because of its high triplet energy, 1,3-Bis(carbazol-9-yl)benzene (mCP) was selected as the host material for both FIrpic and PO-01. This consequently requires a hole transport material with a deep HOMO energy level E_{HOMO}, the requirement satisfied by 40 nm TAPC. A 30 nm neat TPBi layer served as the ETL. Another TPBi layer doped with 2 wt.% CsF was added to increase the separation between the cathode and the emissive layer. The thickness x of the doped ETL layer was varied from 0 to 150 nm with the device with x = 0 nm being identical to the original device described in Zhou *et al*. [14]. **Figure 3.1** shows the brightness and current density *vs.* voltage of the devices. As seen, the turn-on voltage (i.e., the voltage at 1 cd/m^2 brightness) increased with the doped ETL thickness indicating the high voltage required to operate the device. It can also be seen clearly in the current *vs.* voltage plot, indicating inefficient doping of TPBi with 2 wt.% CsF.

Figure 3.1 indicates that the ETL needs to be doped effectively, so the OLED resistance will not increase significantly with ETL thickness. To that end, TPBi was replaced by TmPyPb, and the CsF doping concentration was increased from 2 wt.% to 20 wt.%. However, increasing the electron path to the EML can result in hole accumulation in the EML, which would increase the quenching of the emission by these holes. Therefore, the HTL thickness would also be needed to increase, but not necessarily by the same amount, since the electron and hole mobilities differ. With the new ETL, the HTL was changed to a 10 wt.%

MoO_3-doped TAPC of varying thickness and a 20 nm neat TAPC layer to keep positive charges away from the EML. Hence the full device structure was

ITO/ MoO_3 (20 nm)/ 10 wt.% MoO_3:TAPC (*x*)/ TAPC (10 nm)/ 8 wt.% FIrpic:mCP (20 nm)/ TmPyPb (30 nm)/ 20 wt.% CsF: TmPyPb (*y*)/ LiF (1 nm)/ Al (100 nm)

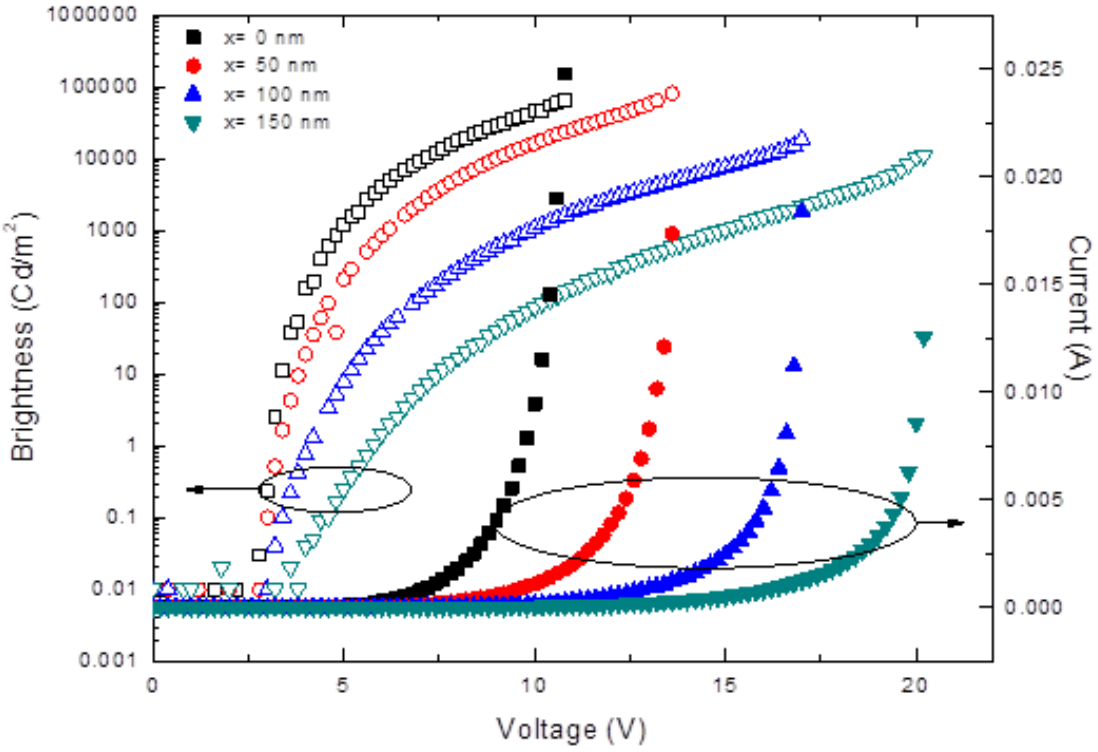

Figure 3.1: Brightness-current vs. voltage characteristic of the white PhOLEDs with varying ETL thickness.

A 2-dimensional (2-d) combinatorial array of OLED pixels was fabricated on ITO-coated flat PET by varying the doped ETL and HTL, in two orthogonal directions, during fabrication. The doped HTL thickness *x* was 10, 50, 75, 100, 125, 150, 175, and 200 nm and the doped ETL thickness *y* was 10, 20, 40, 50, 60, 80, and 100 nm. **Figure 3.2** represents the EQE plotted against the total HTL thickness, i.e., the combined thickness of the doped HTL

and the neat HTL and the total ETL thickness, i.e., the combined thickness of the doped ETL and the neat ETL.

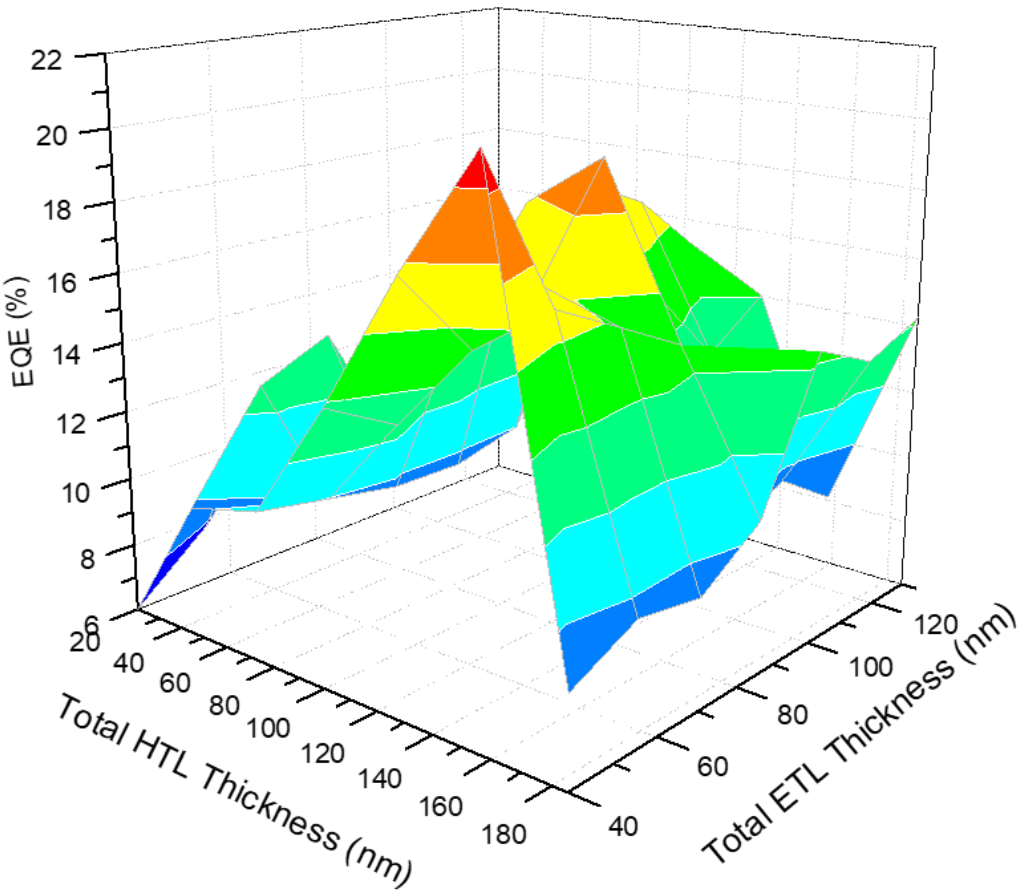

Figure 3.2: The EQE of the 2-dimensional combinatorial array of OLED pixels plotted against the total HTL thickness and the total ETL thickness.

As shown in **Figure 3.2** and **Figure 3.3** the EQE of the devices varied according to the ETL and HTL thickness, and the highest value of 21% was obtained when the total HTL and ETL thicknesses were 160 and 40 nm, respectively; the EQE of the reference device was 9.1% [14] demonstrating an enhancement factor of 2.3. This enhancement is clearly due to minimizing the photon loss to surface plasmons by increasing the distance between the EML and the Al cathode. The variation in both *x* and *y* enabled identification of the optimal pair of values that

yielded optimal charge balance and minimal charge accumulation, and consequently the maximal EQE of 21%.

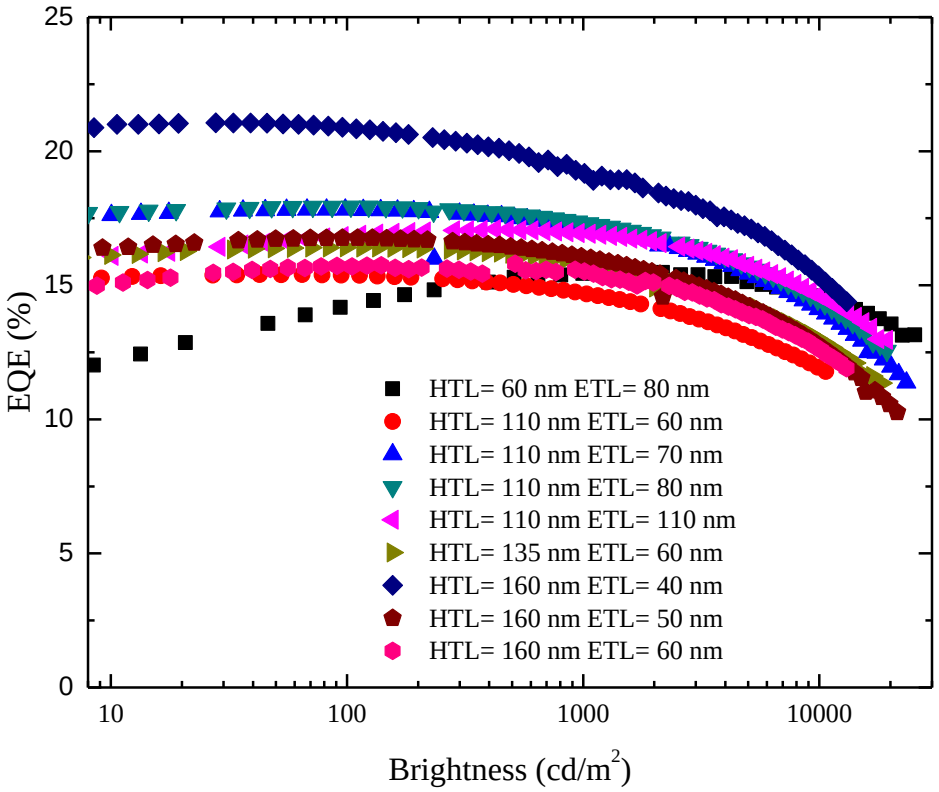

Figure 3.3: The EQE of the best devices of the 2-d combinatorial array.

One of the features of the 2-d array is the variation of the EL spectra, which is due to the variation in the thickness of the devices and the weak microcavity effect. Despite the fact that the EML contains two emitting molecules, blue emitting FIrpic and orange emitting PO-01, the devices displayed distinct emission peaks due to the microcavity effect, shown in **Figure 3.4**. The device with the best attributes, where the total HTL and ETL were 160 nm and 40 nm, respectively, showed a peak emission at 500 nm suppressing most of the orange emission generated by PO-01.

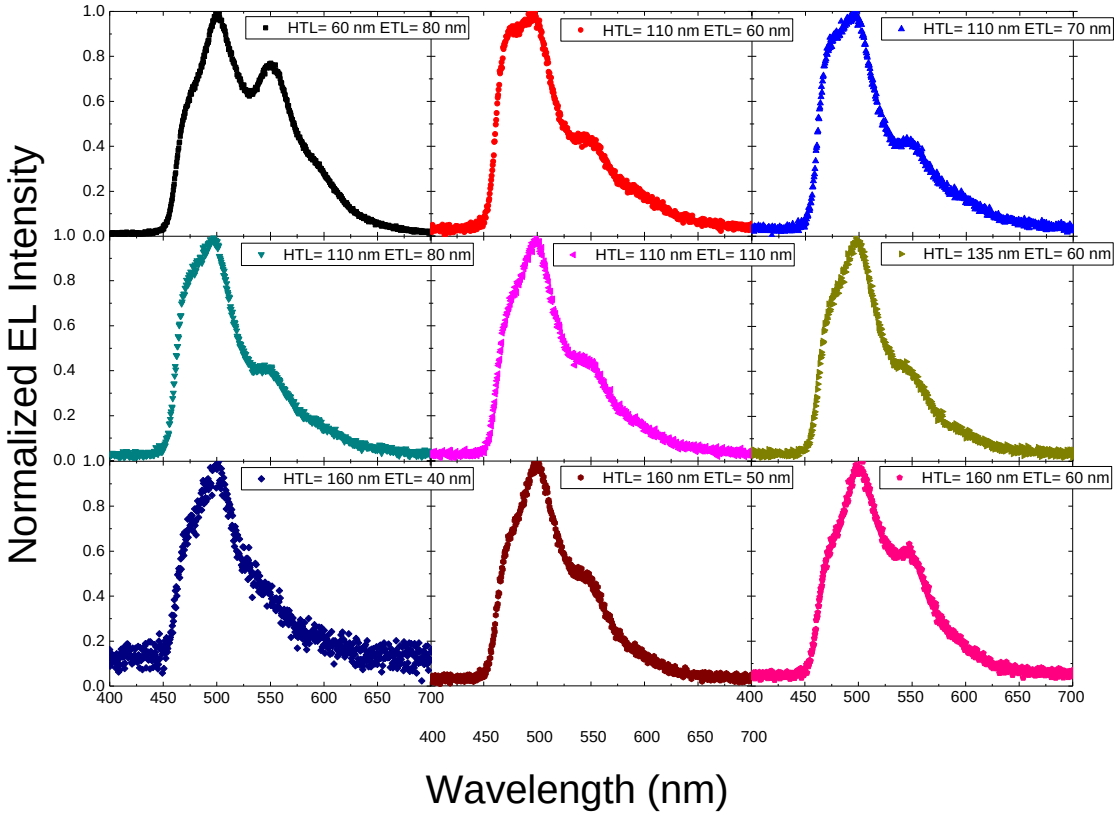

Figure 3.4: The EL spectra for the devices with the best attributes in the 2-d combinatorial array.

3.3.2. Green PhOLEDs on Substrates with Shallow Corrugation

Next, the possibility to reduce the surface plasmon loss using corrugation was investigated. As described and demonstrated in Chapter 2, corrugated surfaces can lead to very high efficiencies. OLEDs made on a corrugated surface with a pitch of 750 nm and a feature height of 300-400 nm were shown to enhance EQE by a factor of 2 with respect to devices made on a flat substrate. In such high corrugation heights, the loss modes, i.e., substrate, waveguiding and surface plasmon modes are disrupted by the corrugation and most of the generated light is scattered into the forward hemisphere as far-field emission.

To identify the specific effect of the corrugation on the surface plasmons, the corrugation height was small so that waveguiding, and substrate modes were still considerable. Two types of corrugations were investigated. The first featured a moth-eye structure (**Figure 3.5**), where the feature height to be ~80 nm and the pitch was ~275 nm measured using an Atomic Force Microscope (AFM) performed by Rajiv Kaudal. A green PhOLED featuring 6 wt.% $Ir(ppy)_3$ was fabricated on moth-eye surface with a thin 35 nm TmPyPb ETL where the surface plasmons can still be excited on the Al cathode by the dipoles in close by emissive layer. To find the best HTL thickness (that yields the best charge balance) the TAPC HTL was doped with 10 wt.% MoO_3 and its thickness *x* was 25, 30, 35, and 40 nm. Since the surface plasmons are generated at the organic/metal interface, it is important to maintain the corrugation throughout the device stack up to the Al cathode. The full device stack was as follows:

Substrate/ 1 layer PEDOT:PSS/ HAT-CN (5 nm)/ 10 wt.% MoO_3: TAPC (*x*)/ TAPC (20 nm)/ 6 wt.% $Ir(ppy)_3$: mCP (20 nm)/ TmPyPb (35 nm)/ LiF (1 nm)/ Al (100 nm).

The thickness x =35 nm proved to be the best (**Figure 3.6a**). As seen from **Figure 3.6b**, the device on the moth-eye corrugation yielded an EQE of 37% compared to an identical device fabricated on flat PC with an EQE of only 17%, an enhancement factor of 2.2. As predicted by simulations, the enhancement is mainly due to disruption of the surface plasmons.

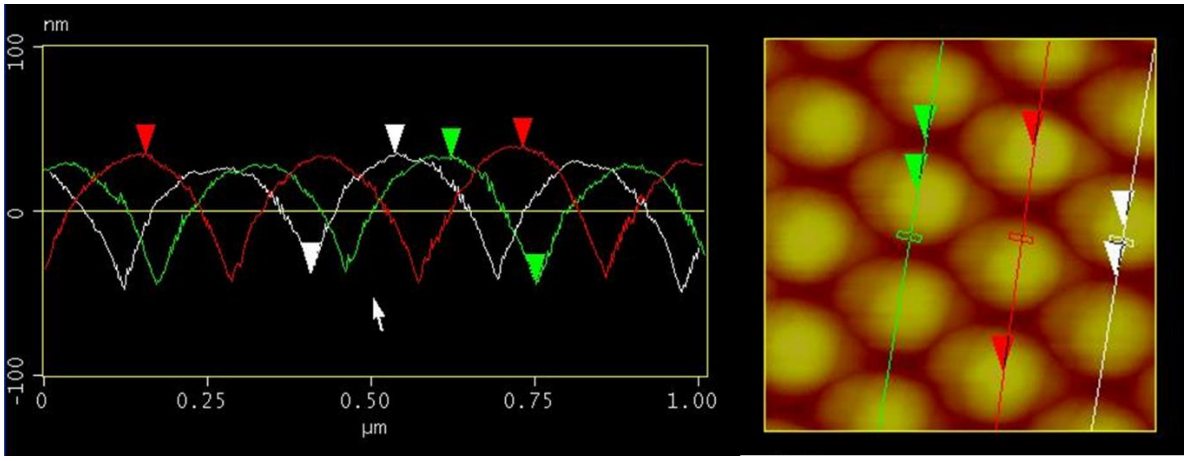

Figure 3.5: AFM section analysis of the Motheye corrugation.

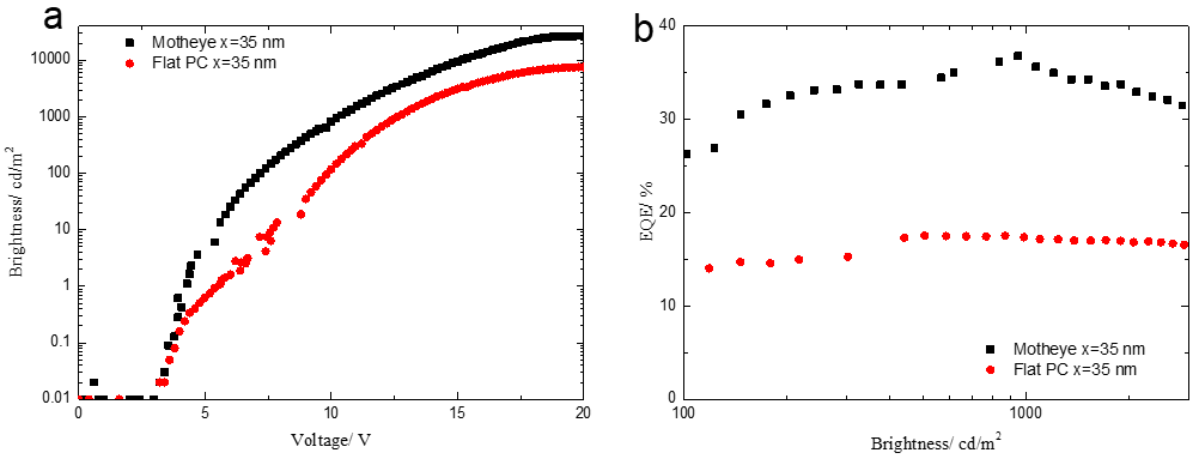

Figure 3.6: Device attributes for the green PhOLEDs on moth-eye corrugation. a) Brightness vs. voltage and b) EQE vs. brightness.

The second type of corrugation structures was dome-shaped with the pitch of 750 nm and a corrugation height of 80 nm. The green PhOLEDs fabricated on these corrugated PC substrates comprised of a 5 nm HAT-CN layer followed by an HTL with 60 nm of 10 wt.% MoO_3 doped into TAPC, and a 20 nm neat TAPC layer. The ETL consisted of a neat 20 nm TmPyPb followed by a 20 wt.% CsF-doped TmPyPb layer, which was either 20 nm or 40 nm.

The green emission was acquired by a 20 nm layer of 6 wt.% Ir(ppy)3 doped into mCP (**Figure 3.7**).

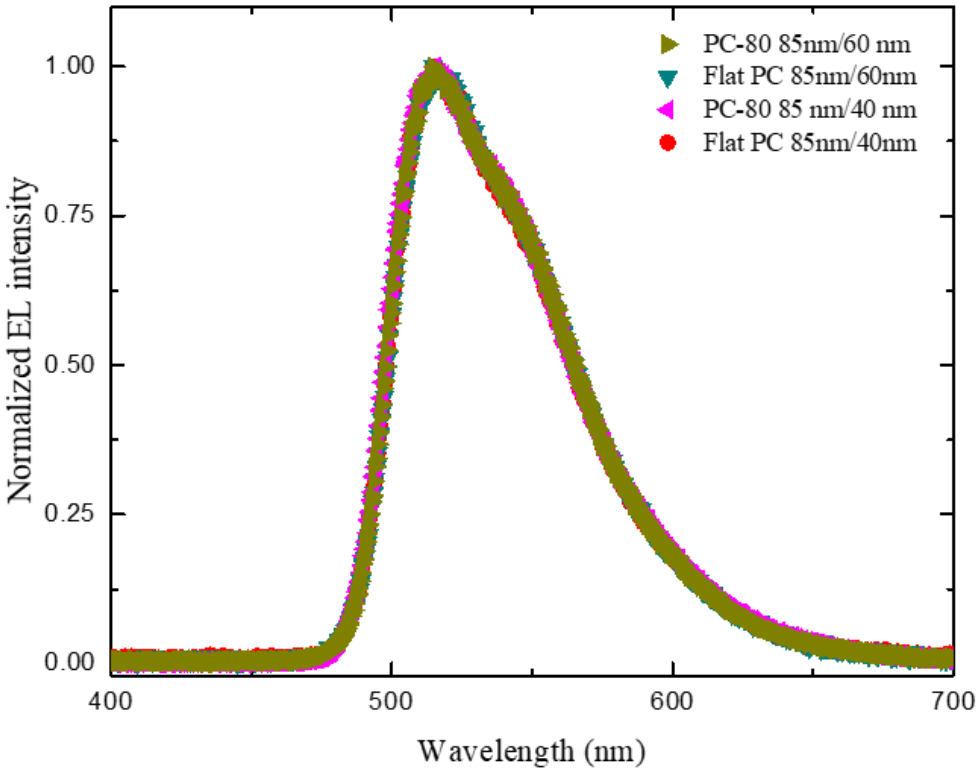

Figure 3.7: EL Spectra for the green PhOLED devices on PC substrates with and without the corrugation.

As illustrated in **Figure 3.8** it is evident the enhancement in all efficiency quantities is mainly due to the mitigation of the plasmon loss in the periodic structure, plus a minor contribution from the reduced substrate and internal waveguiding modes. The device efficiencies were enhanced when using the corrugated structure even with a thin ETL layer of 40 nm. In comparison to the flat device with similar thin ETL thickness, the EQE (**Figure 3.8d**) improved from 19.6% to 24.8% in the corrugated structure with 80 nm feature height resulting in an enhancement factor of 1.3. As the total ETL thickness increased from 40 nm to 60 nm, the corresponding device on the flat PC improved its efficiency up to 21.2% by further

reducing the surface plasmon loss. The comparable OLED on corrugated PC improved the EQE up to 40% by further reduction of the surface plasmons that were already reduced by the thicker ETL. The corrugated device structure yields enhancement factors of 1.9 and 2.0 over the devices on flat PC with similar structure and the flat device with 40 nm ETL thickness, respectively.

The current efficiency or the luminous efficiency **(Figure 3.8b**) was also enhanced over the flat devices; the highest current efficiency was 141 cd/A obtained from a corrugated device with a 60 nm ETL thickness an enhancement factor of 1.9 over the corresponding flat device with 74 cd/A. This device also yielded the highest power efficiency (**Figure 3.8c**) of 114 lm/W, an enhancement factor of 2.2 over the 53 lm/W of the flat device.

As demonstrated, to minimize the surface plasmon losses, a corrugated device is a better solution than increasing the ETL thickness in order to move the emissive layer away from the cathode. At the same time, it is very important to maintain the corrugation through the entire organic stack up to the cathode, since the corrugated cathode is more important in minimizing surface plasmon loss.

To demonstrate the importance of maintaining the corrugation at the cathode, an OLED with thick HTL and ETL was fabricated on a shallow corrugation. This particular device structure was responsible for the 50% EQE reported in Chapter 2. The shallow corrugation was expected to get filled by the 120 nm HTL. The device fabricated on both shallow corrugation and the flat PC resulted in EQEs (**Figure 3.9**) similar to each other, indicating no enhancement despite the substrate corrugation. Filling of the corrugation with organic layers resulted in a flat Al cathode that produces waveguiding and substrate modes in the device and suppresses

the outcoupling. Though there is an ETL with a thickness of 60 nm, some generated photons can be dissipated as surface plasmons since the surface plasmons are energized by waveguided light.

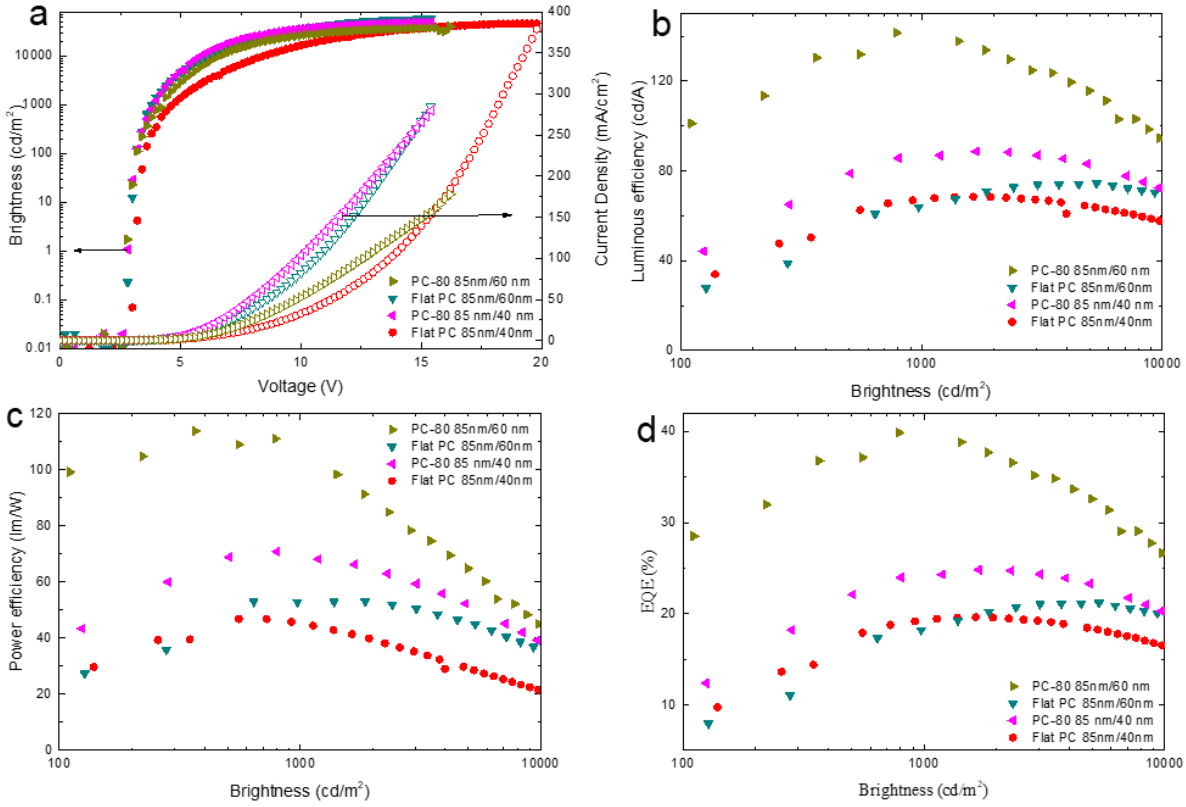

Figure 3.8: The performances of OLEDs fabricated on corrugated PC with feature height 80 nm and on flat PC. a) Current density-brightness-voltage plot, b) Luminous efficiency vs. Brightness, c) Power efficiency vs. Brightness and EQE vs. Brightness.

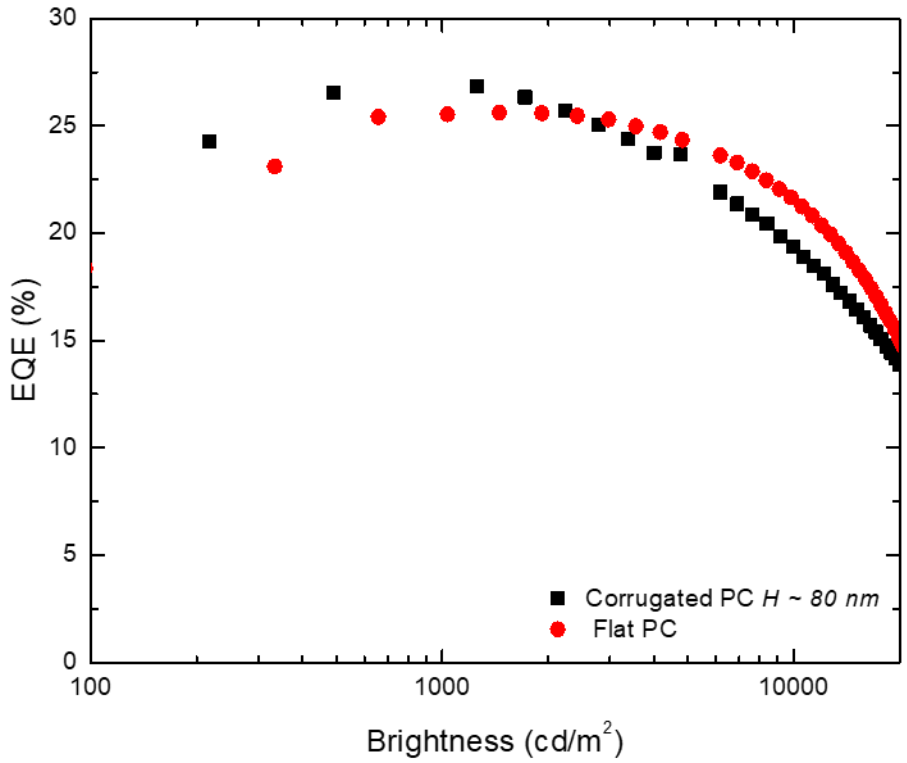

Figure 3.9: EQE for the OLED with thick HTL fabricated on shallow corrugation with 80 nm feature height and on flat PC.

3.4. Conclusion

We demonstrated that light outcoupling could be enhanced by minimizing the surface plasmons loss at the organic/metal interface. Increasing the distance between the emissive layer and the Al cathode is one approach, but it is important to keep a good conductivity in the device. Therefore, proper doping of the ETL is identified as a critical component in this approach. As the ETL thickness increased, charge imbalance at the EML needed to be adjusted by changing the HTL thickness appropriately. Taking all the mentioned parameters into consideration, we demonstrated an EQE enhancement in a two-color white OLED by a factor of 2.3, increasing EQE from 9.1% up to 21% for a device with optimized total HTL thickness of 160 nm and a total ETL thickness of 40 nm.

As the thickness of the ETL increased to reduce the surface plasmon loss, a weak microcavity effect was noticed in the device, changing its relative emission peaks. For the device with best EQE of 21%, the orange emission from PO-01 was suppressed as a result of the weak microcavity effect. With the help of theoretical simulations, it was shown that the surface plasmons could be disrupted using a shallow corrugation at the metal cathode. The EQE enhancement was validated for two different corrugation types. First, an EQE enhancement factor of 2.2 was observed for a device fabricated on a moth-eye structure, where the corrugation height was 80 nm with a pitch of 275 nm. The EQE for the best green device fabricated on this corrugation was 37% while the corresponding flat device yielded 17% EQE. Using a dome shape corrugation with a pitch of 750 nm and feature height of 80 nm, the EQE was boosted up to 40% with an enhancement factor of 1.9 over the controlled flat device where the EQE was only 21.2%.

3.5. Experimental Section

3.5.1. Materials

The conducting anode polymer PEDOT:PSS was purchased from H.C Starck. HAT-CN, TAPC, TmPyPb, mCP, $Ir(ppy)_3$, FIrpic, and PO-01 were purchased from Luminescence Technology Corporation. LiF was purchased from Sigma-Aldrich, and MoO_3 was purchased from Sterm Chemicals. The flat and the corrugated PC with various pitches and heights were fabricated and provided by Microcontinuum, Inc.

3.5.2. Anode Fabrication

The PEDOT:PSS was mixed with 6 vol.% ethylene glycol (EG) and 1 vol.% FS35 fluorosurfactant. The mixture was mixed in an ultrasonic bath for 90 mins before filtering using a 0.45 μm syringe filter. The mixed solution was kept in a refrigerator overnight to remove any

bubbles formed during the mixing. A single layer of PEDOT:PSS was deposited using a Laurell WS-650MZ-23NPPB spin-coater at a 6000 rpm spin speed for 30s. the formed uniform film was then annealed at 120 ^{o}C for 1 hour in the air and for 1 hour in a glove-box maintained at < 10ppm O_2 level. The ITO was deposited on PET substrates by Microcontinuum, Inc. using sputtering mechanism at room temperature.

3.5.3. OLED Fabrication and Characterization

OLEDs were fabricated on flat glass/ITO, flat PET/ITO, flat PC/PEDOT:PSS and on corrugated PC/PEDOT:PSS substrates/anodes. All the organic layers with and without the inorganic dopants were deposited in a vacuum thermal evaporator with a base pressure of 10^{-7} mbar. During the doped layer depositions, the dopant deposition rate was first set using a Maxtek TM 100 thickness monitor connected to a quartz crystal microbalance (QCM) and the host material was evaporated at a 1 Å/s deposition rate to achieve the desired doping concentration. The Al cathode was then evaporated through a shadow mask with 1.5 mm diameter circular openings to define the pixel area. For the characterization, the OLED pixels were driven using a Keithley 2400 source meter by applying a voltage and measuring the current. The Luminescence (brightness) of the device was measured using a Konica Minolta LS110 luminance meter focused to the center of the working pixel. The EL spectra were acquired using an OceanOptics ISP-30-6-1 integrating sphere connected to an OceanOptics HR2000+ spectrometer. The OceanOptics spectrometer was calibrated using an OceanOptics HL-3 plus light source prior to measuring the device EL. The normalized EL spectra were then used to calculate the EQE.

3.6. References

(1) Tang, C. W.; Vanslyke, S. A. Organic Electroluminescent Diodes. *Appl. Phys. Lett.* **1987**, *51* (12), 913–915.

(2) Prasad, S. OLED-Based Biochemical Sensors. In *Organic Light-Emitting Diodes (OLEDs)*; Buckley, A., Ed.; Woodhead Publishing, 2013; pp 548–571.

(3) Baldo, M. A.; O'brien, D. F.; You, Y.; Shoustikov, A.; Sibley, S.; Thompson, M. E.; Forrest, S. R. Highly Efficient Phosphorescent Emission from Organic Electroluminescent Devices. *Nature* **1998**, *395*, 151–154.

(4) Endo, A.; Ogasawara, M.; Takahashi, A.; Yokoyama, D.; Kato, Y.; Adachi, C. Thermally Activated Delayed Fluorescence from Sn4+-Porphyrin Complexes and Their Application to Organic Light Emitting Diodes - A Novel Mechanism for Electroluminescence. *Adv. Mater.* **2009**, *21* (47), 4802–4806.

(5) Hobson, P. A.; Wasey, J. A. E.; Sage, I.; Barnes, W. L. The Role of Surface Plasmons in Organic Light-Emitting Diodes. *IEEE J. Sel. Top. Quantum Electron.* **2002**, *8* (2), 378–386.

(6) Park, J.-M.; Gan, Z.; Leung, W.; Lui, R.; Ye, Z.; Constant, K.; Shinar, J.; Shinar, R.; Ho, K.-M. Soft Holographic Interference Lithography Microlens for Enhanced Organic Light Emitting Diode Light Extraction. *Opt. Express* **2011**, *19* (S4), 786–792.

(7) Hippola, C.; Kaudal, R.; Manna, E.; Xiao, T.; Peer, A.; Biswas, R.; Slafer, W. D.; Trovato, T.; Shinar, J.; Shinar, R. Enhanced Light Extraction from OLEDs Fabricated on Patterned Plastic Substrates. *Adv. Opt. Mater.* **2018**, *6* (4), 1–11.

(8) Gifford, D. K.; Hall, D. G. Emission through One of Two Metal Electrodes of an Organic Light-Emitting Diode via Surface-Plasmon Cross Coupling. *Appl. Phys. Lett* **2002**, *81* (23), 4315–4317.

(9) Singh Mehta, D.; Saxena, K. Light Out-Coupling Strategies in Organic Light Emitting Devices. *Proc. ASID'06* **2006**, 198–201.

(10) Salzmann, I.; Heimel, G.; Oehzelt, M.; Winkler, S.; Koch, N. Molecular Electrical Doping of Organic Semiconductors: Fundamental Mechanisms and Emerging Dopant Design Rules. *Acc. Chem. Res.* **2016**, *49* (3), 370–378.

(11) Ritchie, R. H.; Arakawa, E. T.; Cowan, J. J.; Hamm, R. N. SURFACE-PLASMON RESONANCE EFFECT IN GRATING DIFFRACTION. *Phys. Rev. Lett.* **1968**, *21* (22), 1530–1533.

(12) Hobson, P. A.; Wedge, S.; Wasey, J. A. E.; Sage, I.; Barnes, W. L. Surface Plasmon Mediated Emission from Organic Light-Emitting Diodes. *Adv. Mater.* **2002**, *14* (19), 1393–1396.

(13) Feng, J.; Okamoto, T.; Kawata, S. Enhancement of Electroluminescence through a Two-Dimensional Corrugated Metal Film by Grating-Induced Surface-Plasmon Cross Coupling. *Opt. Lett.* **2005**, *30* (17), 2302–2304.

(14) Zhou, L.; Xiang, H.-Y.; Shen, S.; Li, Y.-Q.; Chen, J.-D.; Xie, H.-J.; Goldthorpe, I. A.; Chen, L.-S.; Lee, S.-T.; Tang, J.-X. High-Performance Flexible Organic Light-Emitting Diodes Using Embedded Silver Network Transparent Electrodes. *ACS Nano* **2014**, *8* (12), 12796–12805.

CHAPTER 4. BRIGHT DEEP BLUE TADF OLEDs: THE ROLE OF TRIPHENYLPHOSPHINE OXIDE IN NPB/TPBI:PPh_3O EXCIPLEX EMISSION

Modified from a manuscript published in *Advanced Optical Materials*

Chamika Hippola *[§], Dusan Danilovic *[§], Ujjal Bhattacharjee[§¥], Cesar Perez-Bolivar[‡], Pavel Anzenbacher[‡], K. A Niradha Sachinthani[#], Toby L. Nelson[#], Jacob W. Patrich [§¥], Ruth Shinar[$£], and Joseph Shinar*[§]

* Physics and Astronomy Department, Iowa State University, Ames, IA 50011, USA

[§] Ames Laboratory, US Department of Energy, Iowa State University, Ames, IA 50011, USA

[$] Electrical and Computer Engineering Department, Iowa State University Ames, IA 50011, USA

[£] Microelectronics Research Center, Iowa State University Ames, IA 50011, USA

[¥]Department of Chemistry, Iowa State University, Ames, IA, 50011, USA

[‡] Chemistry Department, Bowling Green State University, Bowling Green, OH 43403, USA

[#] Chemistry Department, Oklahoma State University, Stillwater, OK 74078, USA

4.1. Abstract

Very bright (~14,000 cdm^{-2}) very deep blue exciplex OLEDs peaking at ~435 nm, where the photopic response is ~0.033, and with CIE Color Coordinates (0.1850, 0.1265), are described. The OLED properties are interestingly linked to PPh_3O (triphenylphosphine oxide) and attributes of the emitting layer (EML) comprising NPB interfacing host:guest TPBI:PPh_3O 5:1 wt. ratio. A neat PPh_3O layer that is central for device performance follows the EML (NPB/TPBi:PPh_3O 5:1/PPh_3O). The bright EL originates from NPB/TPBi:PPh_3O exciplexes

involving triplets via TADF, as evident from the strong quenching of the photoluminescence (PL) by oxygen; interestingly, the monomolecular emission process. The transient PL decay times of an NPB/TPBi:PPh_3O 5:1/PPh_3O film are 43 ns in air vs. 136, 610, and weak ~2000 ns in N_2. For comparison, the respective PL decay times of films of NPB:TPBi are 16 ns in air vs. 131 and 600 ns in N_2, and of NPB:PPh_3O they are 29 ns in air vs. 56, 483, and weak ~2000 ns in N_2. It is suspected that slow emitting states are associated with a PPh_3O aggregate interacting with NPB.

4.2. Introduction

OLEDs are increasingly penetrating displays and solid state lighting systems due to their high brightness and contrast, flexibility, relative ease of large-scale manufacturing, and potentially higher efficiency and reduced cost; they are also promising for analytical applications [1,2]. To meet the increasing demands that these applications pose, improvement in efficiency is crucial, in particular for violet/deep blue OLEDs in analytical applications and white OLEDs (WOLEDs) for high color rendering index (CRI) in lighting applications. The development of PhOLEDs ushered in devices with internal quantum efficiencies approaching 100%, but the efficiency & stability of blue PhOLEDs, particularly deep blue, remains challenging [3–8]. In addition, for blue PhOLEDs, it is also challenging to find an appropriate host that has a triplet state energy higher than that of the guest, which is needed to realize efficient energy transfer.

Various fluorescent blue OLEDs have been studied. Deep blue fluorescent emitters have included, for example, (i) non-doped 9,10-bis(4'-triphenylsilylphenyl)anthracene (BTSA) [9–11], 9,10-bis(1,2-diphenyl styryl)anthracene (BDSA), [9] and 2-tert-butyl-9,10-bis[4-(1,2,2-triphenylvinyl)phenyl]anthracene (TPVAn) [11,12]. The EL of the BTSA-based OLEDs peaks at

436 nm, but the efficiency is limited to 1.3 cdA^{-1} and decreases beyond a current density of 10 $mAcm^{-2}$; the EL of the BDSA-based OLEDs peaks at 453 nm [9].

A more recent approach for developing efficient blue fluorescent emitters is the use of materials that exhibit TADF. Such materials are typically based on donor-acceptor interaction either in a single molecule or in two different molecules forming an exciplex [13–28]. Indeed, TADF in exciplex states, yielding OLEDs with an EL peaking at 468 nm and an external quantum efficiency EQE = 22.4% have been reported [29]. In another example involving exciplexes, a high EQE = 25% at 450 nm was achieved using bis[2-(diphenylphosphino) phenyl] ether oxide (DPEPO) as the host material and 10-(4-((4-(9H-carbazol-9-yl)phenyl) sulfonyl)phenyl)-9,9-dimethyl-9,10-dihydroacridine (CzAcSF) as the blue emitter [30]. A 37% EQE sky-blue emission (480 nm) was achieved using a spiroacridine-triazine (SpiroAC-TRZ) hybrid [27]. An OLED based on the synthesized TADF material Cz-TRZ3 ((9-(4-(4,6-diphenyl-1,3,5-triazin-2-yl)-2-methylphenyl)-3,6-dimethyl-9H-carbazole) and DMAC-DPS (Bis[4-(9,9-dimethyl-9,10-dihydroacridine)phenyl]sulfone)), showed a high EQE of 19.2% with peak emission at 432 nm [31]. However, their emission spectrum was broad, their operating voltage was high (i.e., their power efficiency was low), their maximum brightness was only a few thousand cd/m^2, and their stability is unknown. Other violet-to-sky-blue TADF exciplex OLEDs, where mCP was the donor and TPBi, BPhen, or 3PT2T (2,4,6-tris (3-(1H-pyrazol-1-yl)phenyl)-1,3,5-triazine) the acceptors, were reported [32]. Their EQEs were very low, ranging from 0.57% to 2.23%, with the highest EQE achieved for the mCP:BPhen exciplex, peaking at ~470 nm [32,33]. Thus, such exciplex OLEDs are still challenging as their EQE and/or power efficiencies, as well as their brightness, are low.

Aside from TADF OLEDs guest-host PhOLEDs were developed. The phosphorescent guests developed to date are typically heavy metal Ir, Pt, or Eu chelates. As an example, efficient blue PhOLEDs were obtained by using *fac*-(N-phenyl, N-methyl-benzinidazol-2-yl) iridium(III) (*fac*-Ir(pmp)$_3$) and *mer*-(N-phenyl, N-methyl-benzinidazol-2-yl) iridium(III) (*mer*-Ir(pmp)$_3$). EQEs of 14.4% and 10.1% using *mer*-Ir(pmp)$_3$ and *fac*-Ir(pmp)$_3$ were reported, with peak emission at 453 and 425 nm, respectively [34]. Yet stability issues also plague blue PhOLEDs [8] and for large-scale applications efficient all-organic (i.e., free of rare and expensive metal atoms) phosphors are desirable.

One material that fluoresces in the deep blue is the small molecule NPB, which is widely used as a hole transport material as well [7,35]. This material exhibits high thermal and morphological stability, as well as high hole mobility. However, due to the π-π stacking between its molecules, which promotes exciton quenching via dissociation, it is not a good neat emitter. Yet it has been widely used as a host for different metal-containing emitting dopants, such as iridium (III) bis(2-methyldibenzo [f,h]quinoxaline) (acetylacetonate) (Ir(MDQ)2(acac)) [36–38]. NPB:TPBi (2,2′,2"-(1,3,5-benzinetriyl)-tris(1-phenyl-1-H-benzimidazole))-based exciplex OLEDs yielded relatively efficient (maximum EQE = 2.7% at 600 cdm-2) exciplex-related deep blue emission peaking at 450 nm [35].

This paper describes novel, very bright (14,000 cd m^{-2}) deep blue (peak emission at ~435 nm, where the photopic response of the eye is ~0.033) EL from exciplex OLEDs based on a specific stack design with PPh_3O (triphenylphosphine oxide, or TPPO) being an essential component. The luminous efficiency and EQE, 3.6 cdA^{-1} and 4%, respectively, are relatively high in comparison to reported deep blue exciplex TADF emitters (EQE= 0.57%-1.2%) [32] and particularly NPB:TPBi exciplex OLEDs [35]. The stack also includes TCTA (tris(4-carbazoyl-

9-ylphenyl)amine; E_{HOMO} = -5.7 eV, E_{LUMO} = -2.4 eV), NPB (E_{HOMO} = -5.5 eV, E_{LUMO} = -2.4 eV), TPBi (2,2′,2"-(1,3,5-benzine-triyl)-tris(1-phenyl-1-H-benzimidazole; E_{HOMO} = -6.2 eV, E_{LUMO} = -2.7 eV), and BPhen (4,7-diphenyl-1,10-phenanthroline; E_{HOMO} = -6.4 eV, E_{LUMO} = -3.0 eV). The molecular structures are represented in **Figure 4.1**.

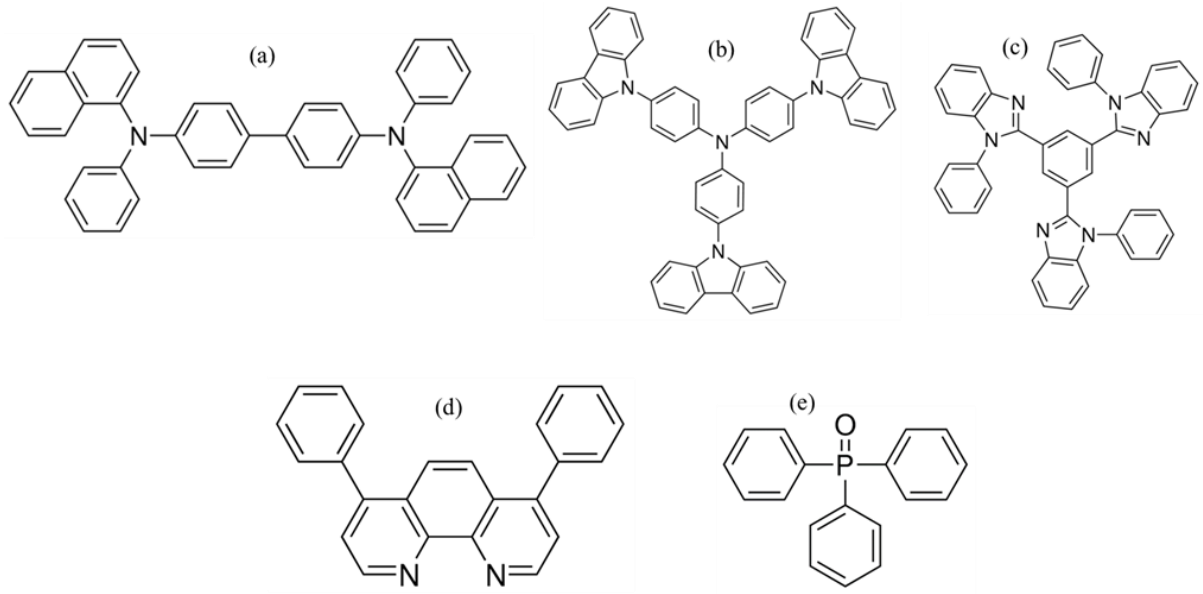

Figure 4.1: Molecular structures of a) NPB, b) TCTA, c) TPBi, d) BPhen and e) PPh_3O

Phenylphosphine oxides have attracted considerable attention [39–48]. Interestingly, E_{HOMO} and E_{LUMO} of the PPh_3O "parent" compound (**Figure 4.1**) have not been firmly established. The calculations and measurements on that and some closely related compounds [42] suggest a deep -6.5 ≤ E_{HOMO} ≤ -6.0 eV and a shallow -2.4 ≤ E_{LUMO} ≤ -1.5 eV, i.e., a large HOMO-LUMO gap E_g ~4.5 eV; the latter was confirmed by both optical absorption and Tauc plot measurement on films (**Figure 4.2 b, c**) [49]. There are, however, reports of the ionization energy of ~8.1 eV [39,50]. At the same time, PPh_3O is an excellent electron transport material [43–45]. The high E_g ~4.5 eV (λ ~275 nm) of the PPh_3O with the high polarity, electron withdrawing P=O groups, [51,52] allow for high triplet energy.

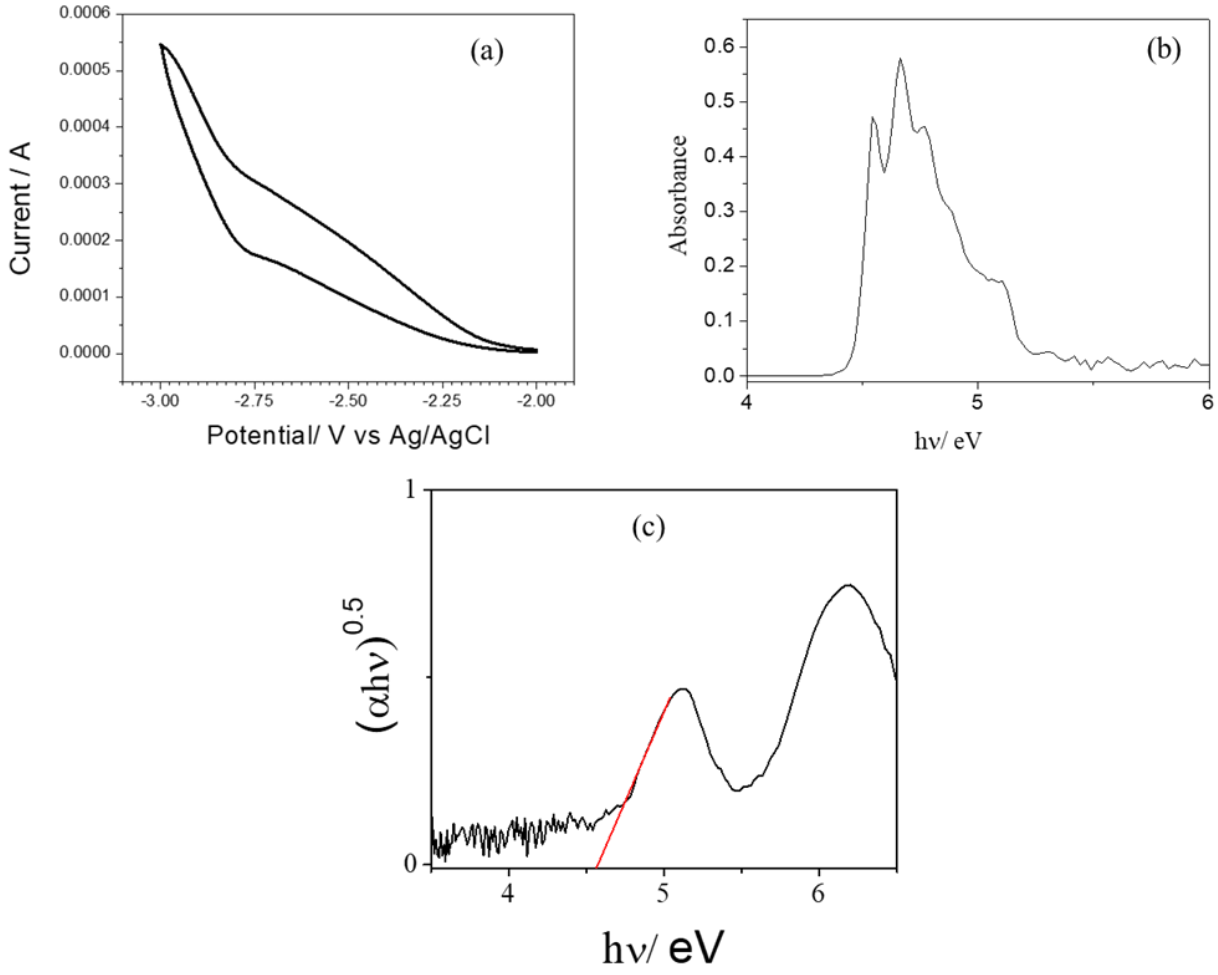

Figure 4.2: Assessing the PPh_3O energy levels and bandgap: (a) cyclic voltammogram of PPh_3O showing the reduction potential Ered = -2.83 eV; ferrocene was used as the standard for the calibration (b) absorption spectrum of PPh_3O in $CHCl_3$; the absorption edge is at 278 nm, yielding optical Eg = 4.46 eV (c) thin-film Tauc plot, yielding Eg = 4.57 eV.

4.3. Results and Discussion

The general structure of the devices studied was: ITO/ MoO_3 (5 nm)/ TCTA (60 nm)/ **EML**/ BPhen (30 nm)/ CsF (1.5 nm)/ Al (110 nm), with the EML of the optimized device (**Device A**) being NPB (45 nm)/ TPBi:PPh_3O (14 nm) (5:1 wt. ratio)/ PPh_3O (15 nm). The optimal 5:1 value was determined by varying the TPBi:PPh_3O ratio. Note that the actual emission zone is likely confined to NPB/TPBi:PPh_3O.

Device A attributes include peak emission at ~435 nm (**Figure 4.3**), CIE coordinates (0.1850,0.1265) shown in **Figure 4.4**, a maximum brightness of ~14,000 cdm^{-2}, and *EQE* of ~4%, all in the absence of any outcoupling-enhancing structures (see **Figure 4.5** and **Table 4.1**). With the addition of low-pass 550 and 500 nm optical filters, the CIE coordinates become (0.1484, 0.0892) and (0.1503,0.0334), respectively (**Figure 4.4**).

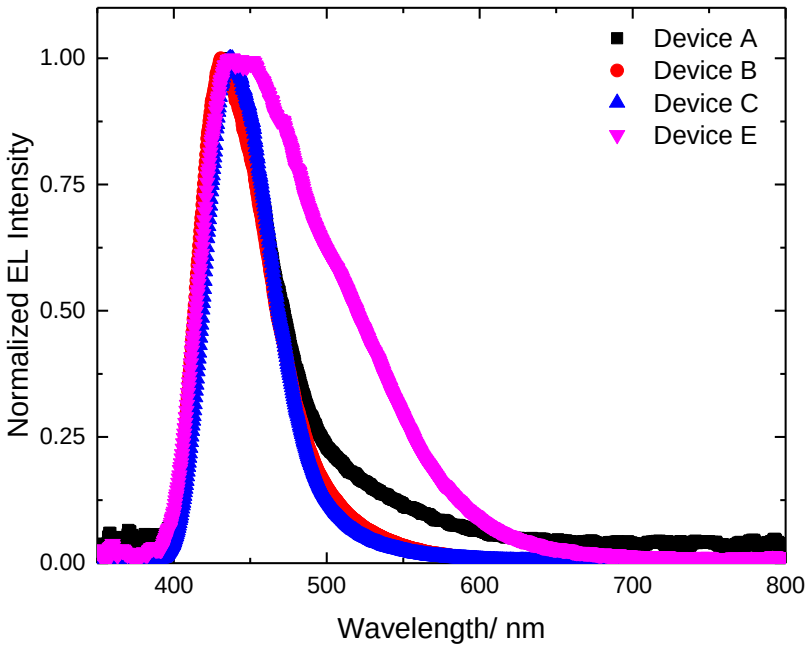

Figure 4.3: Electroluminescence spectra of devices A, B, C, and E

Interestingly, though commonly used successfully as a hole and exciton blocking layer, the BPhen layer was found to be necessary for improving device performance (**Table 4.1**; see **Device A** vs. **Device G**). The deep ~-3.0 eV LUMO of undoped BPhen is unlikely to efficiently inject electrons into the much shallower (possibly~1.8 eV) LUMO of the adjacent PPh_3O. However, CsF is known to *n*-dope BPhen, even when it is present only as a ~1.5 nm-thick layer adjacent to BPhen [53,54] and E_{LUMO} of *n*-doped BPhen is higher (less negative) than that of the undoped BPhen. Additionally, it is likely that a dipole is formed at the PPh_3O/*n*-doped BPhen

interface due also to the electron withdrawing properties of P=O [51,52]. That interface dipole would also lower the barrier for electron injection [49,55]. Such a situation was reported for the doped BPhen/HAT-CN interface in two separate studies, where the barrier for charge transfer was reduced by ~1 eV [49,55].

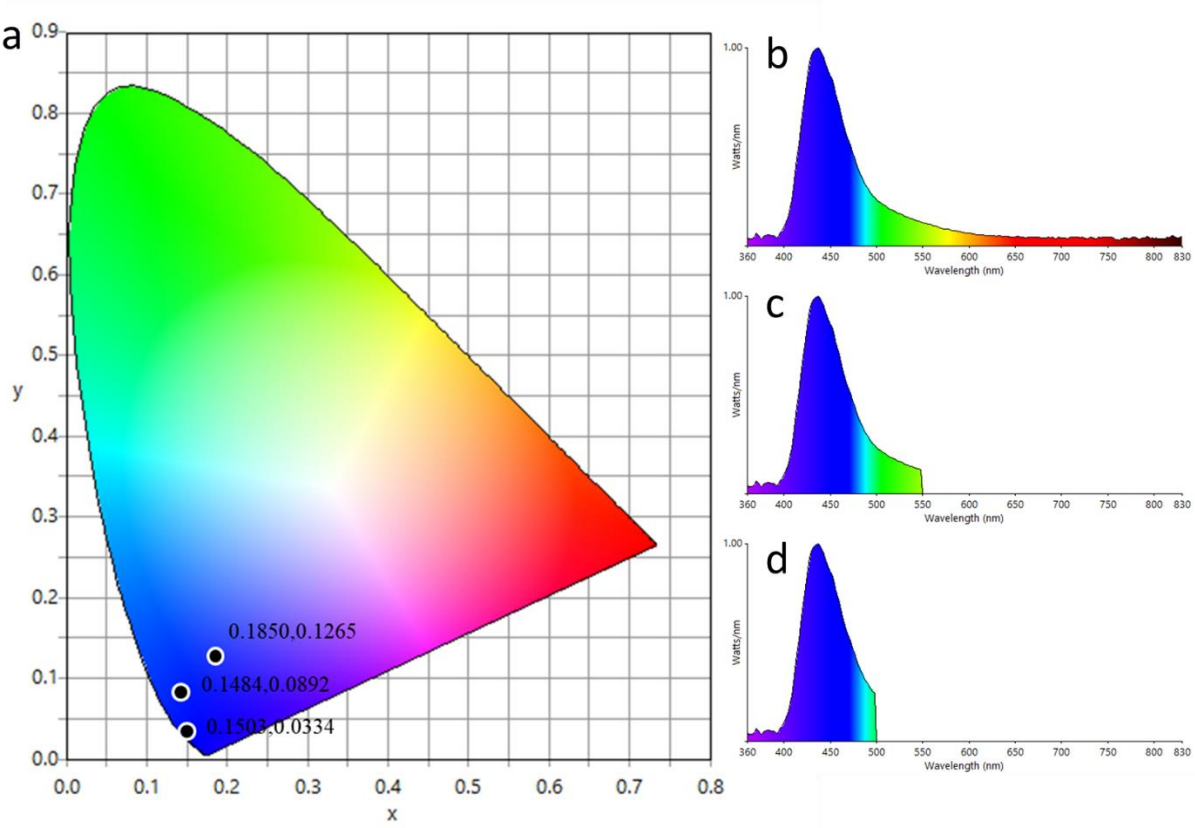

Figure 4.4: CIE color coordinates of Device A, EL Spectrum: b) full spectrum, c) spectrum cut-off above 550 nm and d) spectrum cut-off above 500 nm.

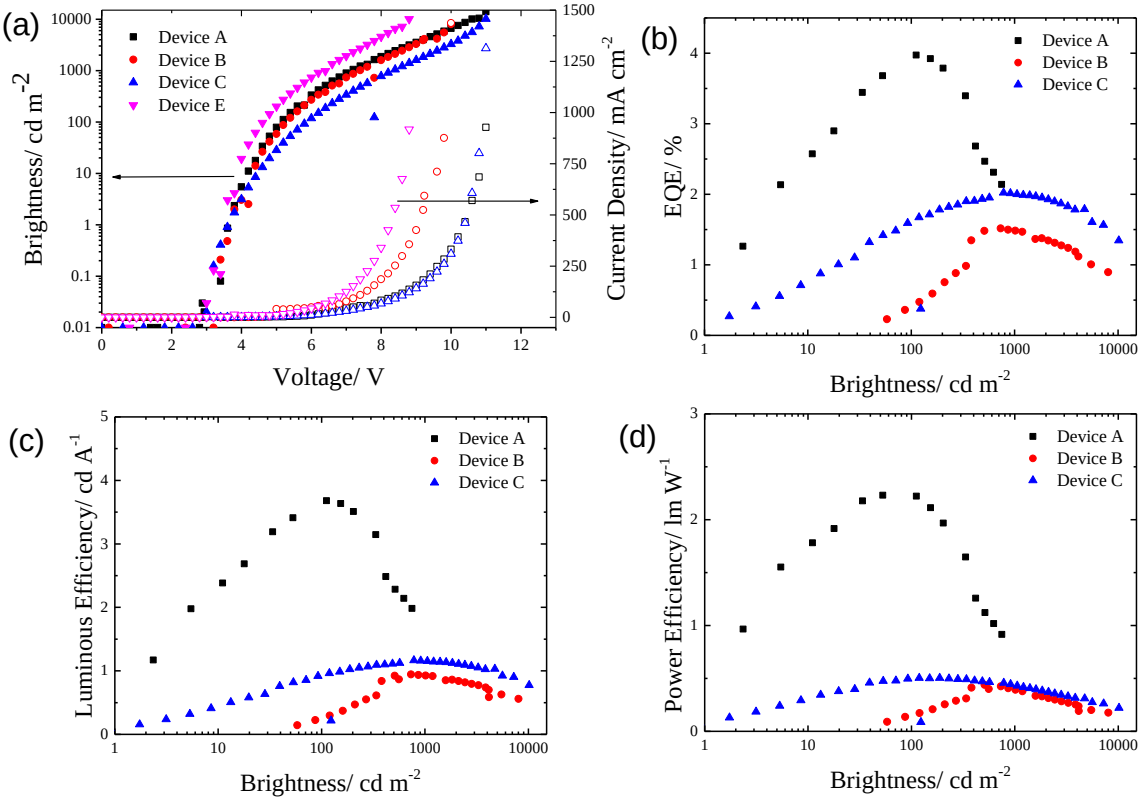

Figure 4.5: Attributes of non-encapsulated Devices A, B, C, and E (see Table 4.1) (a) J-L-V characteristics, (b)EQE, (c) luminous efficiency, and (d) power efficiency.

Also, interestingly, PPh_3O was essential for achieving the optimized **Device A** attributes. As seen in **Figure 4.6** a thermally evaporated film of PPh_3O only, excited at 240 nm in a N_2 atmosphere shows two PL bands, one peaking at ~285 nm (~4.4 eV; corresponding to bandgap emission) and the other at 395 nm (~3.1 eV). The transient PL decay time of the 395 nm emission is < 5 ns in both air and nitrogen, indicating prompt fluorescence. The origin of the band that band is unclear and may be associated with aggregates/ excimer.

Table 4.1: Devices' A - I EML structure, turn on voltage (brightness = 1 cdm^{-2}), peak EL wavelength, peak brightness, luminous efficiency, power efficiency, and EQE

Device	Nominal* Emission Layer (nm thickness)	Turn on Voltage (V)	Peak EL (nm)	Peak Brightness (Cd m^{-2})	Peak Luminous Efficiency (Cd A^{-1})	Peak Power Efficiency (lm W^{-1})	Peak EQE (%)
A	NPB(45)/TPBi:PPh_3O 5:1(14)/PPh_3O(15)	3.6	435	13,970	3.60	2.23	4.0
B	NPB(45)	3.7	433	8,030	0.94	0.58	1.5
C	NPB(45)/TPBi(30)	3.6	437	10,170	1.16	0.50	2.0
D	NPB(45)/NPB:TPBi 1:1(30)	4.0	434	6,170	0.9	0.48	1.5
E	NPB(45)/PPh_3O(15)	3.5	442	10,070	1.74	1.02	1.2
F	NPB(45)/TPBi (14)/PPh_3O(15)	3.7	432	11,950	1.54	0.68	1.7
G	NPB(45)/TPBi:PPh_3O 5:1 (14)/PPh_3O(15) (No BPhen)	4.5	435	6,840	0.58	0.29	0.8
H	NPB(45)/NPB:TPBi 1:1 (30)/TPBi(30)	3.9	442	8,410	1.18	0.60	1.9

To elucidate the origin of the strong deep blue emission of this foregoing optimal **Device A**, multiple devices were fabricated and characterized (see **Table 4.1** for a summary and **Figure 4.5**). Additionally, PL spectra, absorbance and PL excitation spectra, PL spectra, and transient PL decay times of different films, most of the EML structures, were monitored in air and in nitrogen. **Table 4.1** shows the EML layer structure and its thickness, the turn-on voltage of the devices, their peak EL wavelength, brightness, luminous efficiency, power efficiency, and EQE. Transient PL decay times of the various EML (multilayer) films are shown in **Table 4.2.**

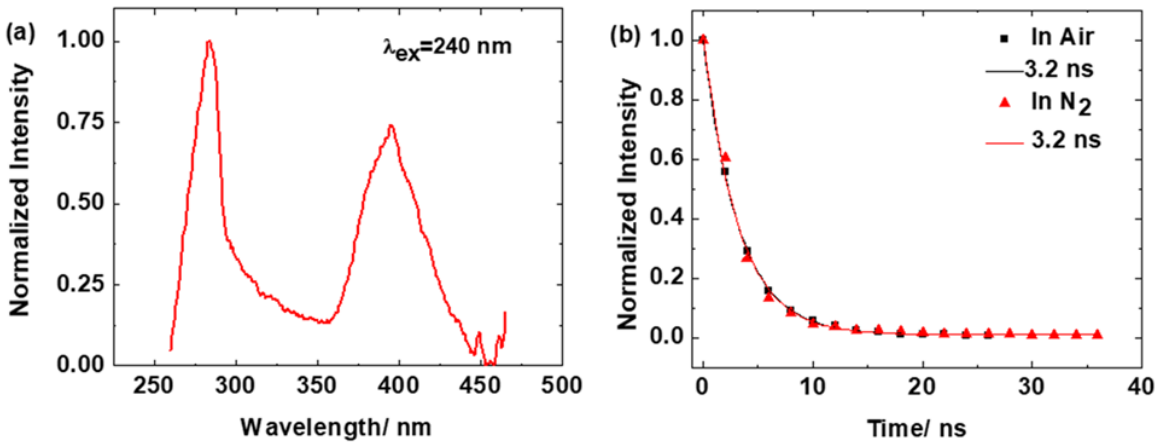

Figure 4.6: (a) Steady-state PL spectrum of a PPh_3O film encapsulated in N_2 excited at 240 nm (b) the PPh_3O transient PL decay curve at λ_{em}= 400 nm in air (black) and in nitrogen (red), where the film was encapsulated. Note that the PL decay constant τ_{PL} < 5 ns both cases, i.e., encapsulation does not increase τ_{PL} to > 5 ns, which would be expected for phosphorescent decay.

Table 4.2: PL decay times of the thin films.

Film Structure	PL Decay Time in Air** (ns)	PL Decay Time in N_2 (ns)
NPB/TPBi:PPh_3O(5:1)/PPh_3O	43	136, 610, ~2000
NPB:TPBi 1:1***	16	131, 600
PPh_3O	<5 at 395 nm 8 at 500 nm	<5 at 395 nm 18 at 500 nm
NPB:PPh_3O 1:1	29	56, 482, ~2000
NPB***, TPBi, TCTA, TPBi:PPh_3O	<5	< 5 (measured for NPB and TPBi:PPh_3O)

*the actual emission zone is narrower occurring around the NPB/adjacent material interface (see text).
**Any decay faster than 5 ns is below our instrument time resolution of 5 ns.
***excitation wavelength was 355 nm; the rest, 266 nm.

As mentioned, **Device A** exhibited the best performance with peak emission at ~435 nm, the brightness of ~14,000 cdm^{-2}, and *EQE* of ~4% in the absence of any outcoupling-enhancing structures. The photopic response of the eye is only 0.033 at 435 nm, and it varies from 0.0098 to 0.0803 in the 413 to 467 nm range (the ~54 nm full width at half maximum (FWHM) of the EL band).

Importantly, the transient PL decay times of the NPB/TPBi:PPh_3O 5:1/PPh_3O multilayer film (EML of **Device A**) indicated formation of triplet exciplexes, as the emission was quenched by oxygen; the PL decay times are 43 ns in air *vs.* 136 and 610 ns, at a ratio of 4:1, in nitrogen, as well as a weaker PL with a ~2000 ns decay time. We note that the PL decay times are shorter than in other reported TADF systems [17]. **Figure 4.7** shows the PL decay curves in air and in N_2 of the EML of **Device A**, NPB/TPBi:PPh_3O 5:1/ PPh_3O and for

comparison of its constituents NPB:TPBi and NPB:PPh_3O films. The PL intensities *vs.* the excitation fluence shown in **Figure 4.8** indicates a monomolecular process, are also shown. The prompt fluorescence of a 45 nm NPB layer excited with 5 ns pulse at 266 nm or 355 nm decayed, as expected, at < 5 ns (**Figure 4.9**).

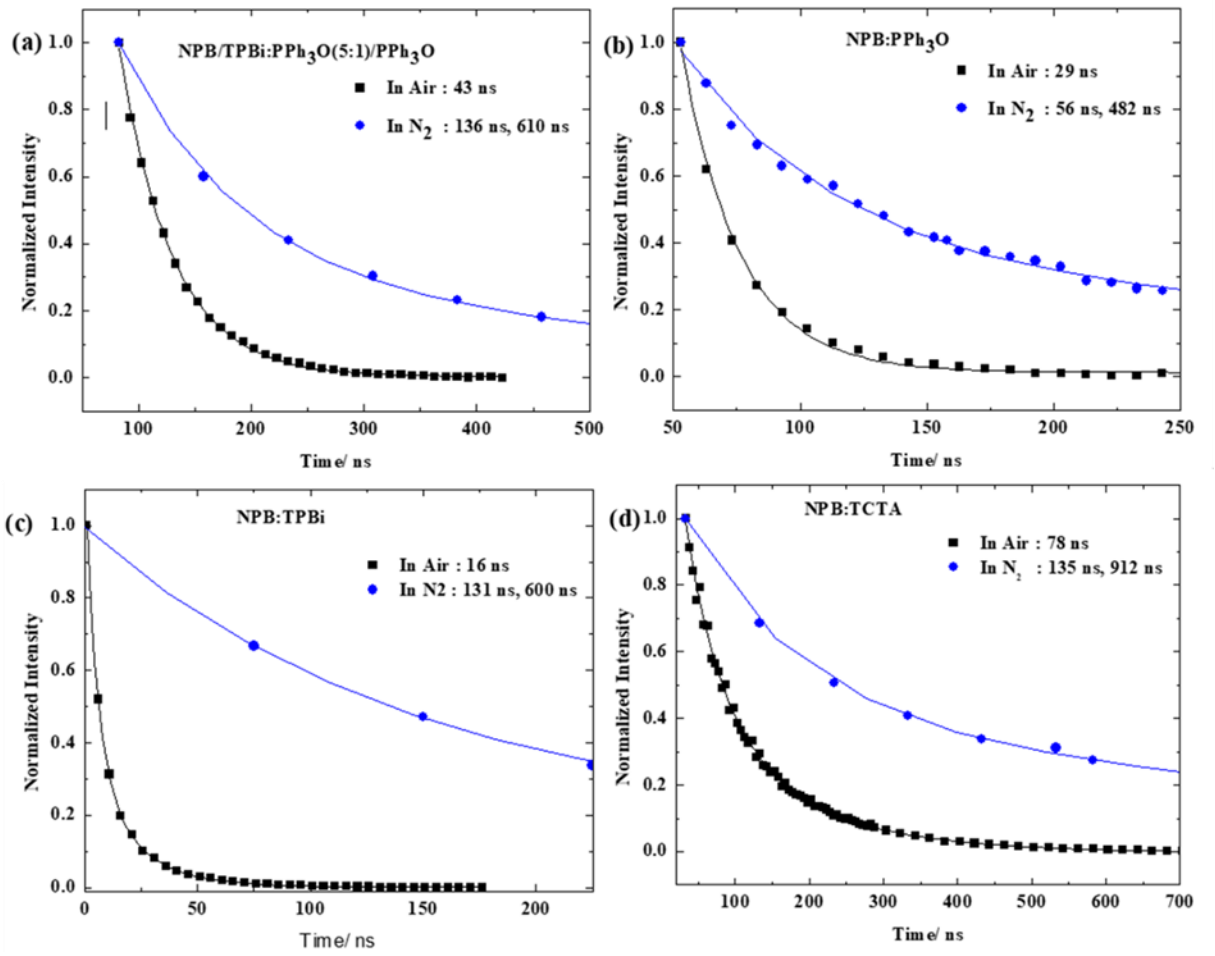

Figure 4.7: PL decay curves in air and in N_2 of (a) NPB/TPBi:PPh_3O (5:1)/PPh_3O, (b) NPB:PPh_3O 1:1, (c) NPB:TPBi 1:1, and (d) NPB:TCTA 1:1.

Unexpectedly, a film of NPB:PPh_3O, unlike that of TPBi:PPh_3O, indicated the formation of an exciplex. This is unexpected because of the HOMO and LUMO levels of NPB, which lies within the HOMO-LUMO gap of PPh_3O. However, the PL decay times (**Figure 4.7** and **Table 4.2**) of a 1:1 NPB:PPh_3O film were 29 ns in air and 56, 482 ns , at a ratio of 4:1,

with additionally a weak ~2000 ns decaying component in N_2. We, therefore, speculate that these slowly emitting states involve PPh_3O aggregates interacting with NPB. The facile crystallization properties of PPh_3O [56] may render this interaction plausible.

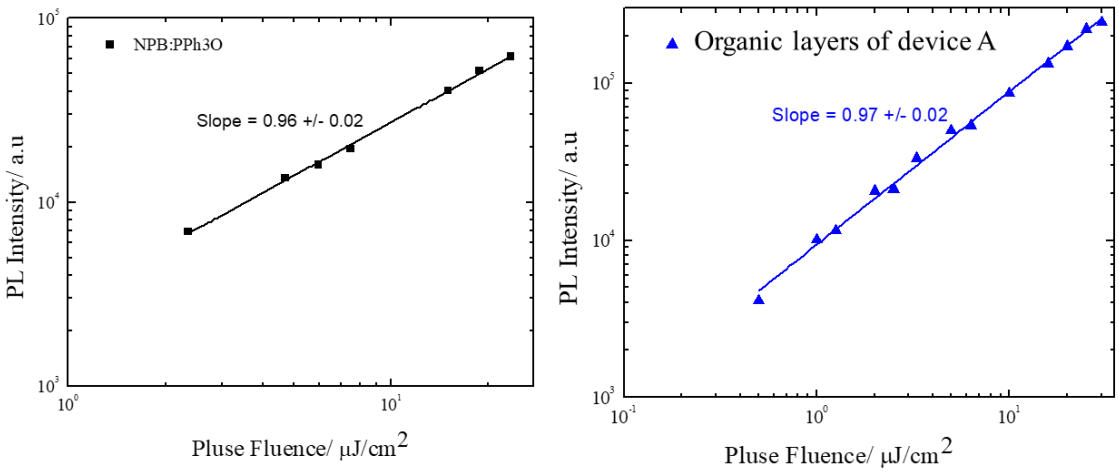

Figure 4.8:PL intensity vs. the laser's fluence for films encapsulated in N2: NPB:PPh3O and the organic layers of Device A; recorded from 100 ns to 5 μs.

Figure 4.10 shows the absorption and excitation spectra of these films; the absorption and excitation spectra of TPBi:PPh_3O coincide, indicating no interaction, unlike the case for NPB:PPh_3O, which is supported by the PL emission peak and decay times. The PL peak emission of NPB:PPh_3O and TPBi:PPh_3O films were at ~460 nm and 386 nm, respectively, whereas those of NPB and TPBi were ~437 nm and ~400 nm; as mentioned the PL of a PPh_3O film peaks at ~285 and ~395 nm. Moreover, the PL decay times (**Figure 4.7** and **Table 1**) of a NPB:PPh_3O film were 29 ns in air and 56, 482, and weak ~2000 ns in N_2, whereas the PL decay times of a TPBi:PPh_3O film in air and in N_2 were < 5 ns. A NPB:TPBi film showed PL decay times of 16 ns in air and 131 and 600 ns in N_2, (**Figure 4.7**). As seen, the PL decays times of NPB:TPBi:PPh_3O/PPh_3O (136, 610 and ~ weak 2000 ns in N_2) combine those of NPB:TPBi and NPB:PPh_3O films, providing a "fingerprint" of the NPB:PPh_3O exciplex.

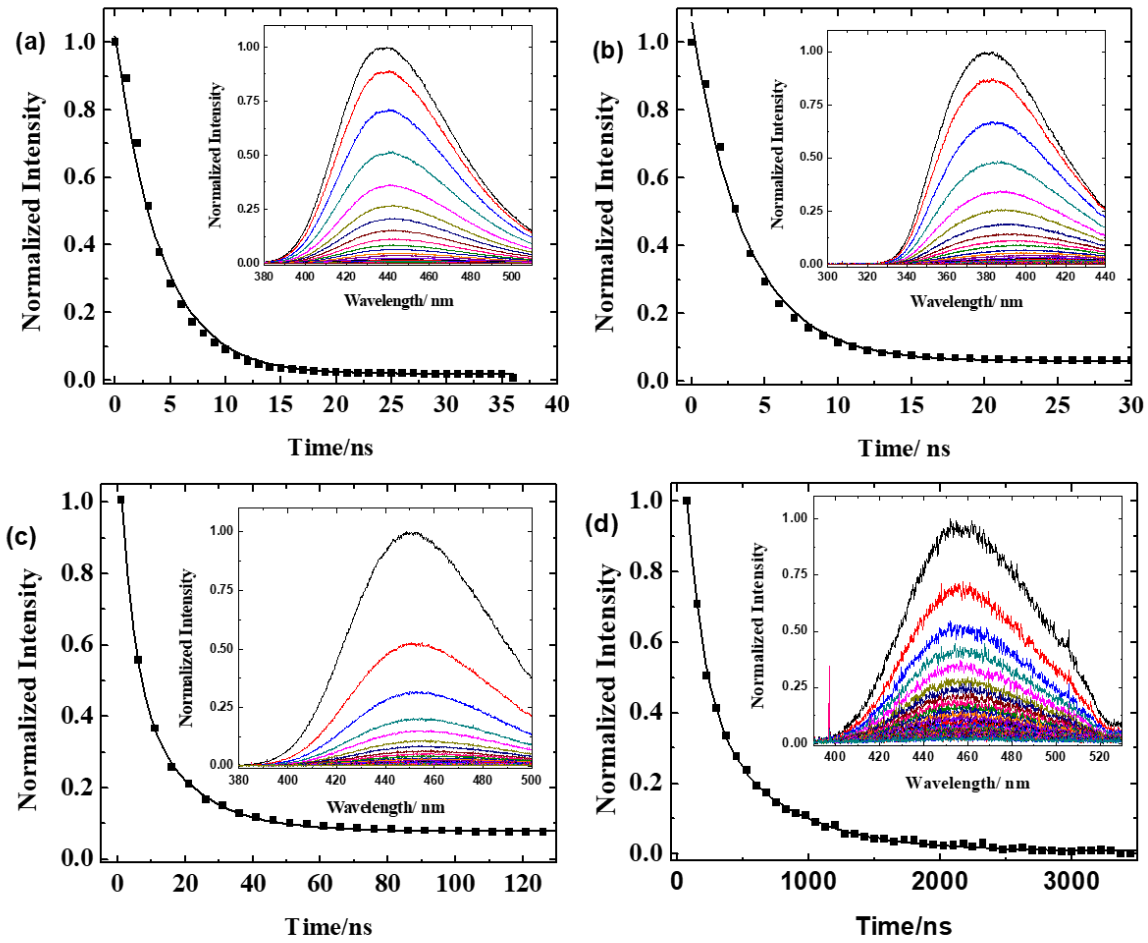

Figure 4.9: Transient PL decay of a) Pure NPB, b) Pure TPBi, c) A mixed NPB:TPBi 1:1 film in air and d) NPB:TPBi 1:1 film in N_2. The inset shows the PL spectra at different times following the laser pulse.

As also seen in **Figure 4.9**, the PL of NPB film peaks at ~437 nm, whereas that of an NPB:TPBi film peaks at ~450-455 nm (**Figure 4.9c**). The PL of NPB/TPBi:PPh_3O 5:1/PPh_3O, like that of NPB:PPh_3O, peak at ~460 nm in N_2 (**Figure 4.11**). The shorter EL peak emissions are likely due to microcavity effects, which would tend to maximize emission at a wavelength λ/n (where n is the refractive index) that is 4 times the ETL thickness.

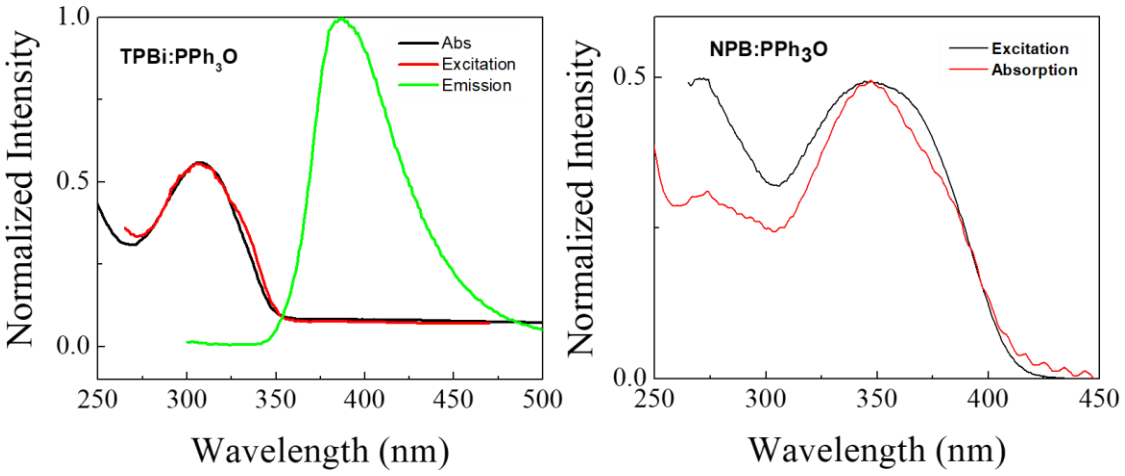

Figure 4.10:Absorption and excitation spectra of TPBi:PPh_3O and NPB:PPh_3O films. The emission spectrum of TPBi:PPh_3O is also shown.

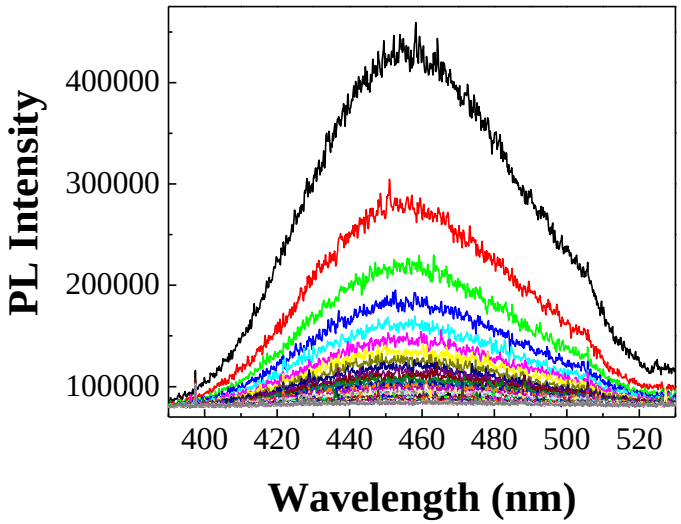

Figure 4.11: Transient PL decay of NPB:PPh_3O (1:1).

The contribution of the prompt fluorescence of NPB Φ_{PF} (NPB was essential for device optimization, **Figure 4.12**) in N_2 to the total EL in the aforementioned films can be estimated by comparing the PL intensity in N_2 *vs.* air. If most of the PL is due to delayed emission involving triplets, then the ratio of the PL intensity in N_2 to that in air would be $\sim(\Phi_{PF}+\Phi_T)/\Phi_{PF}$

[17], where Φ_T is the delayed emission contribution. For NPB:TPBi, this ratio is ~5.2; for the EML of **Device A**, it is ~3.4. Hence, most of the PL and EL are due to the various exciplex triplets. Importantly, the short EL peak wavelength of ~435 nm of **Device A** and the monomolecular PL intensity vs. pulse fluence for NPB/TPBi:PPh_3O/PPh_3O and NPB:PPh_3O exclude triplet-triplet annihilation (TTA) that was observed for NPB:TPBi-based OLEDs [35]. These and the following results emphasize the unique role of PPh_3O, as both a guest and a neat film, in affecting device performance.

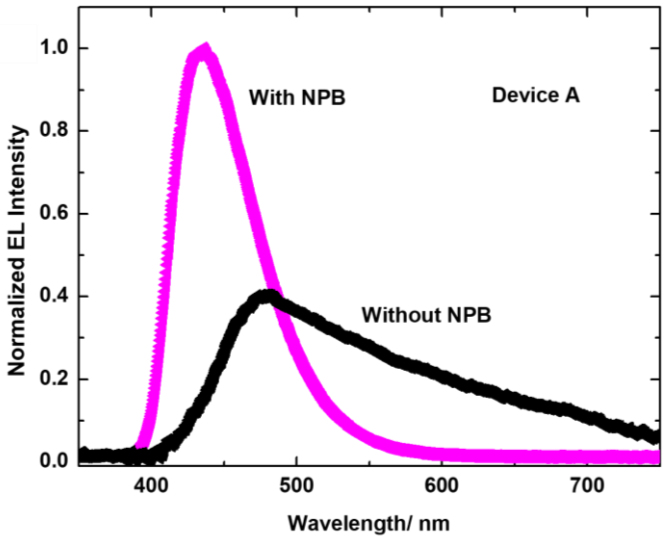

Figure 4.12: EL spectra of Device A with and without NPB.

As it is now clear, the formation of exciplexes between the constituents of **Device A** EML and the strong quenching effect of the PL by oxygen allude to a TADF process. The EQE of ~4% and 14,000 cd/m^2 brightness of **Device A** are much higher than that of the reported respective 1.2% and 900 cd/m^2 deep blue (428 nm) exciplex TADF device [57]. We cannot, however, exclude other emission mechanisms due to the unexpected interactions of PPh_3O.

To further analyze the performance of **Device A**, other devices were evaluated, as summarized in **Table 4.1**. The EMLs of **Devices B** to **F** were (B) NPB, (C) NPB/TPBi, (D) NPB/NPB:TPBi 1:1, (E) NPB/PPh_3O, and (F) NPB/TPBi. As detailed next, the performance of these devices indicated the possible role of the various EML components and their interface interactions in producing the optimized **Device A**.

All the devices showed EL peaking at ~433 to 442 nm (with the wavelength checked against known precise emitters); **Device B**, with neat NPB as the EML, showed a fluorescent EL peak at λ_{max} = 433 nm (as mentioned, the relatively short λ_{max} is likely due to a weak microcavity effect) with a PL decay time < 5 ns (**Figure 4.9a**). The device was bright (> 8,000 cdm^{-2}) with efficiencies that are high (**Table 4.1**) for such deep blue NPB OLEDs [18].

Devices C-F, whose optical properties are detailed below, and **Devices G** and **H** were all inferior to **Device A** (**Table 4.1**); they were tested to determine the optimal multilayer EML and to evaluate interface interaction between the EML constituents. **Device G**, which is identical to **Device A** but without the BPhen layer, highlights the important role of the presumably doped BPhen in improving electron injection, as discussed above.

Device E with an NPB/PPh_3O EML showed a brightness of 10,070 cdm^{-2} peaking at 442 nm and an EQE of 1.2%.

TPBi:PPh_3O did not form an exciplex based on the identical absorbance and PL excitation spectra and the fast PL decay times of < 5 ns. However, TPBi improved the **Device F** (EML NPB/TPBi/PPh_3O) attributes in comparison to **Device E** that is devoid of TPBi, leading to an EQE = 1.7% with peak emission at 432 nm (see **Table 4.1**).

In summary, the results showed a reproducible, extremely bright and relatively efficient (~14,000 cdm^{-2} and ~4% EQE) deep blue (peak EL at ~435 nm, CIE coordinates (0.1850, 0.1265)), TADF exciplex-based **Device A** with the structure ITO/5 nm MoO_3/60 nm TCTA/45 nm NPB/14 nm TPBi:PPh_3O (5:1 wt. ratio)/15 nm PPh_3O/30 nm BPhen/1.5 nm CsF/110 nm Al. This structure was key for the enhanced device attributes as shown by comparison with other devices with structures that included different combinations of the constituents of **Device A**. The EL is dominated by exciplex formation of NPB with each of TPBi and, surprisingly, PPh_3O, as confirmed by absorption and excitation spectra of various films as well as measurements of PL intensities and decay times in air and in nitrogen. The PL process was monomolecular excluding TTA and alluding to a TADF process, though other mechanisms cannot be excluded. Notably, the PL of a film of **Device A**'s EML was 5.2x more intense in N_2 than in air. The results also show the importance of the *n*-doped BPhen in contributing to frontier orbitals favorable alignment. A contribution from NPB's fluorescence, enhanced by PPh_3O (due to the latter's excellent electron transporting properties) to the EL of the optimized **Device A** is likely also present.

4.4. Experimental Section

4.4.1. Materials

Nominally 140 nm thick ITO coated glass with sheet resistance 12 Ω/□ was purchased from Colorado Concept Coating LLC; it was used as a substrate for OLED fabrication. The hole injection material MoO_3 was purchased from Strem Chemicals and NPB from H.W Sands Corporation. TCTA and TPBi were purchased from Luminescence Technology (Lumtec) Corporation and the electron transport materials PPh_3O and BPhen, as well as the electron

injection material, CsF, were purchased from Sigma-Aldrich. The cathode material, Al, was purchased from Alfa Aesar.

4.4.2. OLED Fabrication

Prior to OLED fabrication, the glass/ITO substrates were cleaned using RBS-35 surfactant, acetone, and isopropanol and treated with UV-ozone to increase the work function. All the materials were evaporated inside a thermal vacuum evaporation chamber located inside a glovebox with <20 ppm oxygen at $<1.0\times10^{-6}$ mBar. A 5 nm MoO_3 was deposited on ITO as the hole injection layer at 0.2 Å/s followed by a 60 nm of hole transport material, TCTA at a rate of 0.4 Å /s. Different EMLs were deposited on TCTA. For the optimized **Device A**, a 45 nm NPB layer was deposited at a rate of 0.4-0.7 Å/s followed by co-evaporation of 14 nm of TPBi and PPh_3O at 0.5 Å/s and 0.1 Å/s, respectively, to obtain the 5:1 ratio. A neat 15 nm PPh_3O layer was deposited at 0.4 Å/s on top of the doped layer followed by 30 nm BPhen deposited at 0.4-0.7 Å/s. 1.5 nm of CsF, the electron injection layer, was deposited on BPhen at 0.1 Å/s. Finally, a 110 nm Al layer was deposited through a shadow mask with 1.5 mm diameter holes as the cathode. The neat layers in devices without a doped EML were deposited at a rate of 0.4-0.7 Å/s. Both materials in the doped EMLs with 1:1 ratio were deposited at 0.3 Å/s. The devices were not encapsulated.

4.4.3. Film Fabrication

For transient PL decay experiments, 2×1 cm^2 quartz substrates were used to avoid any signal originating from the substrate under UV excitation. Prior to deposition, all the quartz substrates were cleaned as described above. The cleaned substrates were transferred into the thermal evaporation chamber, and the layers were deposited under the same conditions used for device fabrication. The depositions were carried out through a 6×4 mm^2 shadow mask to

enable encapsulation. For neat films, a thickness of 30 nm was deposited at a rate of 0.4-0.7 Å/s. For doped films, a deposition rate of 0.3 Å/s was maintained in order to maintain the 1:1 ratio. In multilayer films, 45 nm NPB was deposited at 0.3 Å/s followed by a 14 nm TPBi:PPh_3O with a ratio 5:1 by maintained by deposition rates of 0.5 Å/s and 0.1 Å/s, respectively. A following 15 nm neat PPh_3O film was deposited at 0.5 Å/s. Samples were encapsulated in the N_2 atmosphere of the glovebox by covering the films with a quartz substrate and using Torr Seal at the edges.

4.4.4. Measurements

4.4.4.1. OLED characterization

A Keithley 2400 source meter was used for voltage application and current measurements. The EL was measured at each voltage step using a Minolta LS-110 luminance meter. The EL spectra were obtained using an Ocean Optics HR2000+ high-resolution spectrometer, which was calibrated using an Ocean Optics HL-3 plus calibrated light source.

4.4.4.2. Cyclic Voltammetry (CV)

CV was performed on a BASI CV-50W Version 2.3 instrument with 0.1 M tetrabutylammonium hexafluorophosphate as the supporting electrolyte in dry acetonitrile (CH_3CN) using a glassy carbon working electrode, a platinum wire as the counter electrode, and Ag/AgCl as the reference electrode with a scan rate of 100 mV s^{-1}. The CV experiments were performed with the PPh_3O in the electrolyte solution under argon atmosphere.

4.4.4.3. Absorption spectra

UV-Vis absorption spectrum of dilute PPh_3O solution in $CHCl_3$was recorded with a Cary 5000 UV-VIS-NIR spectrophotometer. Absorption spectra of the films were measured with Agilent 8453 UV/vis spectrophotometer.

4.4.4.4. Steady-state measurements

For the steady-state PL 1"x1" quartz substrates were used to avoid any additional signals and the necessary material was thermally evaporated in an evaporation chamber at a base pressure of 10^{-6} mBar. The emission spectra were measured at room temperature on a HORIBA Jobin Yvon Fluorolog 3-222 spectrofluorometer, using a 450 W xenon arc lamp and a R928P PMT detector and a front-faced orientation. We note that the PL peak emission wavelengths in films were slightly longer than the devices' EL peak, possibly due to the weak microcavity effect.

4.4.4.5. Transient PL measurements

Time-resolved emission spectra (TRES) were measured with a home-built nanosecond setup. A Continuum Surelite II laser (5 ns, 20 Hz) was used for excitation at 355 or 266 nm. A collection window in the spectrograph was set to avoid the excitation photons, and a long-pass filter was used to eliminate any leakage of the excitation light. The spectra at different times from the laser pulse were collected with a synchronized ICCD camera (Andor Technology Ltd., Belfast, UK) coupled with a spectrograph. Emission measurements from the films were performed in front-faced orientation. PL decay curves were constructed from the TRES near the peak maximum unless mentioned otherwise. Initial fast decay (< 5 ns) was avoided by time-gating in the samples showing long-lived emission. The decay curves were fitted with bi- or tri-exponential functions. Only PL decay times longer than 5 ns are meaningful since the <5

ns component is below our instrumental time resolution. Hence, the faster component of the fluorescence of some of the films could not be measured.

4.5. Acknowledgment

Ames Laboratory is operated by Iowa State University for the US Department of Energy (USDOE) under Contract No. DE-AC 02-07CH11358. The initial stages of the research were partially supported by NSF Grant ECCS 1202309. The advanced and final stages were partially supported by Basic Energy Sciences, Division of Materials Science and Engineering, USDOE.

4.6. References

(1) Liu, R.; Cai, Y.; Park, J. M.; Ho, K. M.; Shinar, J.; Shinar, R. Organic Light-Emitting Diode Sensing Platform: Challenges and Solutions. *Adv. Funct. Mater.* **2011**, *21* (24), 4744–4753.

(2) Manna, E.; Xiao, T.; Shinar, J.; Shinar, R. *Organic Photodetectors in Analytical Applications*; 2015; Vol. 4.

(3) Tsutsui, T.; Yang, M.-J.; Yahiro, M.; Nakamura, K.; Watanabe, T.; Tsuji, T.; Fukuda, Y.; Wakimoto, T.; Miyaguchi, S. High Quantum Efficiency in Organic Light-Emitting Devices with Iridium-Complex as a Triplet Emissive Center. *Jpn. J. Appl. Phys.* **1999**, *38* (Part 2, No. 12B), L1502.

(4) Adachi, C.; Baldo, M. A.; Forrest, S. R.; Thompson, M. E. High-Efficiency Organic Electrophosphorescent Devices with Tris(2- Phenylpyridine)Iridium Doped into Electrontransporting Materials. *Appl. Phys. Lett* **2000**, *77*, 904.

(5) Adachi, C.; Baldo, M. A.; Thompson, M. E.; Forrest, S. R. Nearly 100% Internal Phosphorescence Efficiency in an Organic Light-Emitting Device. *J. Appl. Phys.* **2001**, *90*, 5048.

(6) D'andrade, B. W.; Baldo, M. A.; Adachi, C.; Brooks, J.; Thompson, M. E.; Forrest, S. R. High-Efficiency Yellow Double-Doped Organic Light-Emitting Devices Based on Phosphorsensitized Fluorescence. *Appl. Phys. Lett* **2001**, *79*, 1045.

(7) Shinar, J.; Savvateev, V. Organic Light Emitting Devices - A Survey. In *Organic light emitting devices - A survey*; Shinar, J., Ed.; Springer, New York, 2004; pp 1–41.

(8) Zhang, Y.; Lee, J.; Forrest, S. R. Tenfold Increase in the Lifetime of Blue Phosphorescent Organic Light-Emitting Diodes. *Nat. Commun.* **2014**, *5*, 5008.

(9) Kim, Y. H.; Jeong, H. C.; Kim, S. H.; Yang, K.; Kwon, S. K. High-Purity-Blue and High-Efficiency Electroluminescent Devices Based on Anthracene. *Adv. Funct. Mater.* **2005**, *15* (11), 1799–1805.

(10) Zhu, Z.-L.; Chen, M.; Chen, W.-C.; Ni, S.-F.; Peng, Y.-Y.; Zhang, C.; Tong, Q.-X.; Lu, F.; Lee, C.-S. Removing Shortcomings of Linear Molecules to Develop High Efficiencies Deep-Blue Organic Electroluminescent Materials. *Org. Electron.* **2016**, *38*, 323.

(11) Zhu, M.; Yang, C. Blue Fluorescent Emitters: Design Tactics and Applications in Organic Light-Emitting Diodes. *Chem. Soc. Rev.* **2013**, *42* (12), 4963–4976.

(12) Shih, P. I.; Chuang, C. Y.; Chien, C. H.; Diau, E. W. G.; Shu, C. F. Highly Efficient Non-Doped Blue-Light-Emitting Diodes Based on an Anthrancene Derivative End-Capped with Tetraphenylethylene Groups. *Adv. Funct. Mater.* **2007**, *17* (16), 3141–3146.

(13) Uoyama, H.; Goushi, K.; Shizu, K.; Nomura, H.; Adachi, C. Highly Efficient Organic Light-Emitting Diodes from Delayed Fluorescence. *Nature* **2012**, *492*, 234.

(14) Goushi, K.; Yoshida, K.; Sato, K.; Adachi, C. Organic Light-Emitting Diodes Employing Efficient Reverse Intersystem Crossing for Triplet-to-Singlet State Conversion. *Nat. Photonics* **2012**, *6* (4), 253–258.

(15) Miwa, T.; Kubo, S.; Shizu, K.; Komino, T.; Adachi, C.; Kaji, H. Blue Organic Light-Emitting Diodes Realizing External Quantum Efficiency over 25% Using Thermally Activated Delayed Fluorescence Emitters. *Sci. Rep.* **2017**, *7*, 287.

(16) Dos Santos, P. L.; Dias, F. B.; Monkman, A. P. Investigation of the Mechanisms Giving Rise to TADF in Exciplex States. *J. Phys. Chem. C* **2016**, *120*, 32.

(17) Dias, F. B.; Penfold, T. J.; Monkmon, A. P. Photophysics of Thermally Activated Delayed Fluorescence Molecules. *Methods Appl. Fluoresc.* **2017**, *5*, 012001.

(18) Sarma, M.; Wong, K.-T. Exciplex: An Intermolecular Charge-Transfer Approach for TADF. *Appl. Mater. Interfaces* **2018**, *10*, 19279.

(19) Han, S. H.; Jeong, J. H.; Yoo, J. W.; Lee, J. Y. Ideal Blue Thermally Activated Delayed Fluorescence Emission Assisted by a Thermally Activated Delayed Fluorescence Assistant Dopant through a Fast Reverse Intersystem Crossing Mediated Cascade Energy Transfer Process. *J. Mater. Chem. C* **2019**, *7*, 3082.

(20) Fan, X.; Li, C.; Wang, Z.; Wei, Y.; Duan, C.; Han, C.; Xu, H. Enhancing Reverse Intersystem Crossing via Secondary Acceptors: Toward Sky-Blue Fluorescent Diodes with 10-Fold Improved External Quantum Efficiency. *ACS Appl. Mater. Interfaces* **2019**, *11*, 4185–4192.

(21) Zhang, Q.; Li, J.; Shizu, K.; Huang, S.; Hirata, S.; Miyazaki, H.; Adachi, C. Design of Efficient Thermally Activated Delayed Fluorescence Materials for Pure Blue Organic Light Emitting Diodes. *J. Am. Chem. Soc* **2012**, *134*, 8.

(22) Lee, J.; Shizu, K.; Tanaka, H.; Nomura, H.; Yasuda, T.; Adachi, C. Oxadiazole-and Triazole-Based Highly-Efficient Thermally Activated Delayed Fluorescence Emitters for Organic Light-Emitting Diodes. *J. Mater. Chem. C* **2013**, *1*, 4599.

(23) Nakanotani, H.; Masui, K.; Nishide, J.; Shibata, T.; Adachi, C. Promising Operational Stability of High-Efficiency Organic Light-Emitting Diodes Based on Thermally Activated Delayed Fluorescence. *Sci. Rep.* **2013**, *3*, 2127.

(24) Liu, X.-K.; Zhang, W.-J.; Qing, J.; Chen, Z.; Wu, B.; Tam, H. L.; Zhang, X.-H.; Zhu, F.; Lee, C.-S. Remanagement of Singlet and Triplet Excitons in Single-Emissive-Layer Hybrid White Organic Light-Emitting Devices Using Thermally Activated Delayed Fluorescent Blue Exciplex. *Adv. Mater.* **2015**, *27* (44), 7079–7085.

(25) Gaj, M. P.; Fuentes-Hernandez, C.; Zhang, Y.; Marder, S. R.; Kippelen, B. Highly Efficient Organic Light-Emitting Diodes from Thermally Activated Delayed Fluorescence Using a Sulfone-Carbazole Host Material. *Org. Electron.* **2015**, *16*, 109.

(26) Seino, Y.; Inomata, S.; Sasabe, H.; Pu, Y. J.; Kido, J. High-Performance Green OLEDs Using Thermally Activated Delayed Fluorescence with a Power Efficiency of over 100 Lm W-1. *Adv. Mater.* **2016**, *28* (13), 2638–2643.

(27) Lin, T.-A.; Chatterjee, T.; Tsai, W.-L.; Lee, W.-K.; Wu, M.-J.; Jiao, M.; Pan, K.-C.; Yi, C.-L.; Chung, C.-L.; Wong, K.-T.; et al. Sky-Blue Organic Light Emitting Diode with 37% External Quantum Efficiency Using Thermally Activated Delayed Fluorescence from Spiroacridine-Triazine Hybrid. *Adv. Mater.* **2016**, *28* (32), 6976–6983.

(28) Nakanotani, H.; Higuchi, T.; Furukawa, T.; Masui, K.; Morimoto, K.; Numata, M.; Tanaka, H.; Sagara, Y.; Yasuda, T.; Adachi, C. High-Efficiency Organic Light-Emitting Diodes with Fluorescent Emitters. *Nat. Commun.* **2014**, *5*, 4016.

(29) Sun, J. W.; Baek, J. Y.; Kim, K.-H.; Moon, C.-K.; Lee, J.-H.; Kwon, S.-K.; Kim, Y.-H.; Kim, J.-J. Thermally Activated Delayed Fluorescence from Azasiline Based Intramolecular Charge-Transfer Emitter (DTPDDA) and a Highly Efficient Blue Light Emitting Diode. *Chem. Mater.* **2015**, *27* (19), 6675–6681.

(30) Lee, I. H.; Song, W.; Lee, J. Y.; Hwang, S.-H. High Efficiency Blue Fluorescent Organic Light-Emitting Diodes Using a Conventional Blue Fluorescent Emitter. *J. Mater. Chem. C* **2015**, *3* (34), 8834–8838.

(31) Cui, L. S.; Nomura, H.; Geng, Y.; Kim, J. U. k.; Nakanotani, H.; Adachi, C. Controlling Singlet–Triplet Energy Splitting for Deep-Blue Thermally Activated Delayed Fluorescence Emitters. *Angew. Chemie - Int. Ed.* **2017**, *56* (6), 1571–1575.

(32) Zhang, T.; Zhao, B.; Chu, B.; Li, W.; Su, Z.; Wang, L.; Wang, J.; Jin, F.; Yan, X.; Gao, Y.; et al. Blue Exciplex Emission and Its Role as a Host of Phosphorescent Emitter. *Org. Electron.* **2015**, *24*, 1–6.

(33) Wong, M. Y.; Zysman-Colman, E.; Wong, M. Y.; Zysman-Colman, E. Purely Organic Thermally Activated Delayed Fluorescence Materials for Organic Light-Emitting Diodes. *Adv. Mater.* **2017**, *29*, 1605444.

(34) Lee, J.; Chen, H.-F.; Batagoda, T.; Coburn, C.; Djurovich, P. I.; Thompson, M. E.; Forrest, S. R. Deep Blue Phosphorescent Organic Light-Emitting Diodes with Very High Brightness and Efficiency. *Nat. Mater.* **2015**, *15* (1), 92–98.

(35) Jankus, V.; Chiang, C. J.; Dias, F.; Monkman, A. P. Deep Blue Exciplex Organic Light-Emitting Diodes with Enhanced Efficiency; P-Type or E-Type Triplet Conversion to Singlet Excitons? *Adv. Mater.* **2013**, *25* (10), 1455–1459.

(36) Reineke, S.; Lindner, F.; Schwartz, G.; Seidler, N.; Walzer, K.; Lüssem, B.; Leo, K. White Organic Light-Emitting Diodes with Fluorescent Tube Efficiency. *Nature* **2009**, *459*, 234.

(37) Liu, R.; Xu, C.; Biswas, R.; Shinar, J.; Shinar, R. MoO3 as Combined Hole Injection Layer and Tapered Spacer in Combinatorial Multicolor Microcavity Organic Light Emitting Diodes. *Appl. Phys. Lett.* **2011**, *99*, 093305.

(38) Lee, J. Y. Mixed-Host-Emitting Layer for High-Efficiency Organic Light-Emitting Diodes. *J. Inf. Disp.* **2014**, *15* (3), 139–144.

(39) Bhattacharya, S.; Nayak, S. K.; Chattopadhyay, S.; Banerjee, M.; Mukherjee, A. K. Study of Charge-Transfer Complexes of [60]-and [70]Fullerenes with a Series of Phosphine Oxides. *J. Phys. Chem. B* **2003**, *107*, 13022–13028.

(40) Burrows, P. E.; Padmaperuma, A. B.; Sapochak, L. S.; Djurovich, P.; Thompson, M. E. Ultraviolet Electroluminescence and Blue-Green Phosphorescence Using an Organic Diphosphine Oxide Charge Transporting Layer. *Appl. Phys. Lett* **2006**, *88*, 183503.

(41) Padmaperuma, A. B.; Sapochak, L. S.; Burrows, P. E. New Charge Transporting Host Material for Short Wavelength Organic Electrophosphorescence: 2,7-Bis(Diphenylphosphine Oxide)-9,9-Dimethylfluorene. *Chem. Mater.* **2006**, *18*, 2389.

(42) Xu, H.; Yin, K.; Huang, W. Highly Improved Electroluminescence from a Series of Novel Eu111 Complexes with Functional Single-Coordinate Phosphine Oxide Ligands: Tuning the Intramolecular Energy Transfer, Morphology, and Carrier Injection Ability of the Complexes. *Chem. - A Eur. J.* **2007**, *13* (36), 10281–10293.

(43) Ha, M. Y.; Moon, D. G. Organic Light-Emitting Devices with Triphenylphosphine Oxide Layer. *Synth. Met.* **2008**, *158*, 617–619.

(44) Ha, M.-Y.; Moon, D.-G. Low Voltage Organic Light-Emitting Devices with Triphenylphosphine Oxide Layer. *Appl. Phys. Lett* **2008**, *93*, 43306.

(45) Jeon, S. O.; S, yook K.; Joo, C. W.; Lee, J. Y. A Phosphine Oxide Derivative as a Universal Electron Transport Material for Organic Light-Emitting Diodes. *J. Mater. Chem.* **2009**, *19*, 5940.

(46) Kim, T.-Y.; Moon, D.-G. Low Voltage Red Phosphorescent Organic Light-Emitting Devices with Triphenylphosphine Oxide and 4,4 0-Bis(2,2 0-Diphenylvinyl)-1,1 0-Biphenyl Electron Transport Layers. *Curr. Appl. Phys.* **2010**, *10*, 1108.

(47) Jeon, S. O.; Lee, J. Y. Phosphine Oxide Derivatives for Organic Light Emitting Diodes. *J. Mater. Chem.* **2012**, *22*, 4233.

(48) Sun, H.; Shen, W.; Zhang, X.; Zhang, D.; Li, M. Theoretical Investigations of the Electronic Structures of Carbazole-Based Triphenylphosphine Oxide Derivatives, Potential Bipolar Host Materials in Blue-Phosphorescent Devices. *J. Mol. Model.* **2015**, *21*, 320.

(49) Wang, R.-B.; Wang, Q.-K.; Xie, H.-J.; Xu, L.-H.; Duhm, S.; Li, Y.-Q.; Tang, J.-X. HATCN-Based Charge Recombination Layers as Effective Interconnectors for Tandem Organic Solar Cells. *Appl. Mater. Interfaces* **2014**, *6*, 15604.

(50) Perez-Bolivar, C. A. Synthesis and Studies of Materials for Organic Light-Emitting Diodes, Bowling Green State University, 2010.

(51) Joly, D.; Bouit, P.-A.; Hissler, M. Organophosphorus Derivatives for Electronic Devices. *J. Mater. Chem. C* **2016**, *4*, 3686.

(52) Jia, J.; Zhu, L.; Wei, Y.; Wu, Z.; Xu, H.; Ding, D.; Chen, R.; Ma, D.; Huang, W. Triazine-Phosphine Oxide Electron Transporter for Ultralow-Voltage-Driven Sky Blue PHOLEDs. *J. Mater. Chem. C* **2015**, *3*, 4890.

(53) Pawlik, T. D.; Kondakov, D. Y.; Begley, W. J.; Young, R. H. Charge Carriers and Charge-Transfer Reactions in OLED Devices Studied by Electron Paramagnetic Resonance. *J. Soc. Inf. Disp.* **2009**, *40*, 413.

(54) Pawlik, T. D.; Kondakova, M. E.; Giesen, D. J.; Deaton, J. C.; Kondakov, D. Y. Charge Carriers and Triplets in OLED Devices Studied by Electrically Detected Electron Paramagnetic Resonance. *J. Soc. Inf. Disp.* **2009**, *17*, 279.

(55) Lee, S.; Lee, J.-H.; Kim, H.; Yoo, S.-J.; Kim, T. G.; Kim, J. W.; Kim, J.-J. Determination of the Interface Energy Level Alignment of a Doped Organic Hetero-Junction Using Capacitance-Voltage Measurements. *Org. Electron.* **2012**, *13*, 2346.

(56) Etter, M. C.; Baures, P. W. Triphenylphosphine Oxide as a Crystallization Aid. *J. Am. Chem. Soc.* **1988**, *110* (2), 639–640.

(57) Cekaviciute, M.; Simokaitiene, J.; Volyniuk, D.; Sini, G.; Grazulevicius, J. V. Arylfluorenyl-substituted metoxytriphenylamines as deep blue exciplex forming bipolar semiconductors for white and blue organic light emitting diodes. Dye. Pigment. **2017**, 140, 187.

CHAPTER 5. GENERAL DISCUSSION

Organic electronics is a promising field given the of potential applications in, e.g., displays, with OLEDs already utilized in commercial products, lighting, (bio)chemical sensing and medical. Extensive R&D is still ongoing to improve the various devices, including reducing their cost.

In OLEDs, enhancing light outcoupling in a cost-effective approach remains one of the main R&D focus areas, and this dissertation discusses a novel approach to enhance light outcoupling that is transferrable to low-cost R2R processing. Another key aspect of OLEDs is their use in solid state lighting, where a more efficient and stable blue emission is needed. This dissertation studied the possibility of using exciplex-based OLEDs to achieve bright deep blue OLEDs.

PhOLEDs can achieve 100% IQE due to strong spin-orbit coupling in organic molecules with a heavy atom. Yet the EQE is typically limited to ~20% due to forward outcoupling failure. The use of corrugated plastic substrates resulted in improved light extraction via diffraction and possibly scattering effects. A green PhOLED with 50% EQE (which entails outcoupling efficiency ≥50%) was demonstrated using optimized corrugation heights of 280-400 nm and a pitch of ~ 750 nm. The high EQE is a result of minimizing the internal and possibly external waveguiding modes as well as disrupting surface plasmon formation at the metal cathode. Outcoupling enhancements, though to a lesser extent, were demonstrated for blue and white PhOLEDs. Simulations are in agreement with experimental results. Further experimental and theoretical studies are ongoing to evaluate different types, including aperiodic.

In current studies, we used mostly a thin PEDOT:PSS layer as the anode as it was hard to achieve high-quality PC/ITO due to ITO deposition on plastic at lower temperatures in comparison to glass/ITO deposition. To further enhance the outcoupling and device efficiency, the anode conductivity has to be increased. This can be achieved by embedding a honeycomb metal mesh in the substrate and covering it by ITO. The OLEDs on the corrugated substrates demonstrate an emission profile that is close to a Lambertian.

As mentioned above, low efficient unstable blue OLEDs, especially deep blue emitters, are problematic due to low efficiencies and stability. This dissertation investigated a different approach to achieve bright deep blue emission by using triplet exciplex emission. An extremely deep blue OLED with peak emission at ~435 nm was achieved with a brightness of ~14000 cd/m^2 and an EQE of 4%.